Summer 2016

Uncertainty assessment for free-running model cases at the IIHR wave basin

Michael John Bottiglieri
University of Iowa

UNCERTAINTY ASSESSMENT FOR FREE-RUNNING MODEL CASES AT THE IIHR WAVE BASIN

by

Michael John Bottiglieri

A thesis submitted in partial fulfillment
of the requirements for the Master of Science
degree in Mechanical Engineering in the
Graduate College of
The University of Iowa

August 2016

Thesis Supervisors: Professor Frederick Stern
Associate Research Scientist Yugo Sanada

Graduate College
The University of Iowa
Iowa City, Iowa

CERTIFICATE OF APPROVAL

_____

MASTER'S THESIS

_____

This is to certify that the Master's thesis of

Michael John Bottiglieri

has been approved by the Examining Committee for
the thesis requirement for the Master of Science degree
in Mechanical Engineering at the August 2016 graduation.

Thesis Committee: _____
Frederick Stern, Thesis Supervisor

_____
Yugo Sanada, Thesis Supervisor

_____
James Buchholz

ACKNOWLEDGEMENTS

Without the guidance of Professor Frederick Stern and Yugo Sanada it would not have been possible to have gained the full potential of my learning experience. I want to sincerely thank them for the continuous support and encouragement both during the past year spent completing my thesis and the later stages of my undergraduate career when I gained my interest in fluid mechanics. Having two advisors with such a high wealth of knowledge has helped me gain a greater understanding than I initially expected when I took this path of education. I would also like to thank the IIHR and the Mechanical Engineering department for their assistance and answers to my questions throughout the graduate school process.

ABSTRACT

Uncertainty analysis is performed to analyze the motions and results of maneuvering characteristics of a 1/49 scale surface combatant model during free-running maneuverability testing. The model is designed with a twin rudder and twin propeller rotating inwards. Calm water and wave testing is completed with an initial ship speed corresponding to a Froude Number of 0.20 while the wave cases have wavelength to ship length ratio of 1.0 and wave height to wavelength ratio of 0.02. These conditions were tested for course keeping, turning circle, and zig zag maneuvers. The turning circles were completed to both port and starboard side. Tracking of the model is completed with an overhead carriage design with a mounted camera to record the motions of the ship and convert these motion to six degree of freedom motions. The combination of the tracking systems are analyzed to find the systematic standard uncertainty of the system.

Uncertainty was performed in accordance with the performance test codes written by ASME during 2013 to find the systematic standard and random uncertainty of measurements. The random uncertainty is found based on the standard deviation of repeated measurements, while the systematic standard uncertainty is found based on the bias of the measurement system and the sensitivity coefficients found from the data reduction equations. The data reduction equations are used to non-dimensionalize the measured values to compare to CFD results as well as results from other model scales. From the data reduction equations partial derivatives are taken to determine how the uncertainty propagates throughout the sensitivity coefficients. After the uncertainties are calculated the results were compared to other facilities to evaluate the method used and

gauge the quality of the repeatability of the measurements. Few other facilities have analyzed the uncertainty during free running tests past looking at the random error based on repeated tests. The comparison with these facilities displayed that the uncertainty process and measurement repeatability used by IIHR at the wave basin produce consistent results with limited uncertainties when the end results of maneuvering characteristics are observed. Large uncertainties occur for some of the measured variables during the full scale of the testing time when the uncertainties are reported as a percentage of the harmonic amplitudes and the reported harmonic amplitude are near zero with a small uncertainty.

PUBLIC ABSTRACT

The Office of Naval Research Tumblehome (ONRT) is a commonly used research vessel representing what was previously a potential surface combatant design. The model is tested at the IIHR wave basin, a 20x40 m basin with six plunger type wave makers on the west end. An overhead carriage is mounted to traverse the length and width of the basin to track and follow the ship during free-running maneuvering tests.

The model was run through course keeping, turning circle, and zig zag maneuvers to determine the stability and maneuverability of the ship design to serve as benchmark data for computational fluid dynamics (CFD) simulations. Testing was performed in both calm water and wave conditions matching the conditions tested by CFD. The values measured are analyzed to determine the uncertainty within the tracking and measurement systems to determine the overall uncertainty from repeated tests. The uncertainty is found as a combination of systematic and random uncertainties representing the propagation of errors within the tracking system and the deviation between repeat trials. The propagation is found based on the sensitivity coefficients found by taking the partial derivatives of data reduction equations used to manipulate the reported values. The combination of the random and systematic standard uncertainties are reported in relation to the mean measured values found through harmonic analysis of the results. The results are analyzed and compared to both CFD simulations and other facility results to evaluate the effectiveness of the reported uncertainties.

TABLE OF CONTENTS

LIST OF TABLES

LIST OF FIGURES

NOMENCLATURE

6DOF	6-Degree of Freedom
A	Desired Wave Amplitude
ASME	American Society of Mechanical Engineers
b_r	Systematic Standard Uncertainty
CFD	Computational Fluid Dynamics
f_p	Plunger Frequency
Fr	Froude Number
g	Gravitational Constant
H	Wave Height
IIHR	Iowa Institute of Hydroscience Research
IMO	International Maritime Organization
ISO	International Organization for Standardization
ITTC	International Towing Tank Conference
k	Wave Number
L	Ship Length
n	Propeller Speed
ONR	Office of Naval Research
PTC	Performance Test Code
$\bar{r}$	Mean Value
s_r	Standard Deviation
$s_{\bar{r}}$	Random Uncertainty
u	Surge Velocity
U	Ship Speed
u_r	Combined Uncertainty
$U_{95,r}$	Expanded Uncertainty
v	Sway Velocity
VMCS	Visual Motion Capture System
z	Heave
δ	Rudder Angle
ζ	Wave Elevation
θ	Pitch
$\theta_{x_i/r}$	Partial Derivative
λ	Wavelength
ϕ	Roll
σ	Sinkage
τ	Trim
ψ	Yaw

CHAPTER 1: INTRODUCTION

In order to validate the ever advancing simulations from computational fluid dynamics (CFD) accurate experimental data must be acquired. With the current CFD capabilities ships can be modeled in both towed and free-running trials. Outputted results fully describe the motion and forces acting on the ship in both calm water and wave situations with various headings. With the advancement in the capabilities of CFD the requirements from the experimental (EFD) results also increases. CFD currently has the ability to produce consistent results showing seakeeping (Castiglione, 2011), maneuvering (Bhushan, 2009), and capsizing situations (Carrica, 2008). In order to validate these simulations facilities capable of producing these results experimentally are required, this situation calls for a facility capable of accurately tracking the ship model through various forms of free-running and towed motions. The IIHR wave basin was designed and built to test model scale ships and provide benchmark data to validate the IIHR CFDShip Iowa. The facility is equipped with six plunger type wave makers, a carriage to maneuver in the x-direction, and a sub-carriage designed to rotate on the xy plane and move in the y-direction. Additionally a model tracking system, model release system, and semi-captive mount are used to test the performance of various ship models in a range of wave conditions.

Throughout history model ships have been designed, built, and tested, to determine ship worthiness before a full scale ship was built. One of the earliest recorded tests of such models was in the 1750's when two 1/48 scale model warships were towed through a calm lake a distance of 300 feet to observe the stability of the model before building a full scale

ship. This first test was less empirical than future tests due to the limited technology at this time. During the 1800's William Froude developed a method to compare model to full scale testing and designed an enclosed towing tank to test his theories on stability as well. These tests became more advanced with increased technology and by the late 1800's additional towing tanks were built around the world (Harley, 1994). The capabilities of towing tanks constantly increased with the eventual desire to test ships maneuverability in both calm water and waves. An early test of the turning capabilities of ships was described by Davidson in 1944, where he provided an early definition for advance, transfer, and tactical diameter and further discussed the relationship between the hull of a ship and its ability to maneuver. Ship design requirements expanded further to the stage they are today allowing for detailed analysis of ship motions in different environments with the capabilities to compare these results to those measured in CFD. Results have been verified by wind tunnels initially with the advancement to towing tank and free running wave tests in recent years.

The current wave basin facility has the capability to measure the maneuvering abilities of scaled ship models with accurate results, but for quality validation of CFD code the level of accuracy must be determined. By knowing the level of accuracy achieved from the EFD testing the confidence of the validation increases. If a slight deviation occurs between the EFD and CFD result but remains within the uncertainty of the measurement, the testing method can be confirmed as validated. Free running ship models have not yet been fully evaluated to determine the complete uncertainty of the tests. The repeatability of the runs is found by completing multiple runs with the same conditions to determine the scatter of the measurements, repeatability testing occurs for nearly all experimental

measurements (Miyazaki, 2011, Ueno, 2008, Eloot, 2015). The analysis of the systematic uncertainty of a free-running measurement has been briefly studied (Quadvlieg, 2011, Tonelli, 2015, and ITTC, 2014d), observing effects of deviations from initial conditions on the final result of testing. In order to determine the propagation of the uncertainties throughout the trial the procedures utilized simulations to determine how the resulting measurement would be affected based on an initial disturbance. This initial disturbance could be a deviation from the initial heading or a change in speed. By determining how the outcome is affected by an initial deviation the uncertainty can be estimated for a very limited set of test cases (ITTC, 2014d). These methods apply to the overall result of maneuvers including advance, transfer, tactical diameter, and overshoot angles, but do not accurately describe the uncertainty of the motions during the full testing time. By observing the uncertainty through the full testing time CFD results can be accurately validated describing position, orientation, and speeds across the duration of the test in various wave conditions. Uncertainty analysis was completed following the current guidelines in place by the American Society of Mechanical Engineers and ITTC procedures where applicable.

CHAPTER 2: EXPERIMENTAL METHODS

2.1 IIHR Wave Basin Facility

At the IIHR wave basin facility both free running and captive ship model tests are performed within the 40x20 square meter basin with a depth of 4.3 meters. The free running tests are performed by following the ship location with an overhead carriage and sub-carriage system while the towed tests are performed with a mount connecting the ship model to the sub-carriage. This carriage traverses on rails in the x-direction of the basin (east-west) and the sub-carriage moves on a rack-gear system in the y-direction (south-north). Additionally mounted to the sub-carriage is a rotating turntable that moves in the xy-plane. The limitations on the positioning of the carriage and sub-carriage are limited to an area of 29.7x15 square meters with a rotational limit of ± 720°. These limitations are due to the restrictions of the tracks that the carriage moves on, the limit of the rack-gear system, and the cable length restricting additional rotation. Located on the east end are six plunger type wave makers. On the west end is a 7.8x20 square meter beach with a tilt angle of 11.3° to limit the effect of waves reflecting. The north and south sides of the basin have rows of wave dampers that can be raised and lowered during testing. The dampers are lowered between tests to quicken the time period between wave tests and raised to not disturb the waves when testing occurs. Above the beach a dock and work station is located to allow for test setup and on the south-west corner of the basin a 4x1.9x1.5 m^3 trimming tank is located. The trimming tank is used to allow for easier lowering of the model into the water as well as used to perform ballasting on the model before initial testing begins. On the second floor of the wave basin two control panels are mounted to allow for

positioning of the carriage system and control of the wave makers. Figure 2.1 shows a schematic drawing of the basin as seen from above the north end while figure 2.2 shows the basin as seen from the wave makers (east end).

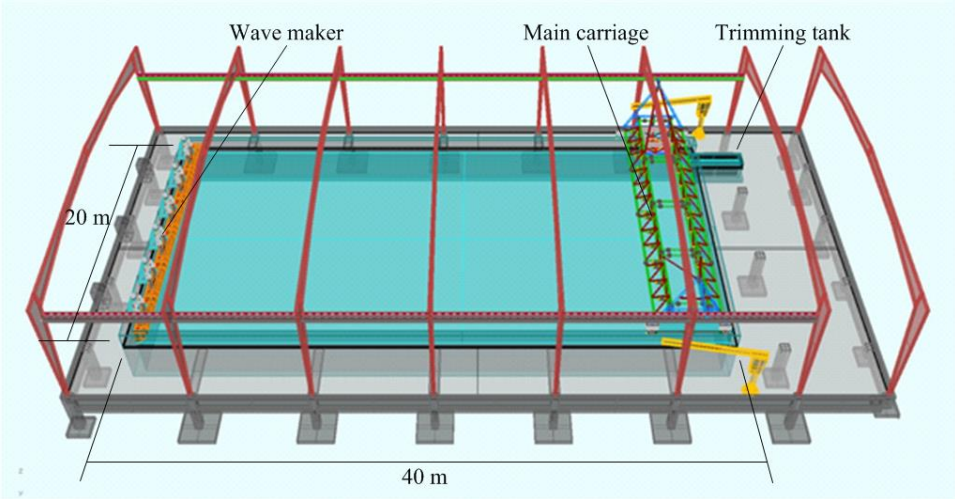

Figure 2.1: Schematic drawing of wave basin facility

Source: (Sanada et al., 2013)

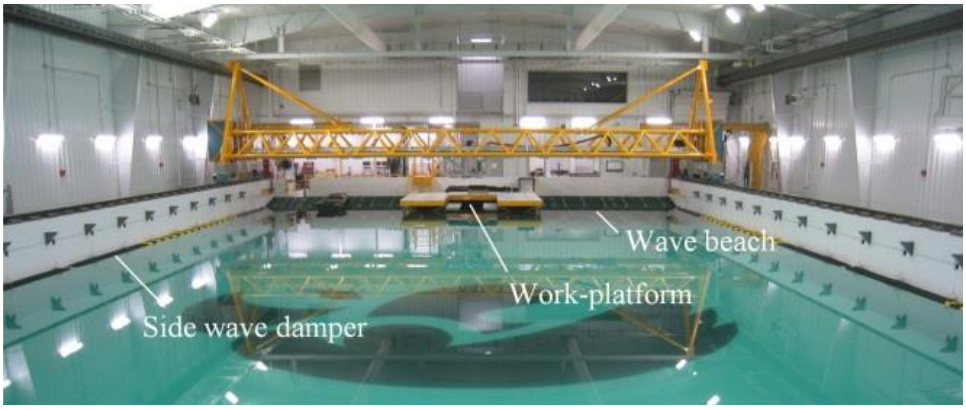

Figure 2.2: Wave basin view from wavemaker end

Source: (Sanada et al., 2013)

The wave makers are designed with six plungers with 1.2, 3.3, and 0.8 meters in height, width, and thickness respectively, with 100 mm of curvature, a profile image of the plunger can be seen in figure 2.3. At calm water conditions 0.7 meters of the thickness of the plunger is at the waterline and extends 0.7 meters below the surface. The motion of the plunger is driven vertically by a motor and screw-drive. The minimum plunger stroke is 77.5 mm and can operate at 2.0 Hz while the maximum plunger stroke is 250 mm but limited to 0.62 Hz the curve showing the relationship between plunger stroke and maximum frequency can be seen in figure 2.4. Through calibration a curve was fitted to find the relationship between plunger motion and the actual wave produced, this resulting calibration curve can be seen in figure 2.5. This curve is used to produce experimentally accurate waves throughout the full area of the wave basin. Both regular (all plungers moving in unison at a constant frequency, amplitude, and initial phase) and irregular waves (plungers move producing various predetermined frequencies and amplitudes) are possible to be produced by the wavemakers to simulate simple sinusoidal and more complex sea conditions, though at this time only regular waves have been calibrated.

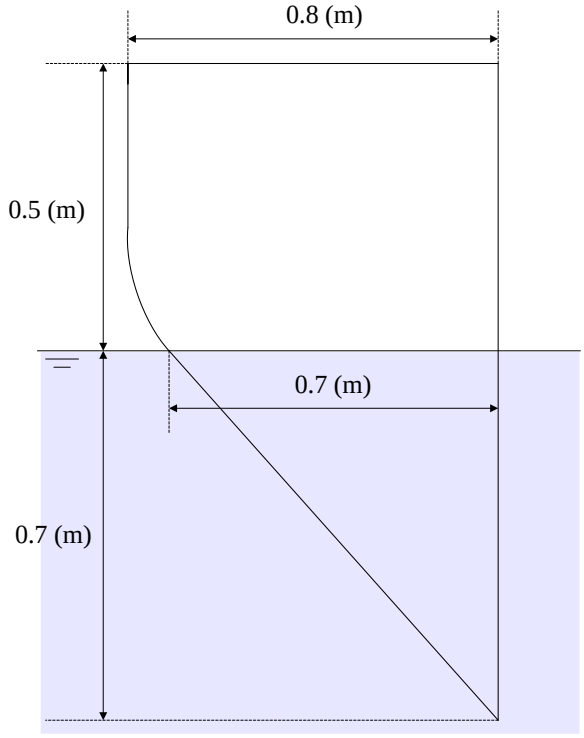

Figure 2.3: Cross section of plunger

Source: (Sanada et al., 2013)

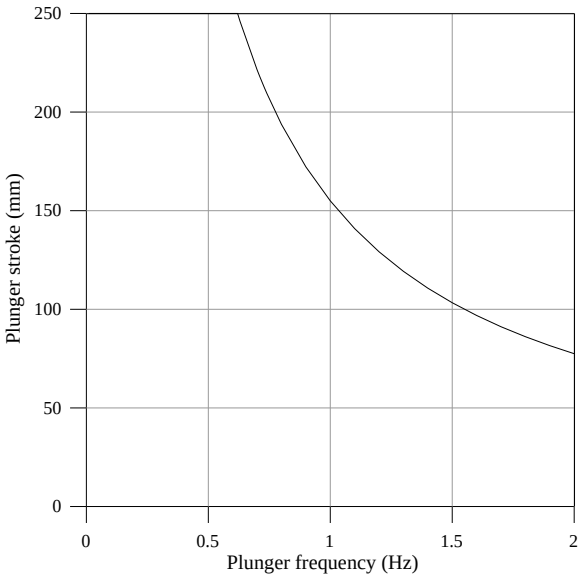

Figure 2.4: Maximal plunger stroke with respect to plunger frequency

Source: (Sanada et al., 2013)

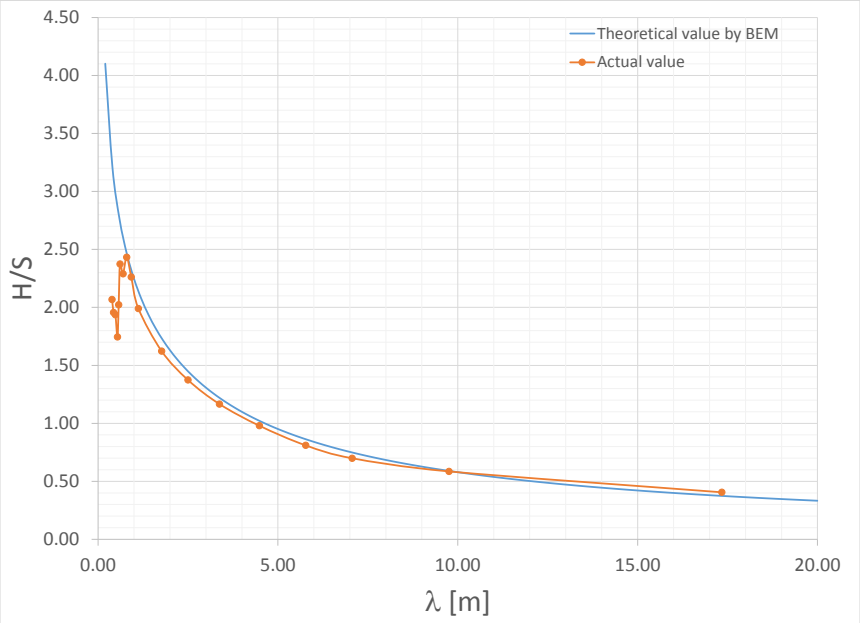

Figure 2.5: Ratio of wave height to plunger stroke with respect to wave length

Source: (Sanada et al., 2013)

2.2 Data Acquisition System

Within free-running tests the ship model is tracked by a combination of systems to ensure accuracy. The ship model is followed by the 12-ton main carriage, 2-ton sub-carriage, and the rotation of the turntable on the xy-plane. To increase the accuracy a 6 degree of freedom motion visual motion capture system (6DOF-VMCS) is implemented. This system functions by tracking a target board mounted on the ship, but must remain above the model to report the position. Also there is a free-running system used to control the ship as well as measure the roll angle, pitch angle, and yaw angle through a fiber optic gyroscope (FOG). The combination of these three systems allow for measuring the true motion of the model with redundancy for all motions except for heave, since the heave is only measured by the 6DOF-VMCS. During the initialization of a test the model is

mounted to the carriage by a semi-captive mount. The trial begins by activating two triggers to start the wavemaker and the free-running and 6DOF-VMCS systems. After initialization the wavemakers start and a time delay is included to allow for the waves to propagate through the basin. After this delay the model is accelerated to a set initial speed before the model is released. The two triggers have the potential to cause slight differences in the timing between systems, but this difference should be negligible.

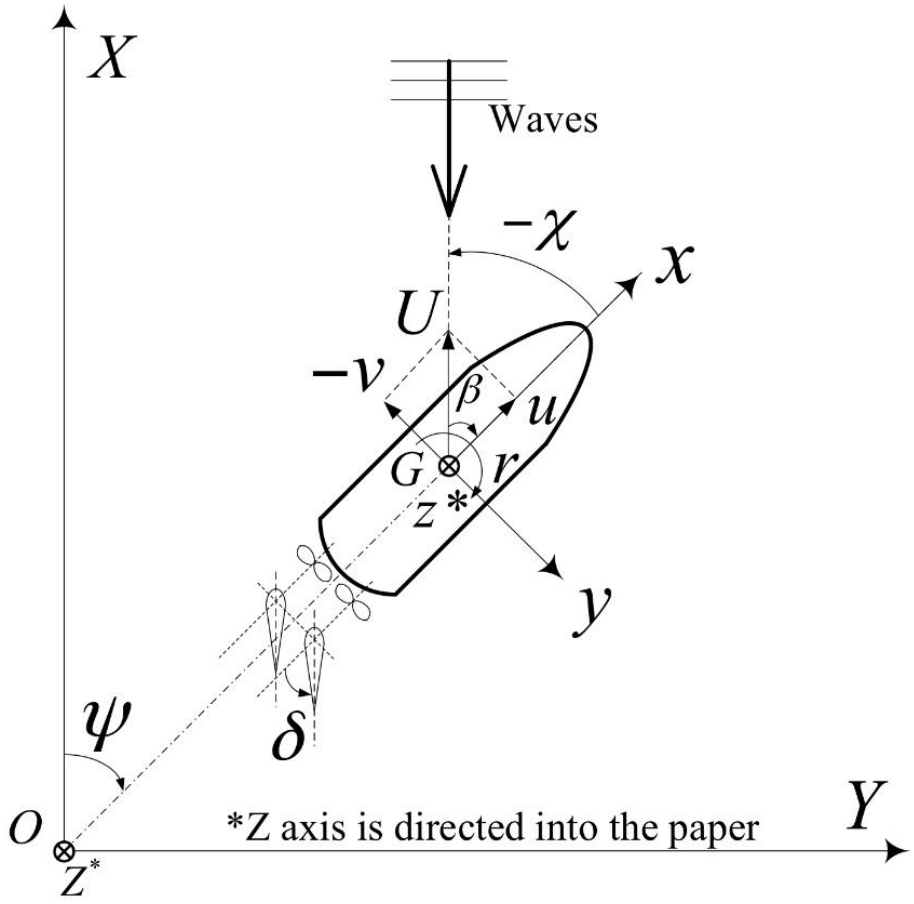

Figure 2.6: Ship coordinate system

Source: (Sanada et al., 2014)

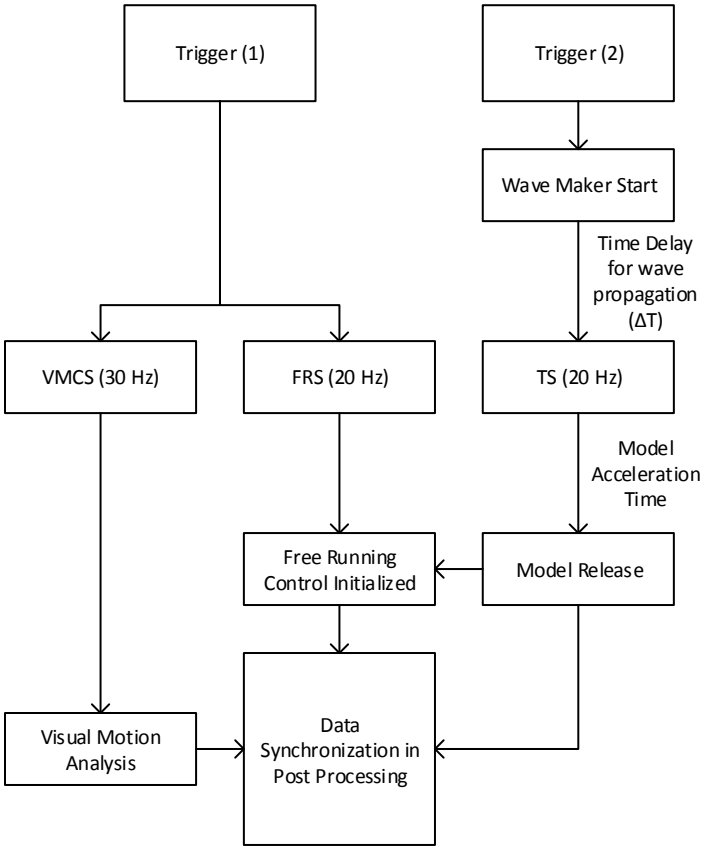

Figure 2.7: Trial initialization procedure

2.2.1 Carriage Tracking System

The carriage tracking system consists of the motion of the carriage, sub-carriage, and turntable to follow the x-position, y-position, and yaw of the ship. Mounted to the turntable are two infrared CCD cameras designed to see the brightness of two infrared LED lights compared to the darker background of the water. Mounted to the bow and stern of the ship are LED lights at a known equal distance from the longitudinal center of gravity. The carriage controller is designed in such a way that the carriage, sub-carriage, and turntable continually adjust to keep the centerpoint of the cameras as closely above the LED lights to ensure that the turntable center is close to the longitudinal center of gravity of the ship model. The initial position of the ship is the same as the initial position of the

turntable center due to the ship model being initially captive. The deviation from the initial camera views of the LED lights results in the calculated ship deviation from the sub-carriage position. The carriage tracking system operates at 20 Hz to report x and y position as well as the yaw angle of the ship model. The maximum carriage speed is 2.5 m/s in both the x and y-direction while the maximum rotational speed is 20 deg/s with accelerations of 0.75 m/s^2 and 10 deg/s^2 respectively. The image processing is fast enough to follow the ship in real-time and ensure that the LED lights attached to the ship as well as the target board remain visible by their respective cameras during the duration of the test. Mechanical limit switches are in place to ensure that the carriage does not overrun the limited test area of 29.7 by 15 square meters.

There are two key sources of error from the carriage tracking system. These can be reported as mechanical and errors from image processing. The mechanical errors are not easily measured but can be estimated to be small based on the chance that slipping occurred between the rails and the carriage itself. This error is only present in the x-direction. In the y-direction and the yaw there is a mechanical error of backlash within the gears but no possibility of slippage. This resulting error is estimated as very small. The error based on the image processing system is related to how accurately the camera system can identify the high contrast point that is the LED. The LED's location within the camera view is estimated based on a pixel count and the estimated distance from the centerpoint of the camera to the LED's location determines the deviation distance of the model. The numerical value of this uncertainty is based on how accurately the location can be estimated (resolution of the camera) as well as the distance from the camera to the LED. With the resting position of the ship model being 1.2 meters from the lens and a resolution of

480x640 pixels for the camera itself the resolution is 1.125 mm/pixel. Other smaller errors may occur within the measuring system such as rail alignment, and delay in the communication of data but these should be minor enough to be negligible. The outputted value from the image processing reports the deviation from the centerpoint of the turntable in x-position, y-position, and yaw, while the carriage position reports the position of the turntable centerpoint.

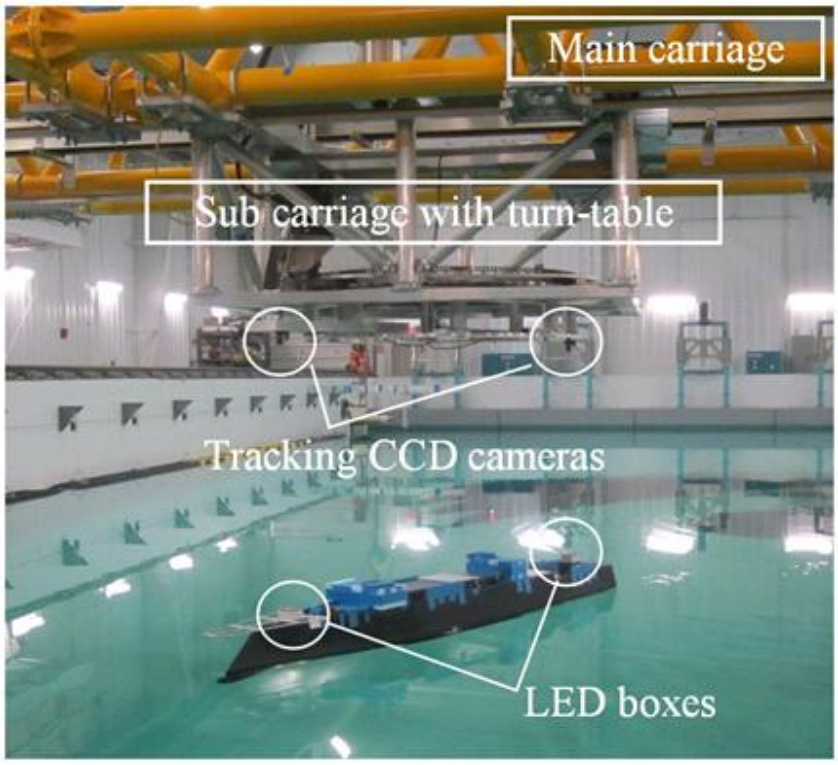

Figure 2.8: Carriage tracking system

Source: (Sanada et al., 2013)

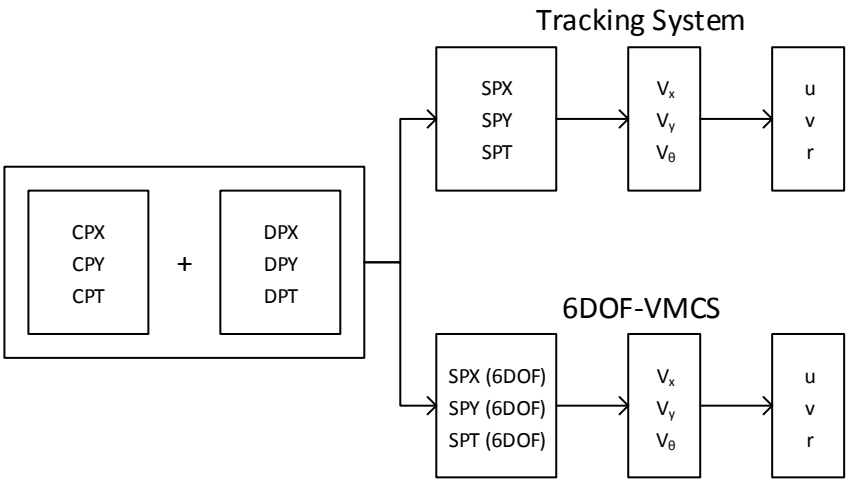

Figure 2.9: Determination of ship model position

2.2.2 6 Degree of Freedom Visual Motion Tracking System

As a way of increasing accuracy of the model position an additional system to track position was implemented. This system works by having a two dimensional target board mounted above the center of gravity of the ship with a high resolution camera mounted at the centerpoint of the sub-carriage and turntable. This target plate is comprised of black and white squares forming a rectangular board. The camera focuses on the target board to calculate the positions of each intersecting square. The corners of the squares represent high contrast points that can accurately be located within the field of view of the camera. These high contrast points are more accurately located by utilizing sub-pixel accuracy. Sub-pixel accuracy works by analyzing the gradient of color change from black to white in both the x and y-direction. The peak of this gradient change more accurately represents the corner of the respective squares than initial image processing allows. The drawback to utilizing sub-pixel accuracy is a longer processing time not allowing this method to be utilized in real-time. Once the corners are accurately found the processing software connects lines between the points to represent what would be perpendicular lines if the

target board was directly in front of the camera without distortion. Any motion in the x, y, or z-direction or rotation causes distortion of the found lines to occur. This distortion can be converted to displacement and rotation matrices by using a digital image pattern analysis method (Zhang, 2000), resulting in accurate measurements of the model position with 6 degrees of freedom. The reported values represent the deviation from the initial position of the target board to the target board's current position. If the process is approached algorithmically, there are four main steps. The first step is taking the first image with the camera and selecting the observed corners using sub-pixel detection. The first image is designated as image zero to represent the initial position of the target board. The second step involves looking close to the previously found points to find the movement of the board. The change in corner location represents the rigid motion to define the rotation and translation matrix. The third step is determining how far from image zero the current frame moved to define the displacement. The final step involves determining the motion of a generic point P (typically the longitudinal center of gravity) to define the overall motion of the body. Step 2-4 are repeated throughout the entire test (Benetazzo, 2011). The 6DOF-VMCS reports position to a higher accuracy than the carriage system as well as allowing for the heave of the ship model to be reported which was not possible with the previous free-running measurement system. This tracking system measures at 30 Hz which is the same frequency as the high resolution camera. Additional details describing the uncertainty of the 6DOF-VMCS can be seen in Appendix B.

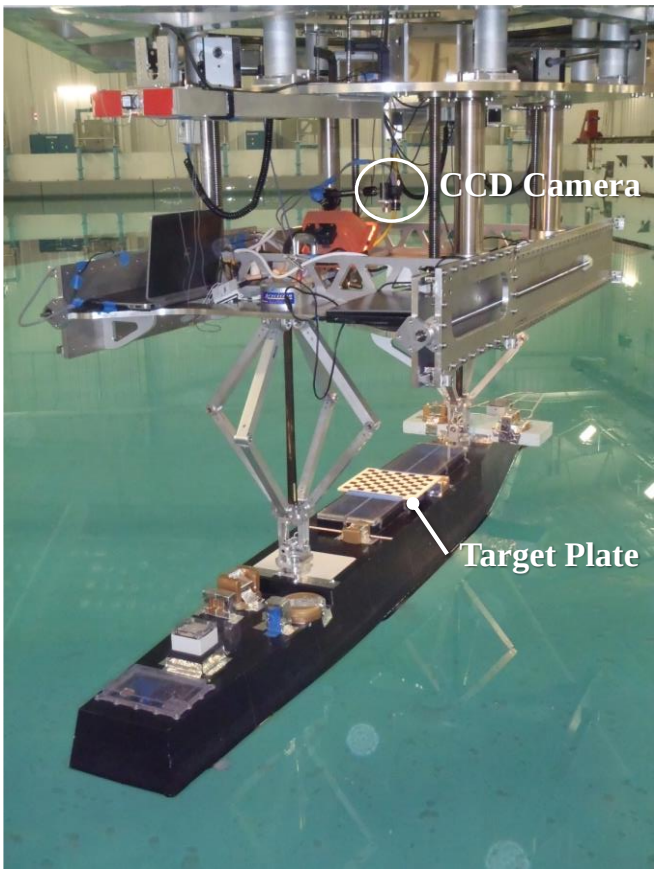

Figure 2.10: 6DOF visual motion tracking system

Source: (Sanada et al., 2013)

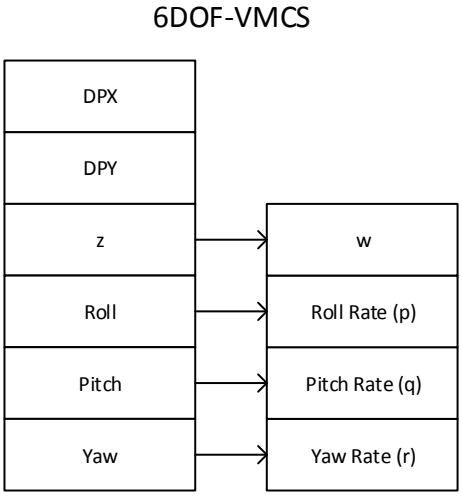

Figure 2.11: Measured and outputted variables from 6DOF-VMCS

2.2.3 Free-Running System

To allow for free-running tests a radio-control system must be implemented. The system consists of four blocks including control unit, drive unit, power unit, and a graphical user interface. The control unit consists of an on-board computer, a fiber optic gyroscopes (FOG), and the radio-control receiver. The drive unit consists of a motor speed controller, a reverse gear, gear motor, a two-axle allotter, and two shafts with propellers. To accurately measure the amount of propeller revolutions a plate with four slits at 90 degree intervals is attached to each shaft. This plate is placed in front of a photo-sensor to read the amount of times per minute that the slits pass the sensor to increase the count by one per pass. The total amount of passes is compared to the total time covered during the test as well as computer clock speed to determine the amount of revolutions per minute of each shaft. The rudder is controlled by two stepping motors rotating the rudder a fixed amount of degrees per pulse. This number of pulse signals is used to estimate the angle of the rudder at any given time throughout the test. The rudder angle is only an estimate due to the possibility that external forces can cause the motor pulse to not reach the expected angle change. The drive unit is powered by a 24-volt battery while the control unit is powered by a 12-volt battery. The combination of these batteries are the power unit that is placed in the ship model. The graphical user interface is used to input the test condition data onto the on-board computer from the on-land PC. These settings include test type, rotational speed of the propellers, rudder angle, offset rudder angle, speed/timing of rudder deflection, and auto-pilot PID gain. The combination of these settings allow the model to perform a wide range of tests including course keeping, turning circle, and zig-zag tests. The course keeping test starts the ship with an initial heading with the goal of maintaining that heading

throughout the test. The turning circle begins with the model moving in a straight line before engaging the rudder to a set angle for multiple full circle turns. The zig-zag test consists of the ship model beginning with a straight heading before engaging the rudder to a fixed angle until the heading of the ship reaches another predetermined heading. Once the heading is reached the rudder reverses to the same angle but negative until the heading angle is reached in the other direction. These three tests help to describe how a ship model behaves in both calm water and wave conditions. Throughout the test the FOG records data of the pitch, roll, and yaw at 20 Hz. The values for pitch and roll are measured with an accuracy of ± 0.5° while the yaw has an accuracy of ± 1.0°. The measured values from the FOG were compared to the outputted values from the 6DOF-VMCS to verify accuracy of the 6DOF-VMCS.

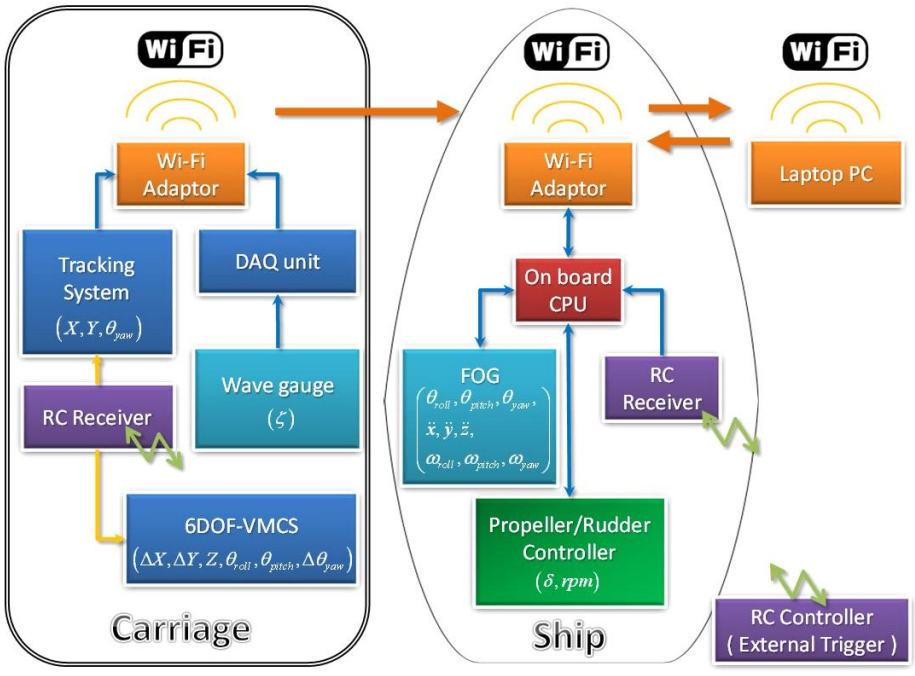

Figure 2.12: Diagram of the free running system

Source: (Sanada et al., 2013)

2.2.4 Model Release System

To begin free-running tests the ship model begins in a semi-captive state. The mount that is attached to the turntable on the sub-carriage is composed of two mechanical arms with electromagnets on the bottom end. The combination of hinges allow for free roll, pitch, and heave motions but restricts the surge, sway, and yaw. By using the semi-captive mount to initialize a test the carriage is used to accelerate the model to its intended speed. The carriage has a faster acceleration than the ship model would which allows the distance needed to perform a test to be reduced allowing for a longer time of data recording. After the intended speed is reached the electromagnets release and the mount retracts allowing the model to perform as a free-running ship. Additionally by releasing at a known initial speed and position the consistency between tests is improved allowing for increased repeatability. The mount can be seen in figure 2.13 with a demonstration of the motions that can be achieved while restrained by the semi-captive mount.

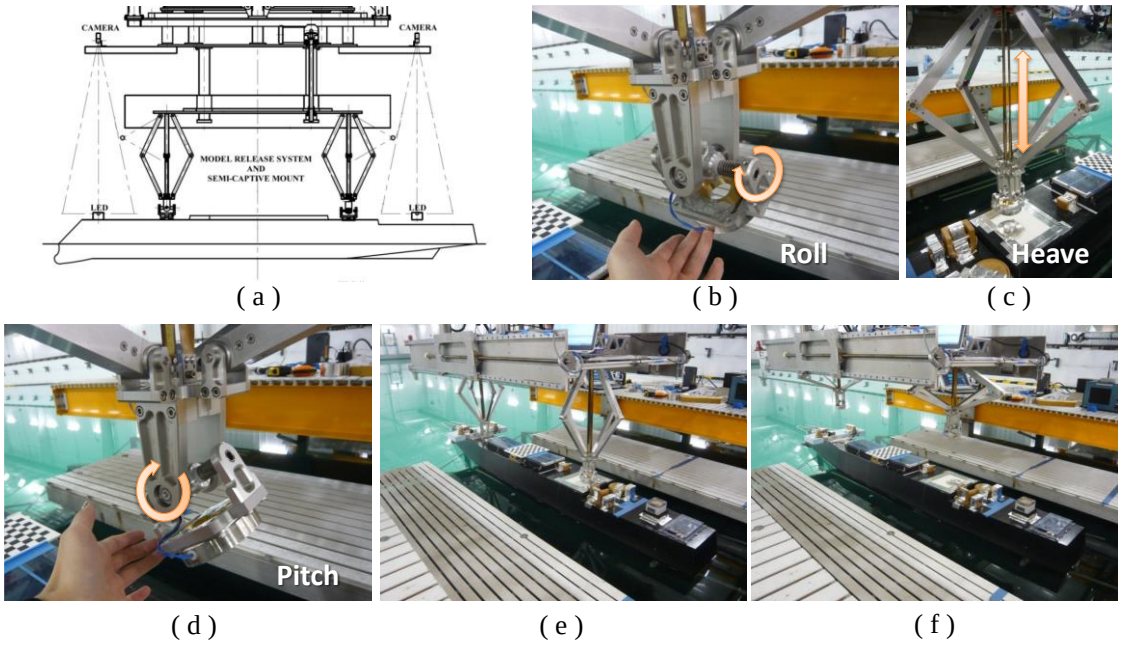

(a) (b) (c)

(d) (e) (f)

Figure 2.13: The model release system and semi-captive mount: (a) sketch of model release system, (b) roll motion of semi-captive mount, (c) heave motion of semi-captive mount, (d) pitch motion of semi-captive mount, (e) model in semi-captive, and (f) model released

Source: (Sanada et al., 2013)

2.3 ONR Tumblehome Model

Free-running tests were performed with a 1/49 scale ONR Tumblehome model 5613 with a length of 3.147 meters. The model is representative of a full scale 154 meter pre-contract design for the U.S. Navy's DDG 1000 Zumwalt class destroyer. The model has full appendages including skeg and bilge keels, as well as rudder and propellers to allow for free-running tests. The metacentric height, GM, natural roll period, and radius of gyration were adjusted by inclining test, free roll decay, and swing test in accordance with Sadat-Hosseini et al. (2011). The coordinate system for the ship is setup such that the x-

axis points toward the bow, the y-axis is oriented towards the starboard side, and the z-axis points downward.

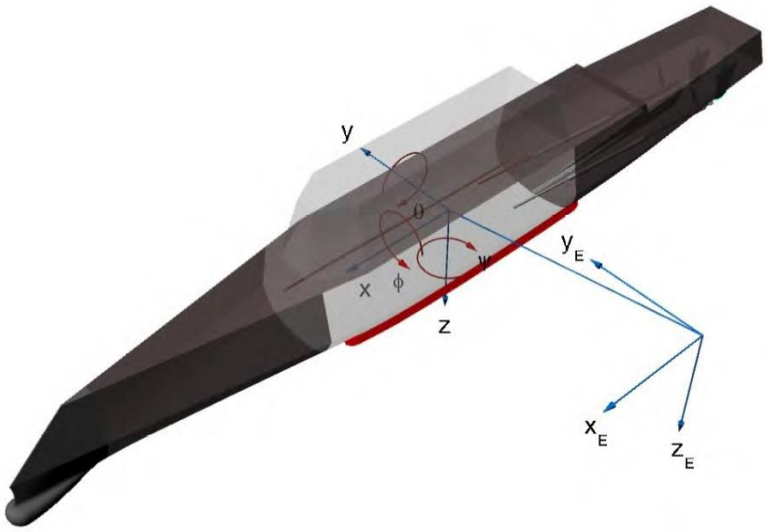

Figure 2.14: Tumblehome model with coordinate system

Source: (Cook, 2011)

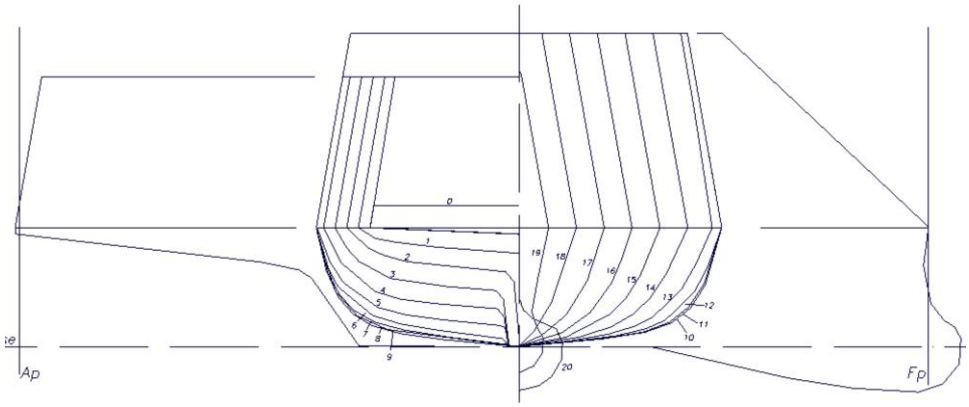

Figure 2.15: Tumblehome body plan and centerline profile

Source: (Sanada, 2013)

Figure 2.16: Experimental Tumblehome model bow

Source: (Sanada, 2013)

Figure 2.17: Experimental Tumblehome model stern

Source: (Sanada, 2013)

Table 2.1: Ship model and full scale dimensions

Main particulars		Model scale (1/49)	Full scale
Length of waterline	L_{WL} (m)	3.147 ± 0.001	154
Maximum beam of waterline	B_{WL} (m)	0.384 ± 0.001	18.78
Depth	D (m)	0.266	14.5
Draft	T (m)	0.112 ± 0.001	5.494
Displacement	Δ	72.6 ± 0.1 kg	8507 ton
Wetted surface area (fully appended)	S_0 (m^2)	1.5	NA
Block coefficient (CB)	$\nabla /(L_{WL}B_{WL}\ T)$	0.535	0.535
LCB	LCB (m) aft of FP	1.625	NA
Vertical Center of Gravity (from keel)	KG (m)	0.16 ± 0.02	NA
Metacentric height	GM (m)	0.042 ± 0.001	NA
Moment of Inertia	K_{xx}/B	0.444 ± 0.021	0.444
Moment of Inertia	K_{yy}/L_{WL}	0.25 ± 0.04	0.25
Propeller diameter	D_P (m)	0.1066	NA
Propeller center, long. location (from FP)	x/L_{WL}	0.9267	NA
Propeller center, lateral location (from CL)	$\pm y/L_{WL}$	0.02661	NA
Propeller center, vert. location (below WL)	$-z/L_{WL}$	0.03565	NA
Propeller shaft angle (downward positive)	ε (deg.)	5	NA
Propeller rotation direction (view from stern)		inward	inward
Maximum rudder rate		35.0 deg./s	
Natural Roll Period	T_ϕ (s)	1.644 ± 0.01	

2.4 Test Conditions

The analyzed tests were performed with the same initial settings through a variety of wave encounter angles and calm water. Course keeping tests were performed with headings of 0°, 45°, 90°, 135°, and 180°, representing head, following, beam, quartering,

and oblique waves. The model was free-running at a Froude Number of 0.2 while the wave conditions had values of 0.02 and 1.0 for wave steepness (H/λ) and wavelength to ship length ratio (λ/L) respectively. Each test was run 3 times to validate the repeatability.

Prior to the initial test the ship model was towed with the propeller spinning at a known rate of rotation. This rotation rate was set in such a way that there was no resulting force on the mount from the thrust of the propellers causing enough forward force to overcome the resistance of the water. Once the propeller rotational rate was determined, calm water tests with a straight heading were performed to determine the sinkage, trim, and verify the rotational speed of the propeller for the desired Froude Number. The calm water tests were initialized closest to the beach heading toward the wave makers, with the model initially mounted to the sub-carriage. The sub-carriage carried the model to the desired speed before release to reduce the amount of space needed for acceleration. The model is self-propelled with a constant heading towards the wave makers. The tests concluded when the model reached the end of the tracking area before being manually controlled to return to the start position.

For tests with waves the ship model began mounted with the propellers spinning at the predetermined rate. The sub-carriage maneuvered the model to the desired starting position depending on heading of the ship, an example of this is having the test start near the wave makers with a heading towards the beach for following waves. Once in position the model remained stationary until the wave propagated through half of the length of the basin before the model was accelerated to speed, corresponding to the desired Froude Number. The model was then self-propelled with the propellers maintaining their rotational speed and the rudders controlling the heading in course keeping cases.

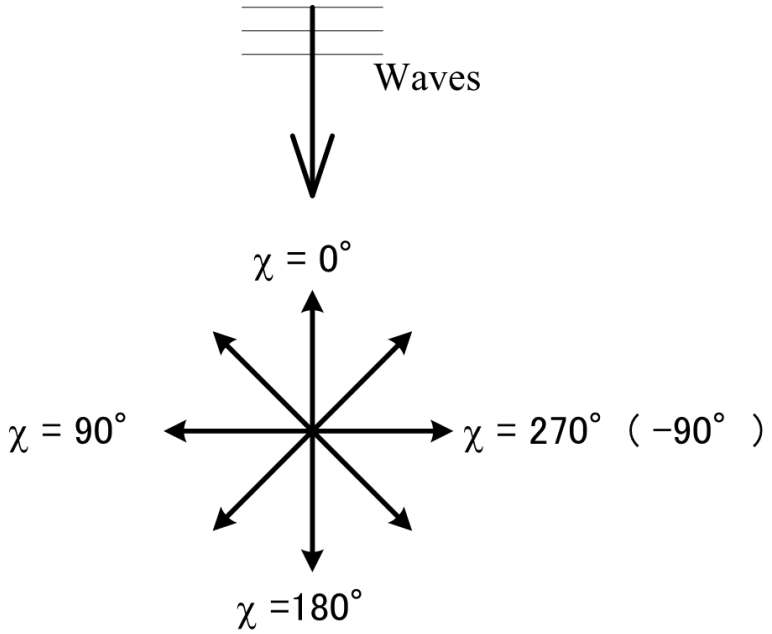

Figure 2.18: Relationship between ship heading and wave angle

Source: (Sanada et al., 2014)

In addition to the course keeping tests, turning circle and zig zag tests are performed to assess the maneuverability of the ship design. From these two tests five key maneuverability measurements are found. These include the transfer, advance, tactical diameter, and first and second overshoot angles. The turning circle tests operate by having the model travel in a straight line at steady state before turning the rudders to 35 degrees. The model then completes three circles with the transfer, advance, and tactical diameter being found. The transfer is the y-distance traveled between the rudder angle being changed and the ship heading changing 90 degrees. The advance is measured at the same location as the transfer but measures the change in x-distance traveled. The tactical diameter is the y-distance traveled to reverse the models heading to 180 degrees from its initial position.

The 10/10 zigzag tests operate with the model traveling at a steady state before engaging the rudder to positive 10 degrees. The model travels until it reaches a heading of 10 degrees before reversing the angle of the rudder to -10 degrees. The model then continues its course until a heading of negative 10 degrees is achieved. Once the heading of negative 10 degrees is achieved the rudder is then changed back to positive 10 degrees. The first overshoot angle is measured as the 10 degree intended heading angle subtracted from the maximum heading achieved. Similarly the second overshoot angle is found by subtracting the execute heading (-10 degrees) from the maximum negative heading measured as defined by the American Bureau of Shipping (2006). In addition to the first and second overshoot angles for the 10/10 zigzag test the first overshoot angle during a 20/20 zigzag test were found. Both the two overshoot angles, the transfer, advance, and tactical diameter are required to determine the overall maneuverability of the model. These maneuverability measurements correspond to the requirements defined in IMO 2004 for standard for ship maneuverability comparing the measurements to the ship length of the model.

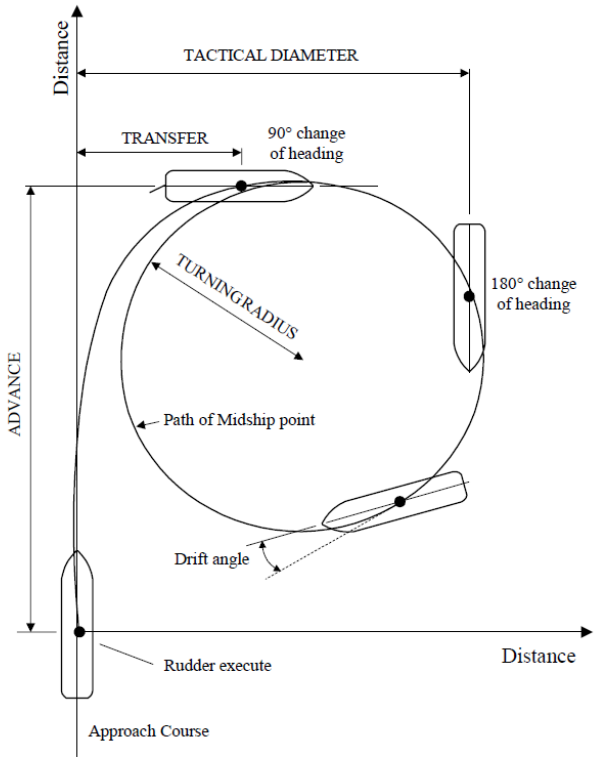

Figure 2.19: Advance, transfer, and tactical diameter definitions

Source: The American Bureau of Shipping (ABS) maneuvering guide (2006)

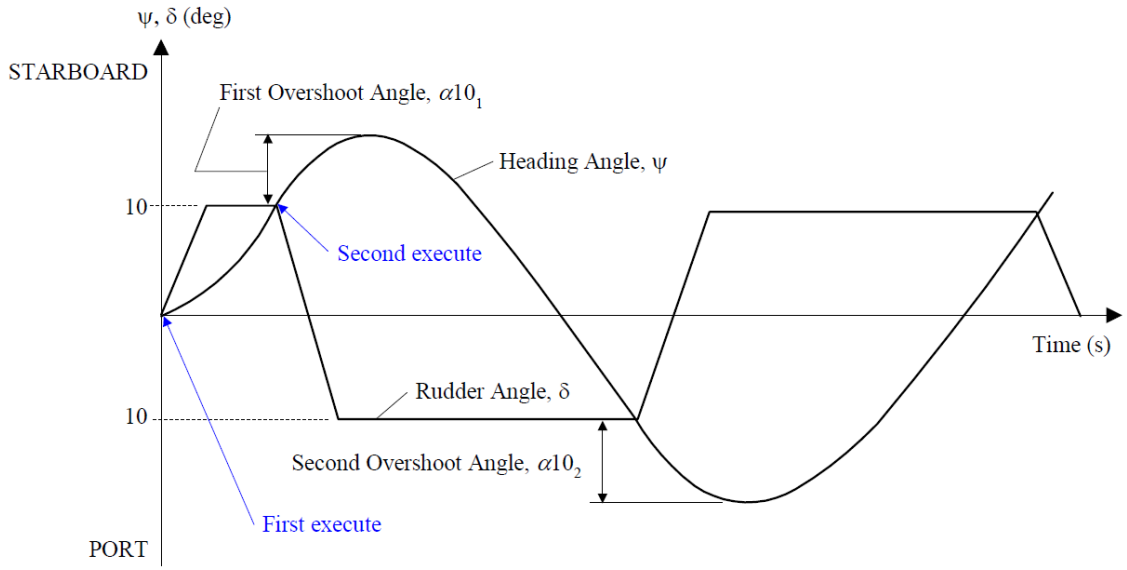

Figure 2.20: Overshoot angles definition

Source: The American Bureau of Shipping (ABS) maneuvering guide (2006)

The measured quantities during maneuvering and turning circle tests are evaluated by IMO criteria to estimate ship maneuvering performance of the finished design. These criteria are in place to ensure that the design is capable of turning, stopping, and maneuvering in a way that collisions can be avoided and ensure that the ship handles correctly around obstacles. The values of requirements with the definitions and the maneuver used to evaluate the criteria can be seen in table 2.2. Within the definitions L, V, AD, TD, α , and ℓ represent the ship length, speed, advance, transfer, overshoot angle, and distance traveled respectively.

Table 2.2: Overview of standards and criteria

Measure of Maneuverability	Criteria and Standard	Maneuver	IMO Standard	ABS Guide Requirement
Required for Optional Class Notation				
Turning Ability	Tactical Diameter	Turning Circle	$TD < 5L$	Rated $R_{td} \geq 1$
	Advance		$AD < 4.5L$	Not Rated $AD < 4.5L$
Course Changing and Yaw Checking Ability	First Overshoot Angle	10/10 Zig-zag Test	$\alpha 10_1 < f_{101}(L/V)$	Rated $R_{t\alpha_{10}} \geq 1$
	Second Overshoot Angle		$\alpha 10_2 < f_{102}(L/V)$	Not Rated $\alpha 10_2 < f_{102}(L/V)$
	First Overshoot Angle	20/20 Zig-zag Test	$\alpha 20_1 \leq 25$	Rated $R_{t\alpha_{20}} \geq 1$
Initial Turning Ability	Distance traveled before 10-degrees course change	10/10 Zig-zag Test	$\ell_{10} \leq 2.5L$	Rated $R_{ti} \geq 1$
Stopping Ability	Track Reach	Crash Stop	$TR < 15L$	Not Rated $TR < 15L$
	Head Reach		None	Rated $R_{ts} \geq 1$
Recommended, Not Required for Optional Class Notation				
Straight-line Stability and Course Keeping Ability	Residual turning rate	Pull-out test	$r \neq 0$	Not Rated $r \neq 0$
	Width of instability loop	Simplified spiral	$\alpha_U \leq f_u(L/V)$	Not Rated $\alpha_U \leq f_u(L/V)$

Source: The American Bureau of Shipping (ABS) maneuvering guide (2006)

The measured values for each test include times histories of the trajectories, roll, pitch, yaw, propeller revolution, rudder angle, and velocities. The position of the ship is defined within a global coordinate system and a model fixed coordinate system with X_0 and Y_0 representing the global location, and x and y representing the ship model coordinate system. Rudder angle, drift angle and roll angle are reported in ship coordinate system while the yaw angle is the same in both coordinate systems. The tests cases that were completed can be seen in Table 2.3 with the cases that were analyzed for uncertainty highlighted in red or blue representing cases for NATO AVT-183 and CFD Tokyo Workshop 2015 or maneuverability testing respectively.

Table 2.3: Maneuvering test cases in calm water and waves

T2015 Case
Included in Thesis

	Test	Fr*	δ [deg]	ψ_c** [deg]	H/ λ	λ/L	χ [deg]	Number of runs	
Calm water	Course keeping	0.2	N/A	**0**, 180				6	**Case 3.9**
				± 45, ± 135				12	
				± 90				6	
	Zigzag	0.2	10	10			**0**,180	6	
			20	20				6	
			35	35, 90				6	
	Turning circle	0.1	± 35	N/A			0	10	
		0.2					**0**, ± 90, 180	31	
		0.3					0	10	
Head Wave	Course keeping	0.2	N/A	0	0.02	0.5	0	3	**Case 3.12**
						1		3	
						1.2		3	
	Zigzag	0.2	10	10	0.02	0.5,1.0, 1.2	**0**	9	
			20	20		0.5,1.0,1.2		9	
			35	35		0.5,1.0, 1.2		9	
	Turning circle	0.1	± 35	N/A	0.02	0.5,1.0,1.2	0	30	
		0.2				0.5,1.0, 1.2	**0**, ± 90, 180	99	
		0.3				0.5, 1.0	0	20	
Following waves	Course keeping	0.2	N/A	180	0.02	0.5	180	3	**Case 3.13**
						1		3	
						1.2		3	
	Zigzag	0.2	10	10	0.02	0.5,1.0, 1.2	180	9	
			20	20		0.5,1.0, 1.2		9	
			35	35	0.02,0.03	0.5,1.0,1.2		18	
Beam wave	Course keeping	0.2	N/A	± 90	0.02	0.5	± 90	6	**Case 3.13**
						1		6	
						1.2		6	
Quartering wave	Course keeping	0.2	N/A	± 45, ± 135	0.02	0.5	± 45, ± 135	12	**Case 3.13**
						1		12	
						1.2		12	

Fr*: the nominal Froude Number.
ψ_c**: the target yaw angle.

2.5 Data Reduction Equations

During each test run a large amount of data is collected from the combination of the three tracking systems. In order to compare the different systems the sampling rates must be synchronized as well as the coordinate systems must be converted to ship coordinate system. The synchronization software is used to account for the 20 Hz sampling rate of the free-running and carriage system while the 6DOF-VMCS uses a 30 Hz sampling rate. By using the synchronization as well as other C++ codes the data is combined and modified to allow for plotting. The files produced are edited in Tecplot to draw time histories of the ship's position, speed, rudder angle, trajectory, propeller revolution, velocity components, drift angle, yaw, roll, pitch, yaw rate, and heave motion. In test cases with multiple runs these values are plotted together to demonstrate the repeatability of the tests.

In order to compare the measured values to other ship model results the measured values must be non-dimensionalized. This is done by dividing the measured value by the ship length, ship speed, wave amplitude, wave number, or some combination of these variables. When reporting the position of the model, the deviation from the sub-carriage to the ship center of gravity reported by the 6DOF-VMCS is used, due to the increased accuracy over the LED marker tracking system. The ship position is reported as the sum of the carriage position and the deviation multiplied by the respective carriage reported angles resulting in an x or y distance. The yaw angle can be found by adding the turntable angle with the deviation angle. These calculations can be seen in equations (2.1), (2.2), and (2.3). The x and y position are non-dimensionalized by dividing by ship length while the yaw angle is non-dimensionalized by dividing by wave amplitude and wave number.

$$\frac{X(t)}{L} = \frac{CPX + DPX\cos(CPT) - DPY\sin(CPT)}{L} \tag{2.1}$$

$$\frac{Y(t)}{L} = \frac{CPY + DPX\sin(CPT) - DPY\cos(CPT)}{L} \tag{2.2}$$

$$\frac{\psi(t)}{Ak} = \frac{\psi g}{A(2\pi f_p)^2} = \frac{(CPT + DPT)g}{A(2\pi f_p)^2} \tag{2.3}$$

The heave of the ship is measured by the 6DOF-VMCS and non-dimensionalized by dividing by the wave amplitude. This calculation can be seen in equation (2.4). The reported heave has an accuracy of ± 0.2 mm.

$$\frac{z(t)}{A} \tag{2.4}$$

The roll and pitch angles are also measured by the 6DOF-VMCS with an accuracy of ± 0.02 degrees. The measured values are non-dimensionalized by dividing by the wave number and wave amplitude as seen in equations (2.5) and (2.6) representing roll and pitch respectively.

$$\frac{\phi(t)}{Ak} = \frac{g\phi}{A(2\pi f_p)^2} \tag{2.5}$$

$$\frac{\theta(t)}{Ak} = \frac{g\theta}{A(2\pi f_p)^2} \tag{2.6}$$

The velocity components of the ship is obtained by measuring the change in both x and y position across two time steps to report the instantaneous x and y velocities. Once the instantaneous velocities are obtained in global coordinates, the ship speed, surge velocity, and sway velocity are calculated. The ship speed is the overall speed of the ship model while the surge and sway velocities represent the x and y velocities. The surge and sway velocities are non-dimensionalized by dividing the respective velocity by the ship speed as seen in equations (2.7) and (2.8). The combination of the two velocities represents the ship speed.

$$\frac{u}{U} = \frac{\frac{dx}{dt}\cos\psi + \frac{dy}{dt}\sin\psi}{\sqrt{\left(\frac{dx}{dt}\right)^2 + \left(\frac{dy}{dt}\right)^2}} \tag{2.7}$$

$$\frac{v}{U} = \frac{\frac{dy}{dt}\cos\psi - \frac{dx}{dt}\sin\psi}{\sqrt{\left(\frac{dx}{dt}\right)^2 + \left(\frac{dy}{dt}\right)^2}} \tag{2.8}$$

$$\frac{U}{U_0} = \frac{\sqrt{\left(\frac{dx}{dt}\right)^2 + \left(\frac{dx}{dt}\right)^2}}{U_0} \tag{2.9}$$

The wave elevation was measured near the bow of the ship model. This value was used to know the true size of the wave that the model was encountering. The wave elevation was non-dimensionalized by dividing by the ship length. Only the first harmonic frequency and phase were analyzed for the wave elevation since the higher order harmonic components can be neglected.

$$\frac{\zeta(t)}{L} \tag{2.10}$$

During calm water tests the sinkage, trim, and propeller speed were evaluated to compare to the captive results. These values are measured in calm water to determine the values used in computational simulations. The trim is reported as the measured pitch angle (represented by τ), the sinkage is the change in the height of the center of gravity from resting to traveling at the desired speed, and is non-dimensionalized by dividing by the ship length, and the propeller speed was reported in revolutions per minute. The propeller speed was calculated by dividing the computer settings and physical geometries by the count from the photo sensor. These settings and geometries include the microcomputer base clock frequency (PCLK), the microcomputer clock frequency divider (DIVD), the number of slits on the shaft to be read by the photo sensor (PRkp), and the gear ratio of the motor and propeller (PRkg). The settings are constant throughout a set of trials if the same computer and motor configuration is used, resulting in the propeller speed being simplified to a constant divided by the count from the photo sensor. A positive sinkage value represents a raised center of gravity while traveling at the desired speed, while a positive trim value represents the bow being lower than the stern of the ship.

$$\frac{\sigma}{L} \tag{2.11}$$

$$n = \frac{60\left(\frac{PCLK}{DIVD}\right)\left(\frac{PRkp}{PRkg}\right)}{count} = \frac{constant}{count} \tag{2.12}$$

The combination of these values are used to describe the ship motions during experimental trials and allow for comparisons to both computational simulations as well as other scale model and full scale tests.

CHAPTER 3: UNCERTAINTY ANALYSIS

The reported measurement error represents the accounted difference between the measured value and the true value of the measurement. The actual deviation between these two cannot be known due to the inability to measure the true value. The difference between the true value and the measured value is represented by the total error, this total error also cannot be known but can be approximated by reporting the combined uncertainty which is made up of both systematic and random error. The current uncertainty analysis is based on the ASME Performance Test Codes (PTC 19.1-2013) for Test Uncertainty.

3.1 Combined Uncertainty

The combined uncertainty is made up of both the random uncertainty as well as the systematic standard uncertainty. These two uncertainties are made up of the variance between repeated measurements and the limited accuracy of the measuring system. The combined uncertainty is calculated by finding the square root of the sum of the random and systematic uncertainties squared.

$$u_r = \sqrt{s_{\bar{r}}^2 + b_r^2} \tag{3.1}$$

Where $s_{\bar{r}}$ and b_r represent the random and systematic uncertainty for the variable r. The expanded uncertainty is calculated by multiplying the combined uncertainty by the expansion factor. The expansion factor is based on a normal t-distribution with a large

enough sample size where t_{95} is approximately 2 when observing a 95% confidence interval.

$$U_{r,95} = t_{95} \cdot u_r \tag{3.2}$$

The estimated expanded uncertainty represents a 95% confidence level that the true value of the measurement falls within $U_{r,95}$ of the measured average value. The range accounts for the calculated expanded uncertainty greater than and less than the average measurement found.

$$\bar{r} \pm U_{r,95} \tag{3.3}$$

3.2 Systematic Standard Uncertainty

In order to analytically calculate the standard uncertainty of a measurement, the measurement system must be fully analyzed to account for all sources of error within the measurement. Within ITTC procedure this value is reported as the "Type B" uncertainty. According to the current ASME performance test codes for test uncertainty, the effect of the systematic standard uncertainty will always have an effect on the final measurement even if an infinite number of measurement were taken. The influence of the systematic standard uncertainty is calculated based on the influence of elemental systematic errors. If random error did not exist to alter the result while standard uncertainty was still present the measured values from repeated tests would not change.

An analytical approach to approximate the standard uncertainty can be taken when a mathematical relationship exists between the known parameters and the result, this can often be in the form of a data reduction equation (DRE). This relationship allows for the sensitivity coefficient to be found through partial differentiation. The sensitivity coefficient represents the rate of change in the result when a change in a specific parameter occurs. In addition to the analytical approach to find sensitivity coefficients a numerical approach can also be represented by selecting a known change in a parameter to calculate the change in the resulting variable.

The systematic uncertainty is found using both sensitivity coefficients and individual systematic uncertainties for each variable within the data reduction equation. The sensitivity coefficient multiplied by the individual bias limits are added together to find the square of the systematic standard uncertainty. This equation applies if there are only uncorrelated uncertainties. The variable r represents the non-dimensional reported variable that is calculated based on a function of x_i variables.

$$r = r\left(x_1, x_2, ..., x_i\right) \tag{3.4}$$

$$b_r^2 = \sum_{i=1}^{J} \theta_{x_i,r}^2 b_{x_i}^2 + 2\sum_{j=1}^{J-1} \sum_{k=j+1}^{J} \theta_{j,r}\theta_{k,r} b\left(x_j, x_k\right) \tag{3.5}$$

If the variables are uncorrelated the systematic uncertainty is reduced to:

$$b_r^2 = \sum_{i=1}^{J} \theta_{x_i,r}^2 b_{x_i}^2 \tag{3.6}$$

The term θ_{x_i} represents the sensitivity coefficient based on the data reduction equation. This value is computed by analytically finding the partial derivative of r in terms of x_i. The sensitivity coefficient represents the rate of change with which the result changes based on a known change in input.

$$\theta_{x_i,r} = \frac{\partial r}{\partial x_i} \tag{3.7}$$

The systematic standard uncertainty can be improved by increasing the quality of the reported variables. This can be done by a combination of improved setup, improved measurement systems, and tighter tolerances on the test model.

3.3 Random Uncertainty

To calculate the random standard uncertainty of the resulting variable the standard deviation must be found of the sample set. This value is reported as the "Type A" uncertainty within ITTC procedure and the ISO Guide to the Expression of Uncertainty in Measurements. The effect of random elemental errors on a measurement results in random scatter of the data near the mean value of repeated trials. When an infinite amount of measurements are taken the sample mean would represent the true population mean of the measurement. An infinite amount of samples is not feasible in testing so the sample mean is reported with the sample standard deviation, where the sample standard deviation plays a large role in calculating the random uncertainty.

When repeated tests were taken, the sample standard deviation calculates the sum squared difference of the mean value subtracted from each individual measurement. This value is divided by M, the total number of data points. The square root of this value represents the standard deviation. These calculated standard deviations represent the variability of the measurement and the random errors that effect the measurement. The standard deviation is not affected by the measurement system and will always remain present even with an essentially perfect measurement system.

$$\bar{r} = \frac{1}{M}\sum_{n=1}^{M} r_n \tag{3.8}$$

$$s_r = \sqrt{\frac{\sum_{n=1}^{N}\left(r_n - \bar{r}\right)^2}{M}} \tag{3.9}$$

The random standard uncertainty is calculated by dividing the standard deviation by the square root of the total number of measurements.

$$s_{\bar{r}} = \frac{s_r}{\sqrt{M}} \tag{3.10}$$

3.4 Uncertainty Reporting

When reporting the uncertainties the expanded uncertainty does not fully describe the dataset. In order to have an understanding of how large the uncertainty is in relation to the measured values, percentages of the harmonic amplitudes or percentage of the range of phase are used. When analyzing the uncertainty of harmonic amplitudes the systematic

standard, random, combined, and expanded uncertainties are reported as percentages of the amplitude to allow for a better understanding of the scale of the uncertainties. Additionally the systematic standard and random uncertainties are reported as percentages of the combined uncertainty to better analyze what is the main source of uncertainty. Similarly the individual contributions of the measurement systems used are compared to the systematic standard uncertainty to verify where to improve if the systematic standard uncertainty is a larger contributor than the random uncertainty. Similarly to the amplitudes when analyzing phases the systematic standard, random, combined, and expanded uncertainties are compared to the full scale of the possible phase shifts (2π) to allow for a better comparison.

3.5 Individual Error Sources

Through the combination of the various tracking systems a variety of error sources exist. These error sources include the accuracies of the tracking systems themselves, as well as facility biases and calculation uncertainties. Table 3.1 shows the various maximum deviations for the different tracking systems which result in the individual systematic uncertainties. The calculations of these different uncertainties can be seen in the Appendix A. The individual systematic uncertainties are used alongside the sensitivity coefficients to calculate the uncertainty from each measurement. With the tracking system, facility, and calculations remaining nearly constant throughout the series of tests these values do not change with the change in test conditions. The change in test conditions results in a change of the resultant standard uncertainty by altering the data reduction equation but does not cause a change within the individual systematic uncertainties. The individual systematic

uncertainties cause the resultant standard uncertainty to remain constant through an infinite amount of the same test process. The variables analyzed as individual systematic uncertainties represent the values that are directly measured during the test in their dimensionalized original form. The values from these measurements are manipulated with data reduction equations to report non-dimensional values to compare different sized models and full scale designs.

The individual error sources are calculated based on the combination of error sources involved in measuring the individual measurements. The uncertainties of the measurement are combined by finding the root-sum-square of the elemental systematic uncertainties. The total uncertainty represents the resulting uncertainty from the combination of error sources contributing to the measurement. An example of this is demonstrated by the X-position being found through the combination of the carriage position and the deviation from the carriage. The reported individual systematic uncertainty for X-position and other measured values can be seen in Table 3.1 with the calculations that contributed to these values located in the Appendix A.

$$\bar{b_r} = \left[\sum_{k=1}^{K} \left(\bar{b_{x_k}} \right)^2 \right]^{1/2} \tag{3.11}$$

Table 3.1: Individual systematic uncertainties

ζ	Wave Elevation	b_ζ	m	0.0006
L	Ship Length	b_L	m	0.0001
X	X-position	b_X	m	0.0029
Y	Y-position	b_Y	m	0.0029
z	Heave	b_z	m	0.0002
ϕ	Roll	b_ϕ	deg	0.02
θ	Pitch	b_θ	deg	0.02
ψ	Yaw	b_ψ	deg	0.02
f_p	Plunger frequency	b_{f_p}	Hz	0.01
A	Desired wave amplitude	b_A	m	0.00
g	Gravitational constant	b_g	m/s^2	0.00
dx/dt	Instantaneous X-velocity	$b_{dx/dt}$	m/s	0.01
dy/dt	Instantaneous Y-velocity	$b_{dy/dt}$	m/s	0.01

3.6 Uncertainty Propagation Analysis

Each source of error has an effect on the reported result through an experiment. Some of these measurement have larger affects than others but all must be approximated to determine the overall effect of each contribution. The wave and calm water cases have differing results due to the effects of waves and the different methods that these values are reported as harmonic motions or mean values measured across a steady state. The following figures display the propagation of uncertainties and their key contributors on the final results.

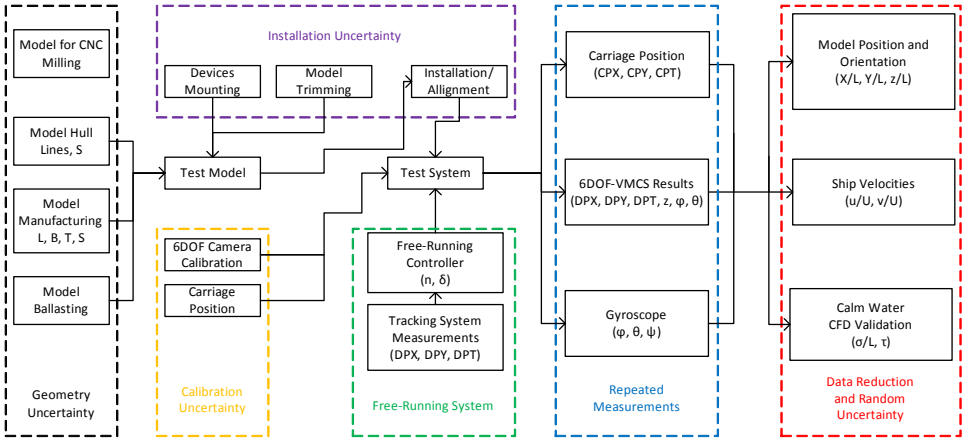

Figure 3.1: Calm water uncertainty propagation

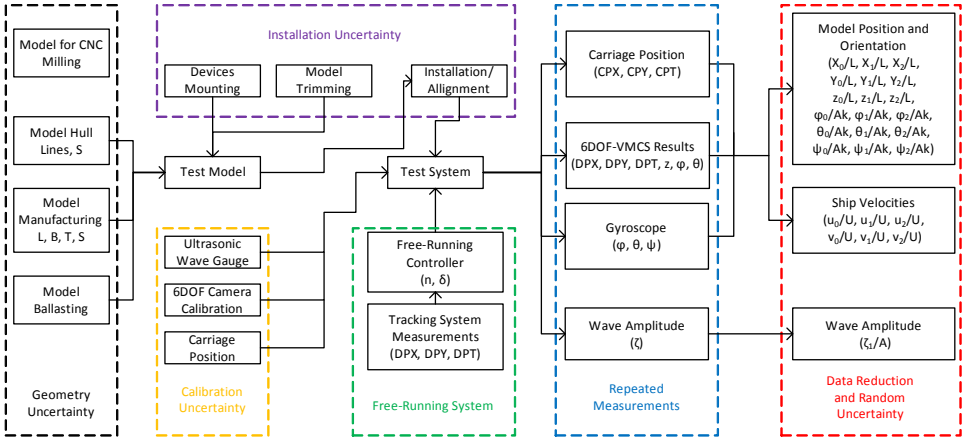

Figure 3.2: Uncertainty propagation in waves

3.7 Comparison to Previous Uncertainty Analysis

The method described for the tested model trials has not yet been completed in other free running studies. This method has been used for towed model test to find the individual bias limits (Force 2013). Force documentation focuses on the KRISO container ship (KCS) within head waves measuring the added resistance. Within the Force documentation the individual bias limits are found by analyzing the partial derivatives, from the DRE, to find the sensitivity coefficients and multiplying these values by their

respective uncertainty from the measurement tools used. The sum squared of these values is found to determine the individual bias limit of each measurement. The propagation of the uncertainty is found in this manner for all measurements taken.

Similar to Quadvlieg, 2011, Tonelli discussed the effects of deviations on the overshoot angles and advance when changes in the initial heading, initial speed, and yaw check angle, and drift angle to describe the sensitivity coefficients. Once the sensitivity coefficients are found the corrections on the outputted overshoot angle and advance are discussed. In addition to the sensitivities to the initial conditions the accuracy of the measurement system is briefly discussed but decided to be negligible because of the small inaccuracies within the measurement system used. A note is made about neglecting the measurement uncertainty because the repeatability tests caused a much larger uncertainty for the measurement system that is used (Tonelli, 2015).

Previous free running tests have analyzed only the repeatability of their trials. The resulting uncertainty is dependent on the random factors of the test but the systematic uncertainty is not accounted for (Elshiekh, 2014) as well as others. The underlying problems from this method is the effects of errors that occur through all the test cases. If the models heading is consistently read as a higher value than the actual measurement, all reported maneuverability characteristics would be incorrectly reported. Other issues would result in the inability to validate CFD results if inaccuracies from the systematic uncertainty cause a large deviation. With the inclusion of the systematic uncertainty the total uncertainty increases but has the added benefit of acknowledging what the largest contributors of uncertainty are. After acknowledgement it becomes possible to correct these errors to reduce the uncertainty of future tests.

CHAPTER 4: CALM WATER RESULTS AND DISCUSSIONS

Uncertainty assessment was performed on data collected for maneuvering characteristics in calm water and regular waves for ONR Tumblehome (Elshiekh 2014). The test cases observed include calm water and wave conditions operating at a Froude Number of 0.2. The measurements that are analyzed include X and Y-position, yaw, heave, pitch, roll, surge and sway velocity, and wave elevation for wave cases as well as sinkage, trim, and propeller speed for calm water tests. Additionally turning circle and zig zag tests were performed to determine the maneuverability characteristics of the Tumblehome model in both calm water and waves.

4.1 Calm Water Course Keeping Uncertainties

During calm water testing the sinkage, trim, and propeller speed were studied to verify captive cases and compare to CFD simulations. Three repeat tests were performed with a heading towards the wave makers (χ=0°).

4.1.1 Sinkage

The sinkage was found as the change in location of the vertical center of gravity from a resting position to traveling at the operational speed. This value was non-dimensionalized by dividing the measured value by the ship length.

$$\frac{\sigma}{L} \tag{4.1}$$

The sensitivity coefficients were found by finding the partial derivatives with respect to length and sinkage.

$$\theta_{z,\sigma/A} = \frac{\partial(\sigma / L)}{\partial(z)} = \frac{1}{L} \tag{4.2}$$

$$\theta_{L,\sigma/L} = \frac{\partial(\sigma / L)}{\partial(L)} = -\frac{z}{L^2} \tag{4.3}$$

From the combination of the sensitivity coefficients and the individual bias limits, found previously, the systematic uncertainty can be found as well as the random, combined, and expanded uncertainties.

$$b_{\sigma/L} = b_\sigma^2 \theta_{\sigma,\sigma/L}^2 + b_L^2 \theta_{L,\sigma/L}^2 \tag{4.4}$$

The measured sinkage has an uncertainty of 20% of the measurement which is higher than the ideal uncertainty. This is largely made up of the systematic standard uncertainty related to the measurement from the 6DOF-VMCS and the uncertainty in the ship length with the majority coming from the uncertainty involved with the depth of sinkage.

Table 4.1: Sinkage uncertainty values in calm water

Mean σ / L	0.0006
$\theta_\sigma^2 \cdot b_\sigma^2$ $\%b_{\sigma/L}^2$	100.00
$\theta_L^2 \cdot b_L^2$ $\%b_{\sigma/L}^2$	0.00
b_σ $\%\overline{\sigma / L}$	9.85
$s_{\overline{\sigma}}$ $\%\overline{\sigma / L}$	0.98
u_σ $\%\overline{\sigma / L}$	9.95
$b_{\sigma/L}^2$ $\%u_{\sigma/L}^2$	99.01
$s_{\sigma/L}^2$ $\%u_{\sigma/L}^2$	0.99
$U_{95,\sigma/L}$ $\%\overline{\sigma / L}$	20.00

4.1.2 Trim

The trim is found by comparing the height of the bow to the height of the stern. From these two values the trim can be calculated and represented with a lower bow representing a positive trim value. The trim is presented as a dimensional value with the units of degrees. The uncertainty associated with the trim is more than 130% of the measured with the systematic standard uncertainty representing the larger portion. This large uncertainty is due to the fact that the accuracy of the 6DOF-VMCS is capable of reporting the trim within 0.02 degrees and the measured trim is the same magnitude as this accuracy.

Table 4.2: Trim uncertainty values in calm water

Mean τ [deg]	0.03
$\theta_\tau^2 \cdot b_\tau^2$ $\%b_\tau^2$	100.00
b_τ $\%\bar{\tau}$	57.96
$s_{\bar{\tau}}$ $\%\bar{\tau}$	19.54
u_τ $\%\bar{\tau}$	67.12
b_τ^2 $\%u_\tau^2$	89.79
s_τ^2 $\%u_\tau^2$	10.21
$U_{95,\tau}$ $\%\bar{\tau}$	134.23

4.1.3 Propeller Revolutions

The ship speed is controlled by operating a set propeller speed determined by operating in calm water. This value is measured by a photo sensor measuring the count of rotations of the propeller in quarter rotations. The propeller speed can be measured within the range of 131.8 and 864000 rpm and is limited by the counting limitations of the computer within a set time period. To calculate the rotational rate the conversion factor (KPS) is found based on the computer base clock frequency (PCLK), clock frequency divider (DIVD), number of slits that the photo sensor can read (PRkp), and the gear ratio from the motor to the propeller (PRkg). The conversion factor is treated as a constant assuming that the same computer and propellers setup is used throughout the trials.

$$n = \frac{60\left(\frac{PCLK}{DIVD}\right)\left(\frac{PRkp}{PRkg}\right)}{count} = \frac{KPS}{count} \tag{4.5}$$

The sensitivity coefficient is found with respect to the measured count value with the uncertainty in count being represented by a rectangular distribution. The count can be estimated to an accuracy of ±1/2 and is divided by the square root of three to represent the rectangular distribution (ITTC, 2014c).

$$\theta_{count,n} = \frac{\partial(n)}{\partial(count)} = -\frac{60\left(\frac{PCLK}{DIVD}\right)\left(\frac{PRkp}{PRkg}\right)}{count^2} = -\frac{n}{count} \tag{4.6}$$

$$b_n^2 = b_{count}^2 \theta_{count,n}^2 \tag{4.7}$$

Analysis of the uncertainty associated with the propeller speed is initially performed analytically based on the sensitivity coefficient and individual bias limits.

Table 4.3: Propeller speed uncertainty values in calm water (Analytic standard uncertainty)

n [rpm] at Fr=0.2	538.11
b_n [rpm]	0.0097
s_n	0.3842
$s_{\bar{n}}$	0.2219
u_n	0.2221
$\frac{U_{95,n}}{\%\bar{n}}$	0.0825

If a numeric approach is taken instead of an analytic one, the measured motor speed during testing has a value of 538.1087 rpm. This value can be converted into the count by dividing the conversion factor by the propeller speed. By completing this division and rounding to the nearest integer, the count to maintain a Froude Number of 0.2 is 16056 counts per minute. With the knowledge that the count is accurate to within ±1 the range of count for this test is 16055 to 16057. These values result in a propeller speed range of 538.0831 to 538.1501 rpm. The range of these results is ±0.0335 rpm, a higher value than the analytically calculated uncertainty.

$$538.1166\ [\text{rpm}]: 8640000 / (16056 \pm 1) = 538.1166 \pm 0.0335\ [\text{rpm}] \quad (4.8)$$

The numerical approach should be used to calculate the estimated standard uncertainty due to the greater magnitude. The uncertainty values are reported to the $1/10000^{th}$ of a rotation per minute. This amount of precision was selected because of the count accuracy equating to ± 1 at approximately 16056 counts per minute resulting in the propeller speed being reported to a precision of $1/16056 = 0.0000623$.

Table 4.4: Propeller speed uncertainty in calm water (Numeric standard uncertainty)

b_n [rpm]	0.0335
s_n	0.3842
$s_{\bar{n}}$	0.2219
u_n	0.2244
b_n^2 $\%u_n^2$	2.63
s_n^2 $\%u_n^2$	97.37
$U_{95,n}$ $\%\bar{n}$	0.0834

In order to report the uncertainty of the propeller speed in rotations per second the measured values must be divided by 60. These scaled values are used for the mean, standard deviation, and numerical uncertainty values. The following tables show the calculated values with units of rotations per second. The rotation speed in rotations per second is reported to the 1/100th of a rotation per second due to the reduced precision when reporting across a lower time step.

$$n[rps] = \frac{n[rpm]}{60} = \frac{538.1087}{60} = 8.97 \tag{4.9}$$

$$b_n[rps] = \frac{b_n[rpm]}{60} = \frac{0.0335}{60} = 0.0006 \tag{4.10}$$

Table 4.5: Propeller speed uncertainty in calm water in rotations per second

n [rps]	8.97
b_n [rps]	0.0006
s_n	0.0064
$s_{\bar{n}}$	0.0037
u_n	0.0037
b_n $\%n$	0.0063
$s_{\bar{n}}$ $\%n$	0.0413
b_n^2 $\%u_n^2$	2.63
s_n^2 $\%u_n^2$	97.37
$U_{95,n}$ $\%\bar{n}$	0.0834

The calculated uncertainty from the numerical approach proved to be larger than the analytically found approach. In this case the larger uncertainty should be reported. Both systematic uncertainties are significantly smaller than the random uncertainty, causing only a small difference between the two calculated uncertainties. Both approaches cause a very small percent uncertainty at less than 1/10th of a percent of the mean.

4.1.4 Calm Water Course Keeping Conclusions

The propeller revolution speed is very accurately measured during calm water tests and reports a near zero percent uncertainty. The trim and sinkage report less accurate results due to the magnitude of measured values and the uncertainties involved with the

measurements being consistently similar. Both uncertainties for sinkage and trim are primarily made up of the systematic standard uncertainty displaying that the tests are very repeatable but the measurement system could use improvement if such low values for sinkage and trim are being measured. The initial ship speed has a significant amount of standard deviation after initial release due to the variability with initial conditions and the release from the carriage. During the course keeping test the maximum deviation from the intended paths were 0.0159, 0.0280, and 0.0466, for the three runs with the maximum deviation in the second run occurring in the negative Y-direction.

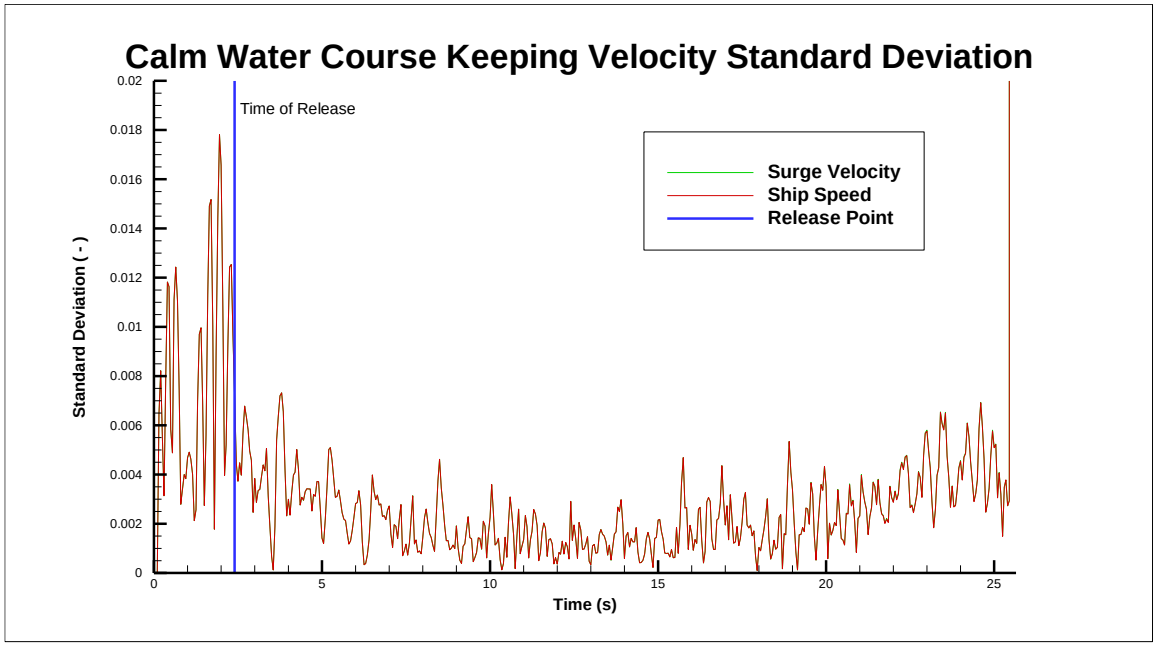

Figure 4.1: Calm water ship velocity standard deviations

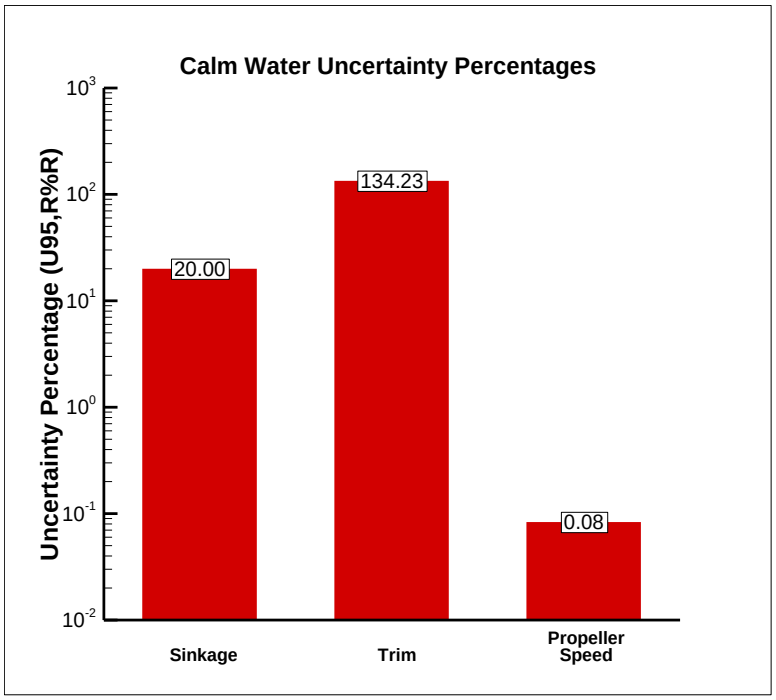

Figure 4.2: Calm water uncertainties

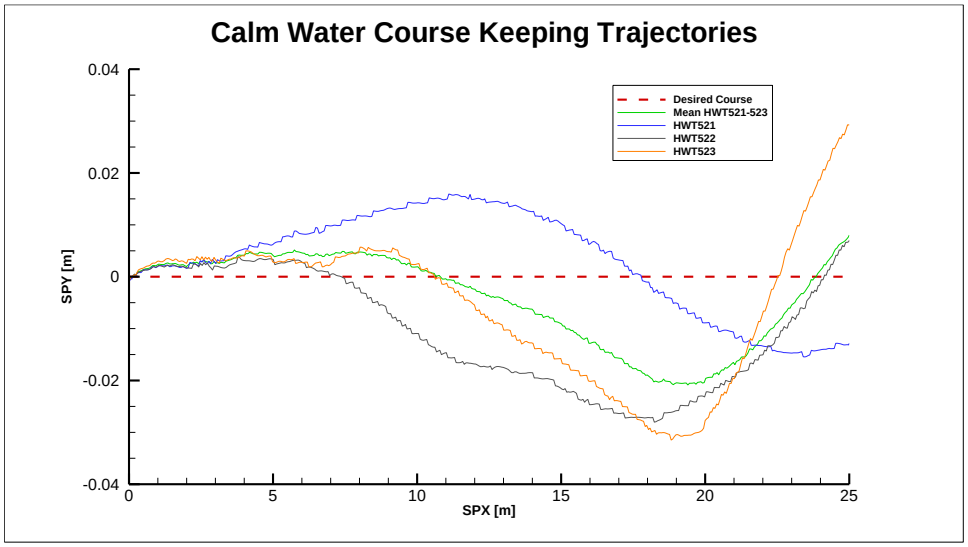

Figure 4.3: Calm water course keeping trajectories with the dashed line representing the desired course

4.2 Calm Water Zig Zag Uncertainties

Zig zag test were performed with rudder angles of 10°/10° to determine the maneuverability of the model. The X-position, Y-position, surge and sway velocity are analyzed for the zig zag maneuvers in addition to the first and second overshoot angles were also found and the uncertainty of these angles were analyzed. The overshoot angles represent the ability for the model to change directions when a rudder angle of ±10 degrees is executed. The process to find uncertainties of the position and velocities the process described in Chapter 3 is followed by determining the partial derivatives of the data reduction equation and manipulating these equations with the individual systematic uncertainties to find the combined and expanded uncertainties.

4.2.1 X-Position

The X-position of the model is determined based on the combination of the ship position and the carriage position. The position of the carriage (CPX) is added to the deviation from the center point of the sub-carriage to the center of gravity of the ship model (DPX and DPY). This deviation is adjusted based on the yaw angle of the sub-carriage (CPT) to accurately describe the position of the model within basin coordinates. The X-position of the model is divided by the ship length to non-dimensionalize.

$$\frac{X(t)}{L} = \frac{CPX + DPX\cos(CPT) - DPY\sin(CPT)}{L} \tag{4.11}$$

Partial derivatives are found for the length, carriage position, carriage yaw, and x and y-deviation from the sub carriage to determine the sensitivity coefficients for the X-position.

$$\theta_{CPX,X/L} = \frac{\partial(X/L)}{\partial(CPX)} = \frac{1}{L} \tag{4.12}$$

$$\theta_{DPX,X/L} = \frac{\partial(X/L)}{\partial(DPX)} = \frac{\cos(CPT)}{L} \tag{4.13}$$

$$\theta_{DPY,X/L} = \frac{\partial(X/L)}{\partial(DPY)} = -\frac{\sin(CPT)}{L} \tag{4.14}$$

$$\theta_{CPT,X/L} = \frac{\partial(X/L)}{\partial(CPT)} = -\frac{DPX\sin(CPT) - DPY\cos(CPT)}{L} \tag{4.15}$$

$$\theta_{L,X/L} = \frac{\partial(X/L)}{\partial(L)} = -\frac{CPX + DPX\cos(CPT) - DPY\sin(CPT)}{L^2} \tag{4.16}$$

To find the systematic standard uncertainty for the X-position the sensitivity coefficients and individual bias limits are combined by finding the sum squared of their multiplications.

$$b_{X/L}^2 = b_{CPX}^2\theta_{CPX,X/L}^2 + b_{DPX}^2\theta_{DPX,X/L}^2 + b_{DPY}^2\theta_{DPY,X/L}^2 + b_{CPT}^2\theta_{CPT,X/L}^2 + b_L^2\theta_{L,X/L}^2 \tag{4.17}$$

4.2.2 Y-Position

The Y-position is found the same manner as X-position, but uses the sub-carriage position (CPX) and y-deviation from the sub-carriage to calculate the overall position in basin-coordinates.

$$\frac{Y(t)}{L} = \frac{CPY + DPX\sin(CPT) - DPY\cos(CPT)}{L} \tag{4.18}$$

The sensitivity coefficients are found as follows:

$$\theta_{CPY,Y/L} = \frac{\partial(Y/L)}{\partial(CPY)} = \frac{1}{L} \tag{4.19}$$

$$\theta_{DPY,Y/L} = \frac{\partial(Y/L)}{\partial(DPY)} = -\frac{\cos(CPT)}{L} \tag{4.20}$$

$$\theta_{DPX,Y/L} = \frac{\partial(Y/L)}{\partial(DPX)} = \frac{\sin(CPT)}{L} \tag{4.21}$$

$$\theta_{CPT,Y/L} = \frac{\partial(Y/L)}{\partial(CPT)} = -\frac{DPX\cos(CPT) - DPY\sin(CPT)}{L} \tag{4.22}$$

$$\theta_{L,Y/L} = \frac{\partial(Y/L)}{\partial(L)} = -\frac{CPY + DPX\sin(CPT) - DPY\cos(CPT)}{L^2} \tag{4.23}$$

With the systematic standard uncertainty being calculated as:

$$b_{Y/L}^2 = b_{CPY}^2\theta_{CPY,Y/L}^2 + b_{DPY}^2\theta_{DPY,Y/L}^2 + b_{DPX}^2\theta_{DPX,Y/L}^2 + b_{CPT}^2\theta_{CPT,Y/L}^2 + b_L^2\theta_{L,Y/L}^2 \tag{4.24}$$

4.2.3 Surge Velocity

The surge velocity represents the ships velocity in the longitudinal direction. This is found by calculating the instantaneous change in the position in the x-direction. Once found this value is divided by the ship speed (found as the combined magnitude of surge and sway velocities) to be non-dimensionalized.

$$\frac{u}{U} = \frac{\frac{dx}{dt}\cos\psi + \frac{dy}{dt}\sin\psi}{\sqrt{\left(\frac{dx}{dt}\right)^2 + \left(\frac{dy}{dt}\right)^2}} \tag{4.25}$$

The partial derivatives of the surge velocity are found with respect to the instantaneous x-velocity (dx/dt), the instantaneous y-velocity (dy/dt), and the heading of the ship.

$$\theta_{\frac{dx}{dt},u/U} = \frac{\partial(u/U)}{\partial\left(\frac{dx}{dt}\right)} = \frac{\cos\psi}{\sqrt{\left(\frac{dx}{dt}\right)^2 + \left(\frac{dy}{dt}\right)^2}} - \frac{\frac{dx}{dt}\left(\frac{dx}{dt}\cos\psi + \frac{dy}{dt}\sin\psi\right)}{\left(\left(\frac{dx}{dt}\right)^2 + \left(\frac{dy}{dt}\right)^2\right)^{3/2}} \tag{4.26}$$

$$\theta_{\frac{dy}{dt},u/U} = \frac{\partial(u/U)}{\partial\left(\frac{dy}{dt}\right)} = \frac{\sin\psi}{\sqrt{\left(\frac{dx}{dt}\right)^2 + \left(\frac{dy}{dt}\right)^2}} - \frac{\frac{dy}{dt}\left(\frac{dx}{dt}\cos\psi + \frac{dy}{dt}\sin\psi\right)}{\left(\left(\frac{dx}{dt}\right)^2 + \left(\frac{dy}{dt}\right)^2\right)^{3/2}} \tag{4.27}$$

$$\theta_{\psi,u/U} = \frac{\partial(u/U)}{\partial(\psi)} = \frac{-\frac{dx}{dt}\sin\psi + \frac{dy}{dt}\cos\psi}{\sqrt{\left(\frac{dx}{dt}\right)^2 + \left(\frac{dy}{dt}\right)^2}} \tag{4.28}$$

With the systematic standard uncertainty being calculated by:

$$b_{u/U}^2 = b_{dx/dt}^2\theta_{dx/dt,u/U}^2 + b_{dy/dt}^2\theta_{dy/dt,u/U}^2 + b_{\psi}^2\theta_{\psi,u/U}^2 \tag{4.29}$$

4.2.4 Sway Velocity

Similarly to the surge velocity the sway velocity is found based on the instantaneous velocities though in this case with respect to the lateral motions of the ship model.

$$\frac{v}{U} = \frac{\frac{dy}{dt}\cos\psi - \frac{dx}{dt}\sin\psi}{\sqrt{\left(\frac{dx}{dt}\right)^2 + \left(\frac{dy}{dt}\right)^2}} \tag{4.30}$$

With the sensitivity coefficients represented as:

$$\theta_{dx/dt,v/U} = \frac{\partial(v/U)}{\partial\left(\frac{dx}{dt}\right)} = \frac{-\sin\psi}{\sqrt{\left(\frac{dx}{dt}\right)^2 + \left(\frac{dy}{dt}\right)^2}} - \frac{\frac{dx}{dt}\left(\frac{dy}{dt}\cos\psi - \frac{dx}{dt}\sin\psi\right)}{\left(\left(\frac{dx}{dt}\right)^2 + \left(\frac{dy}{dt}\right)^2\right)^{3/2}} \tag{4.31}$$

$$\theta_{dy/dt,v/U} = \frac{\partial(v/U)}{\partial\left(\frac{dy}{dt}\right)} = \frac{\cos\psi}{\sqrt{\left(\frac{dx}{dt}\right)^2 + \left(\frac{dy}{dt}\right)^2}} - \frac{\frac{dy}{dt}\left(\frac{dy}{dt}\cos\psi - \frac{dx}{dt}\sin\psi\right)}{\left(\left(\frac{dx}{dt}\right)^2 + \left(\frac{dy}{dt}\right)^2\right)^{3/2}} \tag{4.32}$$

$$\theta_{\psi,v/U} = \frac{\partial(v/U)}{\partial(\psi)} = \frac{-\frac{dy}{dt}\sin\psi - \frac{dx}{dt}\cos\psi}{\sqrt{\left(\frac{dx}{dt}\right)^2 + \left(\frac{dy}{dt}\right)^2}} \tag{4.33}$$

And the systematic standard uncertainty found by:

$$b_{v/U}^2 = b_{dx/dt}^2 \theta_{dx/dt,v/U}^2 + b_{dy/dt}^2 \theta_{dy/dt,v/U}^2 + b_{\psi}^2 \theta_{\psi,v/U}^2 \tag{4.34}$$

4.2.5 Ship Speed

The ship speed represents the magnitude of the combined velocities. The ship speed is non-dimensionalized by dividing by the nominal ship speed which relates to the desired Froude Number of 0.20.

$$\frac{U}{U_0} = \frac{\sqrt{\left(\frac{dx}{dt}\right)^2 + \left(\frac{dy}{dt}\right)^2}}{U_0} \tag{4.35}$$

The sensitivity coefficients of the ship speed are found with respect to the instantaneous x and y velocities and the desired ship speed.

$$\theta_{dx/dt,U/U_0} = \frac{\partial\left(U/U_0\right)}{\partial\left(dx/dt\right)} = \frac{\frac{dx}{dt}}{U_0\sqrt{\left(\frac{dx}{dt}\right)^2 + \left(\frac{dy}{dt}\right)^2}} \tag{4.36}$$

$$\theta_{dy/dt,U/U_0} = \frac{\partial\left(U/U_0\right)}{\partial\left(dy/dt\right)} = \frac{\frac{dy}{dt}}{U_0\sqrt{\left(\frac{dx}{dt}\right)^2 + \left(\frac{dy}{dt}\right)^2}} \tag{4.37}$$

$$\theta_{U_0,U/U_0} = \frac{\partial(U/U_0)}{\partial(U_0)} = -\frac{\sqrt{\left(\frac{dx}{dt}\right)^2 + \left(\frac{dy}{dt}\right)^2}}{U_0^2} \tag{4.38}$$

The systematic standard uncertainty is found as follows:

$$b_{U/U_0}^2 = b_{dx/dt}^2 \theta_{dx/dt,U/U_0}^2 + b_{dy/dt}^2 \theta dy + b_{U_0}^2 \theta_{U_0,U/U_0}^2 \tag{4.39}$$

4.2.6 Zig Zag Results

When Zig zag maneuvers were performed in calm water, large uncertainty values occurred for the sway velocity. With the sway velocity being essentially zero during calm water tests the comparison to the mean value reported very large uncertainties. The expanded uncertainty for this value was approximately 30 times the mean sway velocity but is still a value reported as zero when accounting for the accuracies and the correct amount of significant digits (0.0045 reported as 0.00).

Table 4.6: Calm water zig zag uncertainties

r	Mean	b_r %r	$s_{\bar{r}}$ %r	u_r %r	b_r^2 %u_r^2	s_r^2 %u_r^2	$U_{95,r}$ %r
X_1/L	2.2168	0.05	0.49	0.49	0.86	99.14	0.98
X_2/L	4.9600	0.02	0.22	0.22	0.84	99.16	0.44
Y_1/L	0.0860	1.16	2.30	2.57	20.27	79.73	5.14
Y_2/L	0.2695	0.37	0.36	0.52	51.15	48.85	1.03
ψ_1	12.31	0.16	0.38	0.41	15.64	84.36	0.82
ψ_2	-12.10	-0.17	-0.14	-0.22	56.68	43.32	-0.44
u/U_1	1.00	0.82	0.85	1.18	48.78	51.22	2.36
v/U_1	-0.03	-91.80	-18.08	-93.56	96.26	3.74	-187.12
u/U_2	0.95	0.86	0.03	0.62	190.24	0.20	1.25
v/U_2	0.05	53.64	102.03	102.23	27.53	99.61	204.45
$\alpha 10_1$	0.18	3.40	0.15	3.40	99.80	0.20	6.80
$\alpha 10_2$	2.31	0.13	2.01	2.01	0.39	99.61	4.02

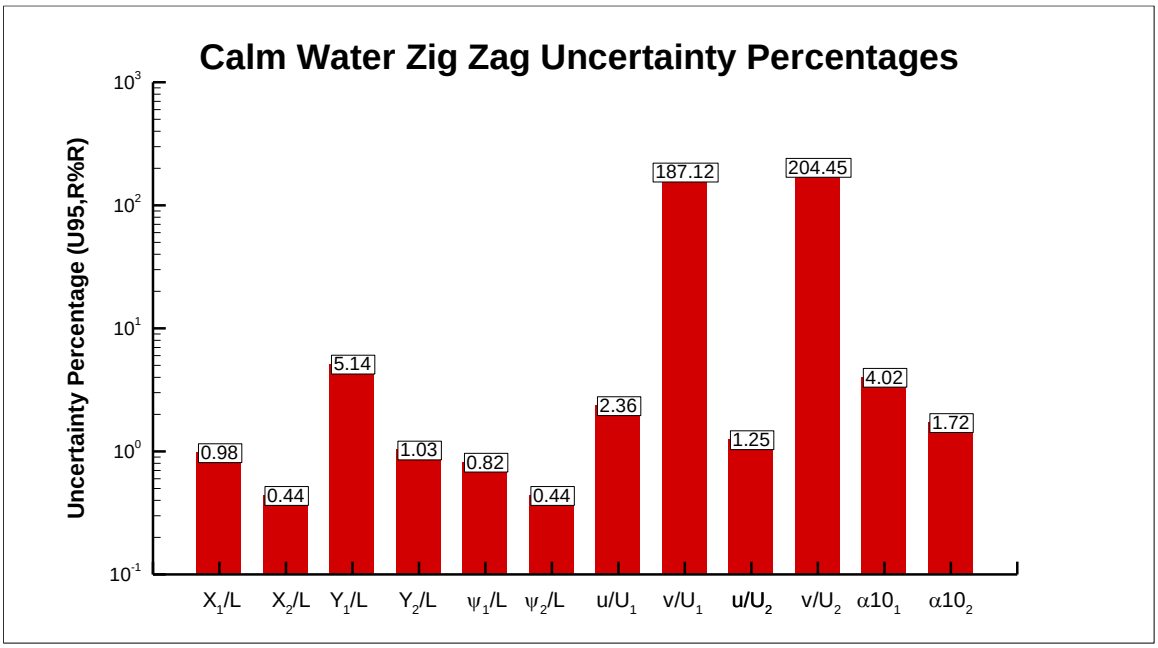

Figure 4.4: Uncertainties during calm water zig zag tests

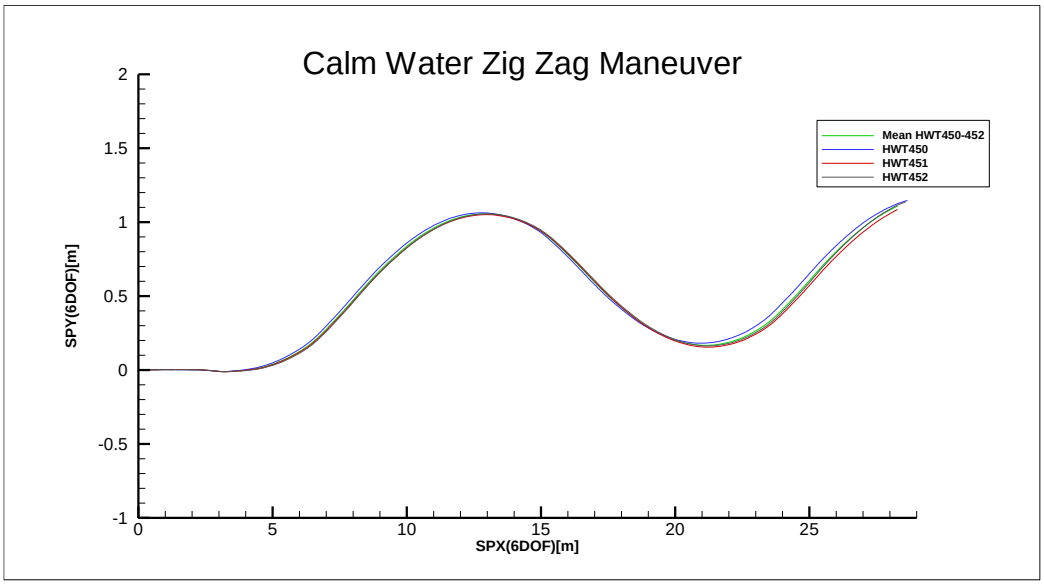

Figure 4.5: Zig Zag trajectory in calm water

When further analyzing the repeatability of the measurements the fluctuation of the ship speed and surge velocity were initially transient upon release but converged to a lower value after approximately 8 seconds. Variability is still present during this time but the lower value proved to be interesting. This initial transient can be due to many contributing factors. The ship is mounted to the sub-carriage during the initial 2.5 seconds of the trial and then released. From this point the consistency of the ship speed between trials increases which was an unexpected result. Contributing factors can include inconsistent carriage speed, the models initial mounting, and the variance in the propeller speed as well as others. Similarly to the course keeping test the standard deviation of the ship speed and surge velocity reduced to approximately 0 to 0.006 during the time of the maneuvers with an amount of extra noise when the rudder angle was changed. The larger deviations occur during rudder executions and decrease in value slower than the calm water case.

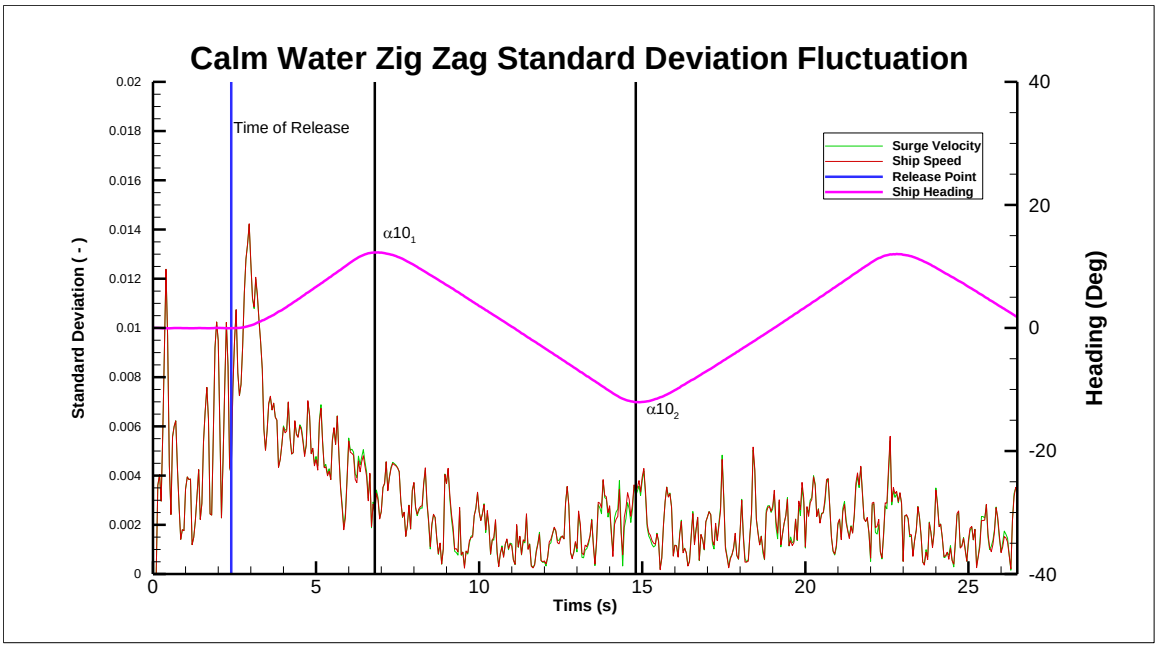

Figure 4.6: Standard deviation fluctuation during calm water zig zag maneuver

4.3 Calm Water Turning Circle Uncertainties

Turning circles were completed with an initial heading towards the wave maker with rudder angles of both positive and negative 35 degrees. These tests, similar to the zig zag test, judge the maneuverability of the ship model by analyzing the ability of the ship model to turn when transitioning from a straight heading to different degrees of heading. The advance (AD), transfer (TR), and tactical diameter (TD) are measured and non-dimensionalized by the ship length. These variables are measured when the ship heading of 90 (advance and transfer) or 180 (tactical diameter) degrees is reached. The advance measures the x-distance traveled before the 90 degree heading change, while transfer is measured at the same location but represents the y-distance traveled. The tactical diameter represents the y-distanced traveled for the ship to change from a 0 degree heading to 180 degrees. These values are then compared to IMO criteria to evaluate and class the

maneuvering characteristics of the ship (ABS, 2006). The uncertainties for the turning circles are calculated in the same manner as the zig zag maneuvers above.

When comparing the positive and negative 35 degree rudder angles, similar results are found as expected. The position and headings during at the locations of the advance, transfer, and tactical diameter as well as the measurements themselves were observed to find the uncertainties at these points. Between the two rudder angles the uncertainties were very comparable with the difference between the two primarily being due to the repeatability. Across all observed measurements except velocities the repeatability errors were the largest contributor to the combined uncertainty.

Table 4.7: Calm water turning circle uncertainties (δ=35)

r	Mean	b_r $\%r$	$s_{\bar{r}}$ $\%r$	u_r $\%r$	b_r^2 $\%u_r^2$	s_r^2 $\%u_r^2$	$U_{95,r}$ $\%r$
X_{AD}/L	7.5488	0.01	0.04	0.04	8.77	91.23	0.09
X_{TD}/L	6.3115	0.02	0.07	0.08	4.18	95.82	0.15
Y_{TR}/L	0.0097	9.99	15.68	18.59	28.90	71.10	37.18
Y_{TD}/L	1.8960	0.05	0.08	0.10	28.20	71.80	0.19
ψ_{AD}	89.99	0.02	0.07	0.08	8.31	91.69	0.15
ψ_{TD}	179.81	0.01	0.02	0.03	19.10	80.90	0.05
u/U	0.63	25.09	28.34	37.85	43.94	56.06	75.70
v/U	-0.14	-9.95	-25.12	-27.02	13.55	86.45	-54.04
AD/L	2.3793	0.13	0.20	0.24	29.26	70.74	0.47
TR/L	1.2808	0.23	0.32	0.40	33.32	66.68	0.79
TD/L	3.1671	0.09	0.24	0.26	12.78	87.22	0.52

Table 4.8: Calm water turning circle uncertainties (δ=-35)

r	Mean	b_r %r	s_r %r	u_r %r	b_r^2 %u_r^2	s_r^2 %u_r^2	$U_{95,r}$ %r
X_{AD}/L	7.5464	0.01	0.08	0.08	2.57	97.43	0.16
X_{TD}/L	6.2036	0.02	0.95	0.95	0.03	99.97	1.90
Y_{TR}/L	-0.0250	-3.90	-17.11	-17.55	4.93	95.07	-35.09
Y_{TD}/L	-1.9246	-0.05	-0.27	-0.27	3.40	96.60	-0.55
ψ_{AD}	-90.02	-0.02	-0.10	-0.10	4.97	95.03	-0.20
ψ_{TD}	-177.28	-0.01	-1.19	-1.19	0.01	99.99	-2.38
u/U	0.64	23.36	27.49	36.07	41.93	58.07	72.14
v/U	0.14	21.95	26.95	34.76	39.88	60.12	69.51
AD/L	2.3709	0.13	0.24	0.27	22.52	77.48	0.54
TR/L	1.2955	0.23	0.23	0.32	49.88	50.12	0.64
TD/L	3.1850	0.09	0.21	0.23	15.79	84.21	0.46

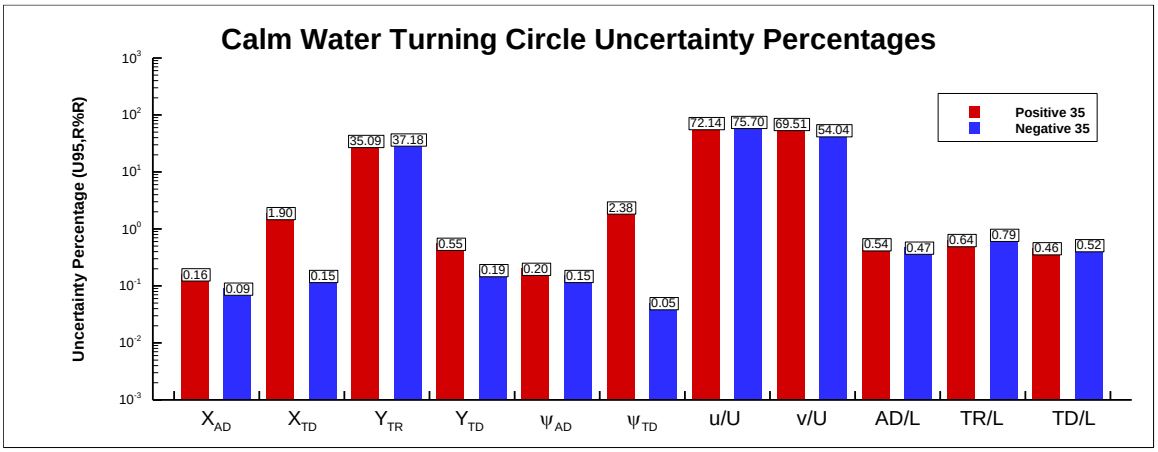

Figure 4.7: Uncertainty during calm water turning circles

During the turning maneuvers in calm water, large standard deviations during the times when the carriage stops and reverses its speed. This direction change occurs when the model heading is at approximately ±90 degrees. When this speed change occurs the carriage shakes causing unpredictable motions which results in different ship speeds reported during each test. This larger standard deviation is recorded and describe the repeatability error during each turning circle maneuver. The fluctuations can be observed in figure 4.8, the peaks approximately correspond to when the carriage is fully stopped and transitioning from either a positive velocity to a negative one or vice versa. During the time that the carriage is not reversing direction the standard deviations of the ship speed drop to approximately 0.006 m/s as the highest which is a comparable amount of change as seen in the course keeping test where the model operates closer to steady state.

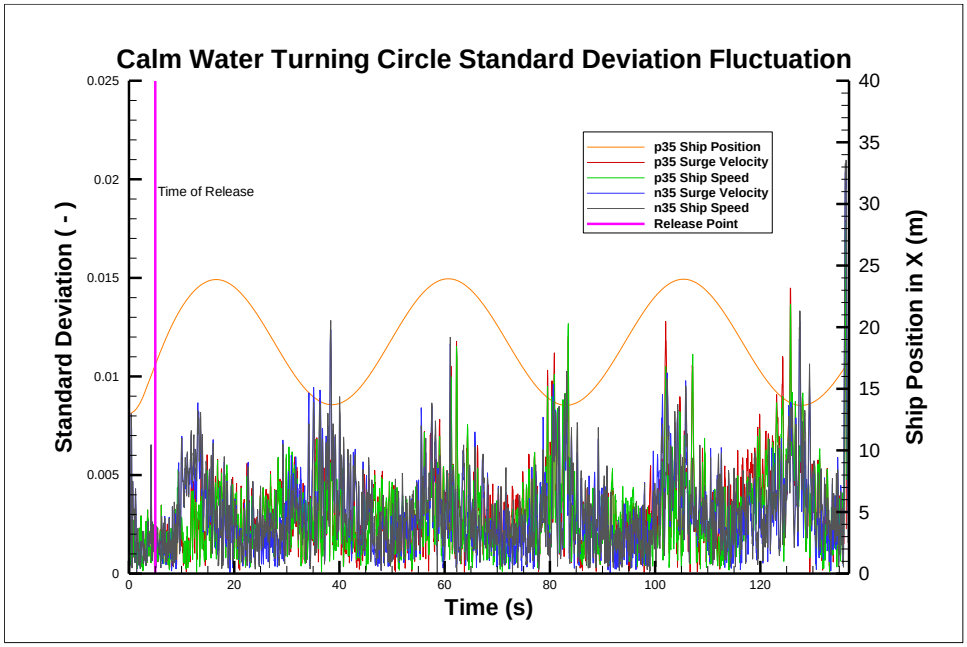

Figure 4.8: Standard deviation fluctuation during calm water turning circle maneuver

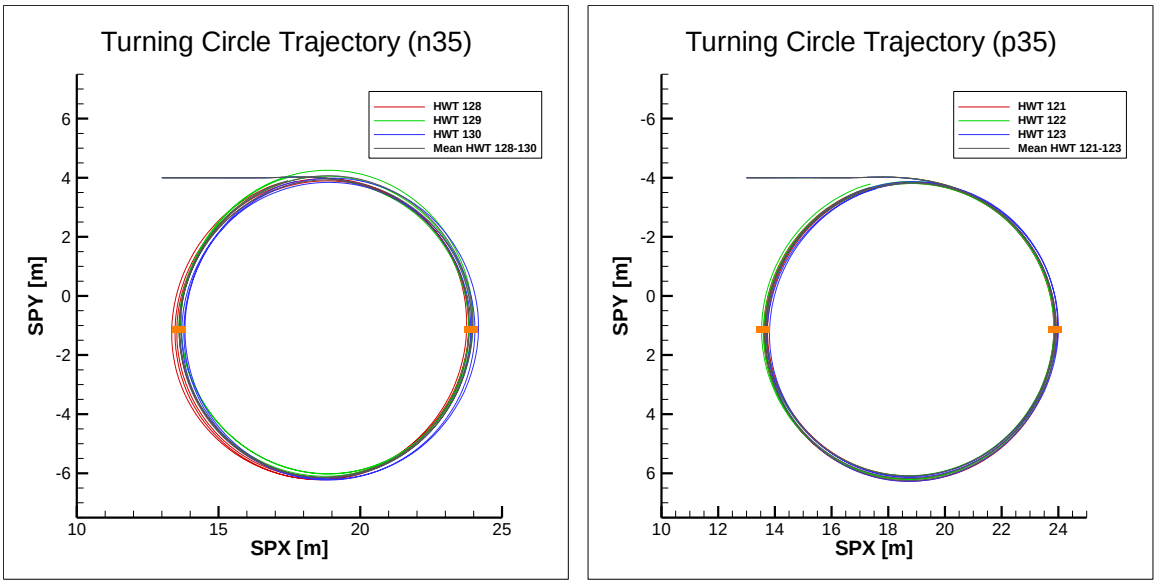

Figure 4.9: Turning circle trajectories with orange marks representing areas with high standard deviations seen in Figure 4.8

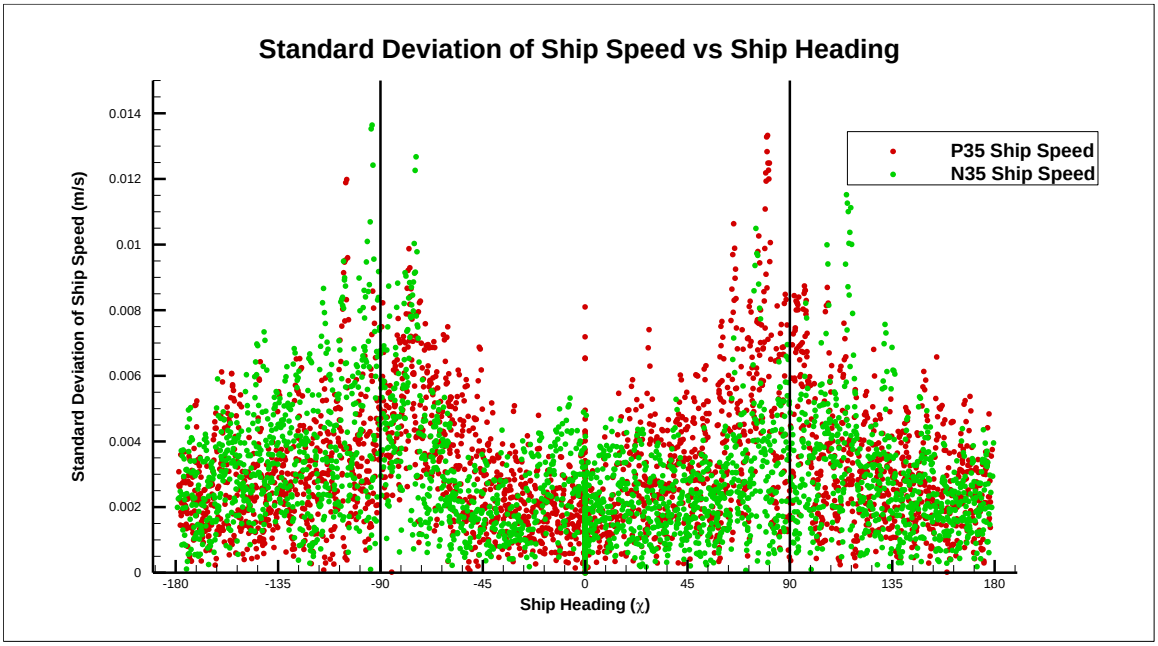

Figure 4.10: Ship speed standard deviation compared to ship heading

4.4 Comparison to Other Facilities

Once the uncertainties for the overshoot angles, advance, transfer, and tactical diameter were calculated, these values were compared to previously acquired data (Miyazaki, 2011). In this trial only the repeatability error was accounted for and the systematic standard uncertainty was not found. In Tables 4.9 and 4.10 the uncertainties are first compared with only the random certainty to display that the two trials have similar levels of repeatability error and the combined uncertainty is compared to the repeatability from the National Maritime Research Institute (NMRI). In both tests the models are twin skeg with dual rudders. When observing the repeatability error between the two facilities the results from IIHR have a lower amount of scatter which is observed by the lower standard deviation. The combined uncertainty at IIHR is found to be comparable to the repeatability error found at NMRI. This observation suggests that the systematic uncertainty plays only a small role, less than 1% of the measured mean value, in the overall uncertainty of the end result measurements that were compared. The systematic uncertainties for 10°/10° zigzag and -35° turning circle are first compared below followed by the calculated combined uncertainty compared to the systematic uncertainties from NMRI.

Table 4.9: Comparison to NMRI (Repeatability Errors Only)

	NMRI (Podded Propulsion Ship)				IIHR WB (ONRT)			
	$\bar{r}$	s_r	$s_{\bar{r}}$	$\frac{s_{\bar{r}}}{\bar{r}}\%$	$\bar{r}$	s_r	$s_{\bar{r}}$	$\frac{s_{\bar{r}}}{\bar{r}}\%$
Advance (AD/L)	2.869	0.032	0.010	0.349	2.371	0.010	0.006	0.237
Transfer (TR/L)	1.129	0.017	0.005	0.443	1.295	0.005	0.003	0.227
Tactical Diameter (TD/L)	1.351	0.014	0.004	0.296	3.185	0.012	0.007	0.212
Turning Radius (R/L)	0.542	0.013	0.004	0.738	1.624	0.004	0.002	0.113
1st Overshoot angle [deg]	7.150	0.433	0.125	1.748	2.313	0.080	0.046	2.008
2nd Overshoot angle [deg]	12.980	0.510	0.147	1.133	-2.065	0.030	0.017	0.847

Table 4.10: Comparison to NMRI (Total Uncertainty)

	NMRI (Podded Propulsion Ship)				IIHR WB (ONRT)				
	$\bar{r}$	s_r	$s_{\bar{r}}$	$\frac{s_{\bar{r}}}{\bar{r}}\%$	$\bar{r}$	$s_{\bar{r}}$	$b_{\bar{r}}$	$u_{\bar{r}}$	$\frac{u_{\bar{r}}}{r}\%$
Advance (AD/L)	2.869	0.032	0.010	0.349	2.371	0.006	0.003	0.006	0.539
Transfer (TR/L)	1.129	0.017	0.005	0.443	1.295	0.003	0.003	0.004	0.641
Tactical Diameter (TD/L)	1.351	0.014	0.004	0.296	3.185	0.007	0.003	0.007	0.463
Turning Radius (R/L)	0.542	0.013	0.004	0.738	1.624	0.002	0.001	0.003	0.170
1st Overshoot angle [deg]	7.150	0.433	0.125	1.748	2.313	0.046	0.003	0.047	4.02
2nd Overshoot angle [deg]	12.980	0.510	0.147	1.133	-2.065	0.017	0.003	0.018	-1.72

In addition to the data from NMRI, the data previously discussed taken by MARIN is also compared to the uncertainty results that were found. MARIN's data accounts for the sensitivity coefficients based on deviations from the initial settings to determine a propagation instead of the analytical approach analyzed. Additionally the repeatability and measurement uncertainty are also included. The 10°/10° zigzag and -35° turning circle are also compared for this study, finding the expanded uncertainties as percentages of the mean. The reported uncertainties from the MARIN tests were drastically higher during both their port and starboard side turning circles as well as similar results from their zigzag

maneuvers. These large differences are a result of their propagation contributing a much larger effect based on the ships response to the initial offset. The differences in mean values and uncertainties for the MARIN model are due to the single rudder and single screw propeller causing a lack of symmetry between sides (Quadvlieg, 2011).

Table 4.11: Comparison to MARIN maneuvering uncertainties

	MARIN KVLCC2 Port Side			MARIN KVLCC2 Starboard Side			IIHR WB (ONRT)		
	$\bar{r}$	$U_{95,r}$	$U_{95,r}$ %r	$\bar{r}$	$U_{95,r}$	$U_{95,r}$ %r	$\bar{r}$	$U_{95,r}$	$U_{95,r}$ %r
Advance (AD/L)	2.97	0.11	3.70	3.07	0.07	2.28	2.37	0.02	0.54
Tactical Diameter (TD/L)	3.09	0.12	3.88	3.28	0.08	2.44	3.19	0.02	0.64
Turning Radius (R/L)	1.23	0.09	6.91	1.25	0.06	4.40	1.62	0.01	0.46
1st Overshoot angle $(\alpha 10_1)$ [deg]	9.30	1.60	17.20	7.50	1.40	18.67	2.31	0.13	4.02
2nd Overshoot angle $(\alpha 10_2)$ [deg]	14.70	1.60	10.88	20.60	1.30	6.31	-2.06	0.05	-1.72

CHAPTER 5: RESULTS AND DISCUSSIONS FOR WAVE CONDITIONS

5.1 Course Keeping in Waves

The overall uncertainties for course keeping in wave conditions are found based on the process identified in Chapter 3. The 0^{th}, 1^{st}, and 2^{nd} harmonic amplitudes are analyzed along with the 1^{st} and 2^{nd} harmonic phases. The harmonics are analyzed based on the wave encounter frequencies that are dependent on the ship heading, speed, wavelength, and wave amplitude. For each test case the contribution of each systematic source of uncertainty in relation to the systematic standard is reported as well as the systematic, random, and combined uncertainty as a percentage of the measured value, and the percentage of the combined uncertainty that the systematic and random uncertainty make up are also reported. The measured values that are analyzed can be seen in Table 5.1. The waves that are produced have a wavelength to ship length ratio of 1.0 and a wave height to wavelength ratio of 0.02. The initial speed during each trial run caused a resulting Froude Number of 0.20 with the corresponding velocity of 1.11 m/s.

Table 5.1: Validation variables

$\zeta(t)/A$	Wave Elevation
$X(t)/L$	X-Position
$Y(t)/L$	Y-Position
$z(t)/A$	Heave
$\phi(t)/Ak$	Roll
$\theta(t)/Ak$	Pitch
$\psi(t)/Ak$	Yaw
$u(t)/U$	Surge Velocity
$v(t)/U$	Sway Velocity
U/U_0	Ship Speed

5.1.1 Wave Elevation

The wave elevation is measured near the bow of the ship model by an ultrasonic wave gauge. Only the 1st harmonic amplitude and phase are analyzed due to the sinusoidal nature of the wave generated by the wave makers in regular wave cases. The measured 1st harmonic amplitude and phase are non-dimensionalized by dividing by the desired wave amplitude.

$$\frac{\zeta(t)}{A} \tag{5.1}$$

The sensitivity coefficients are found for both the wave elevation and the desired wave amplitude. Similar to other tests the desired wave amplitude does not have an associated uncertainty because it is the desired setting not the actual measured wave amplitude.

$$\theta_{\zeta,\zeta/A} = \frac{\partial(\zeta / A)}{\partial \zeta} = \frac{1}{A} \tag{5.2}$$

$$\theta_{A,\zeta/A} = \frac{\partial(\zeta / A)}{\partial A} = -\frac{\zeta}{A^2} \tag{5.3}$$

The systematic standard uncertainty for wave elevation is found:

$$b_{\zeta/A}^2 = b_\zeta^2 \theta_{\zeta,\zeta/A}^2 + b_A^2 \theta_{A,\zeta/A}^2 \tag{5.4}$$

The measured wave amplitudes during tests is very consistent throughout all tests examined. The 1st harmonic amplitudes and phases found display very consistent results and almost no variance within phase. The maximum uncertainty found for wave elevation occurred when the wave heading of -135 degrees was examined with a value of 2.92% of the measured elevation. The expected wave elevation divided by amplitude was simulated as 1.00 in CFD trials, but slight deviation occurs within actual experiments. The phase were measured as very near to zero as expected. The low uncertainty and low random error relate very well to the sinusoidal shape of the waves produced from the wavemakers and encountered by the ship model during tests.

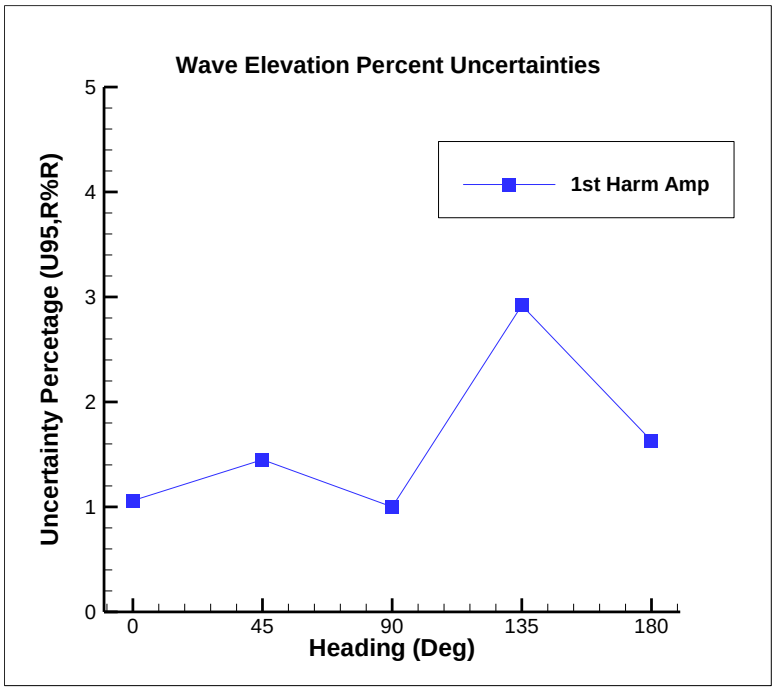

Figure 5.1: Uncertainties for wave elevation with different headings

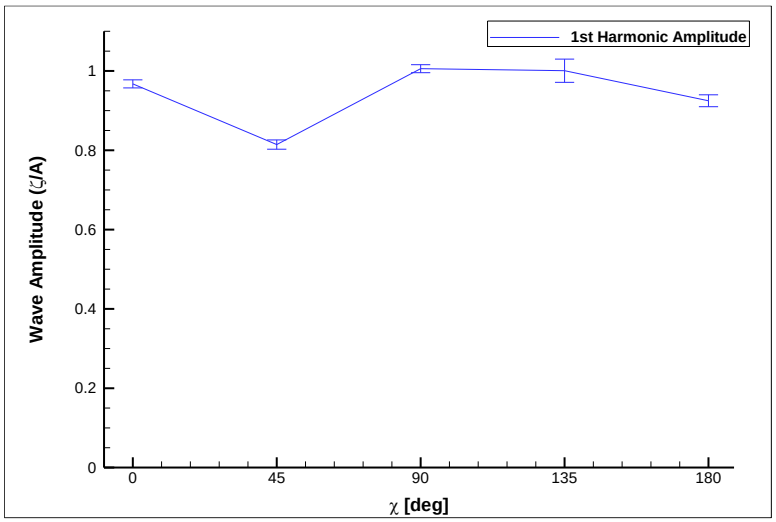

Figure 5.2: Wave elevation harmonic amplitude with error bars

Table 5.2: 1st Harmonic amplitude uncertainty calculations for wave elevation

Test Case		Heading ψ_c	# of runs (M)	$\overline{\zeta / A}$	$\theta_\zeta^2 \cdot b_\zeta^2$ $\%b_{\zeta/A}^2$	$\theta_A^2 \cdot b_A^2$ $\%b_{\zeta/A}^2$	$b_{\zeta/A}$ $\%\overline{\zeta / A}$	$s_{\overline{\zeta/A}}$ $\%\overline{\zeta / A}$	$u_{\overline{\zeta/A}}$ $\%\overline{\zeta / A}$	$b_{\zeta/A}^2$ $\%u_{\zeta/A}^2$	$s_{\overline{\zeta/A}}^2$ $\%u_{\zeta/A}^2$	$U_{95,\zeta/A}$ $\%\overline{\zeta / A}$
1st Amp	Case 3.12	0	3	0.9675	100.00	0.00	0.49	0.19	0.53	86.82	13.18	1.06
	Case 3.13	-45	3	0.8248	100.00	0.00	0.58	0.41	0.71	66.98	33.02	1.41
		-90	3	1.0058	100.00	0.00	0.47	0.17	0.50	89.11	10.89	1.00
		-135	3	0.9933	100.00	0.00	0.48	1.40	1.48	10.46	89.54	2.97
		-180	3	0.9248	100.00	0.00	0.52	0.63	0.81	40.13	59.87	1.63

Table 5.3: 1st Harmonic phase uncertainty calculations for wave elevation

Test Case		Heading ψ_c	# of runs (M)	$\overline{\zeta / A}$	$\theta_\zeta^2 \cdot b_\zeta^2$ $\%b_{\zeta/A}^2$	$\theta_A^2 \cdot b_A^2$ $\%b_{\zeta/A}^2$	$b_{\zeta/A}$ $\%2\pi$	$s_{\overline{\zeta/A}}$ $\%2\pi$	$u_{\overline{\zeta/A}}$ $\%2\pi$	$b_{\zeta/A}^2$ $\%u_{\zeta/A}^2$	$s_{\overline{\zeta/A}}^2$ $\%u_{\zeta/A}^2$	$U_{95,\overline{\zeta/A}}$ $\%2\pi$
1st Phase	Case 3.12	0	3	-0.0012	100.00	0.00	0.08	0.00	0.08	99.92	0.08	0.15
	Case 3.13	-45	3	0.0022	100.00	0.00	0.08	0.00	0.08	99.85	0.15	0.15
		-90	3	-0.0006	100.00	0.00	0.08	0.00	0.08	99.99	0.01	0.15
		-135	3	0.0026	100.00	0.00	0.08	0.00	0.08	99.90	0.10	0.15
		-180	3	-0.0016	100.00	0.00	0.08	0.00	0.08	99.98	0.02	0.15

5.1.2 X-position

To calculate the X-position uncertainties the 0^{th}, 1^{st}, and 2^{nd} harmonic amplitudes and phases are analyzed based on the process described in Section 4.2.1. The reported uncertainties for X–position are consistently small for both the 0^{th} and 1^{st} harmonic amplitudes. The majority of the uncertainty for the 0^{th} harmonic amplitude is made up of random error between measurements. When analyzing the 1^{st} harmonic amplitude, changes occur with whether systematic or random uncertainty contributes a larger percentage to the combined uncertainty depending on the heading of the model. The carriage position was the largest contributor for systematic uncertainty when observing the X-position. This is a combination of the accuracy of the wheel encoder and the potential slipping that occurs across the rails.

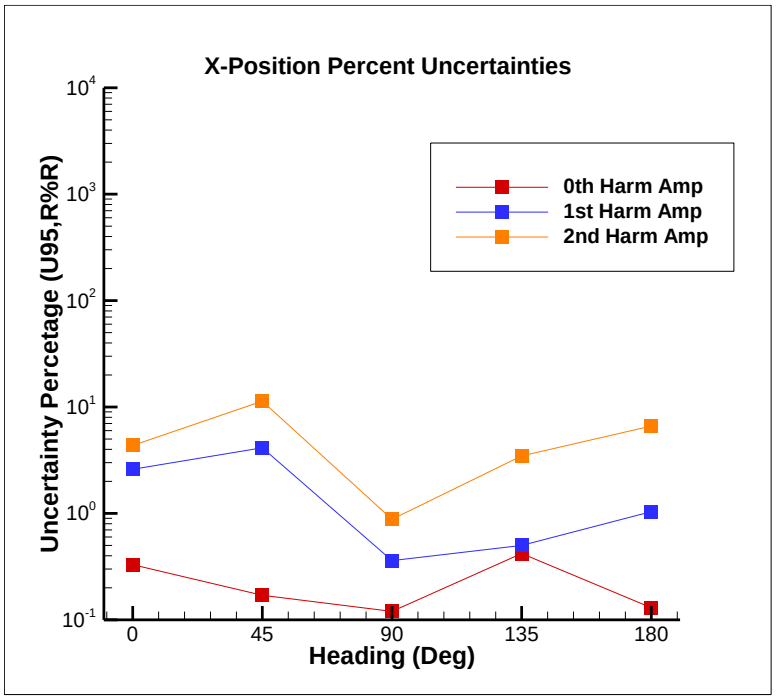

Figure 5.3: Uncertainties for X-Position with different headings

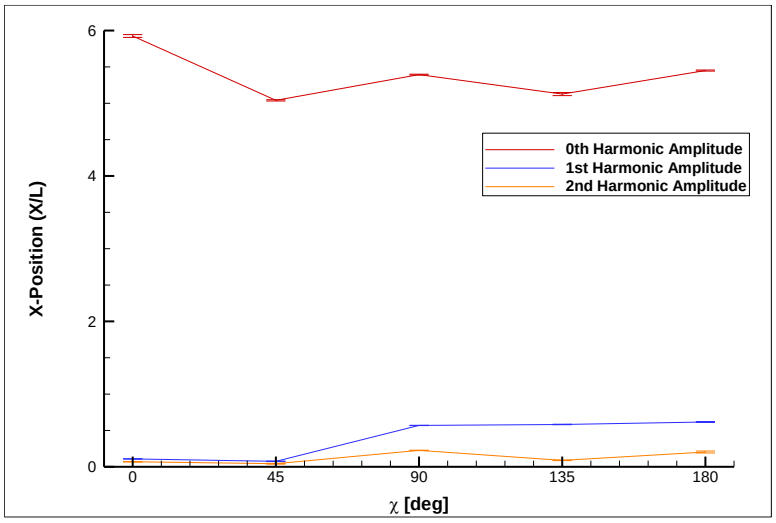

Figure 5.4: X- Position harmonic amplitudes with error bars

Table 5.4: Harmonic amplitude uncertainties for X-positions

Test Case		Heading ψ_c	# of runs (M)	$\overline{X/L}$	$\theta^2_{CPX}\cdot b^2_{CPX}$ $\%b^2_{X/L}$	$\theta^2_{DPX}\cdot b^2_{DPX}$ $\%b^2_{X/L}$	$\theta^2_{DPY}\cdot b^2_{DPY}$ $\%b^2_{X/L}$	$\theta^2_{CPT}\cdot b^2_{CPT}$ $\%b^2_{X/L}$	$\theta^2_{L}\cdot b^2_{L}$ $\%b^2_{X/L}$	$b_{X/L}$ $\%\overline{X/L}$	$s_{\overline{X/L}}$ $\%\overline{X/L}$	$u_{X/L}$ $\%\overline{X/L}$	$b^2_{X/L}$ $\%u^2_{X/L}$	$s^2_{\overline{X/L}}$ $\%u^2_{X/L}$	$U_{95,X/L}$ $\%\overline{X/L}$
0th Amp	Case 3.12	0	3	5.9254	86.55	10.86	0.35	1.03	1.22	0.02	0.17	0.17	0.99	99.01	0.33
	Case 3.13	-45	3	5.0406	81.51	6.95	1.79	8.92	0.83	0.02	0.08	0.09	5.33	94.67	0.17
		-90	3	5.3943	88.27	9.50	1.06	0.14	1.03	0.02	0.06	0.06	9.41	90.59	0.12
		-135	3	5.1271	87.58	10.34	0.65	0.52	0.92	0.02	0.21	0.21	0.83	99.17	0.42
		-180	3	5.4504	86.29	11.09	0.23	1.36	1.03	0.02	0.06	0.07	7.50	92.50	0.13
1st Amp	Case 3.12	0	3	0.1090	85.44	11.49	0.00	3.06	0.00	0.91	0.93	1.30	48.98	51.02	2.60
	Case 3.13	-45	3	0.0759	89.24	9.53	1.11	0.13	0.00	1.28	1.63	2.07	38.17	61.83	4.14
		-90	3	0.5693	86.63	11.39	0.12	1.84	0.01	0.17	0.04	0.18	94.17	5.83	0.36
		-135	3	0.5826	84.54	1.12	4.58	9.74	0.01	0.17	0.18	0.25	46.76	53.24	0.50
		-180	3	0.6162	85.50	11.50	0.00	2.98	0.01	0.16	0.49	0.52	9.65	90.35	1.04
2nd Amp	Case 3.12	0	3	0.0695	85.39	11.49	0.00	3.12	0.00	1.43	1.64	2.17	43.17	56.83	4.35
	Case 3.13	-45	3	0.0427	85.63	11.51	0.01	2.85	0.00	2.32	5.18	5.68	16.74	83.26	11.35
		-90	3	0.2261	85.54	11.50	0.00	2.95	0.00	0.44	0.05	0.44	98.64	1.36	0.88
		-135	3	0.0887	86.59	11.41	0.11	1.89	0.00	1.11	1.33	1.74	41.02	58.98	3.47
		-180	3	0.2035	85.55	11.50	0.00	2.94	0.00	0.49	3.28	3.31	2.16	97.84	6.63

Table 5.5: Harmonic phase uncertainties for X-position

Test Case		Heading ψ_c	# of runs (M)	$\overline{X/L}$	$\theta_{CPX}^2 \cdot b_{CPX}^2$ $\%b_{X/L}^2$	$\theta_{DPX}^2 \cdot b_{DPX}^2$ $\%b_{X/L}^2$	$\theta_{DPY}^2 \cdot b_{DPY}^2$ $\%b_{X/L}^2$	$\theta_{CPT}^2 \cdot b_{CPT}^2$ $\%b_{X/L}^2$	$\theta_L^2 \cdot b_L^2$ $\%b_{X/L}^2$	$b_{X/L}$ $\%2\pi$	$s_{\overline{X/L}}$ $\%2\pi$	$u_{X/L}$ $\%2\pi$	$b_{X/L}^2$ $\%u_{X/L}^2$	$s_{\overline{X/L}}^2$ $\%u_{X/L}^2$	$U_{95,X/L}$ $\%2\pi$
1st Phase	Case 3.12	0	3	-2.2569	88.37	10.44	0.65	0.53	0.02	0.02	1.29	1.29	0.01	99.99	2.58
	Case 3.13	-45	3	-2.2663	82.93	3.34	3.49	10.22	0.02	0.02	2.83	2.83	0.00	100.00	5.66
		-90	3	-3.0396	90.66	3.50	3.88	1.91	0.03	0.02	0.01	0.02	81.30	18.70	0.03
		-135	3	2.7006	83.50	2.31	3.99	10.18	0.02	0.02	3.09	3.09	0.00	100.00	6.17
		-180	3	2.3497	84.01	1.66	4.31	10.01	0.02	0.02	1.41	1.41	0.01	99.99	2.82
2nd Phase	Case 3.12	0	3	0.0124	87.59	0.02	5.25	7.14	0.00	0.02	2.33	2.33	0.00	100.00	4.67
	Case 3.13	-45	3	0.1875	90.78	4.09	3.63	1.50	0.00	0.02	5.23	5.23	0.00	100.00	10.46
		-90	3	-2.9771	87.36	11.11	0.29	1.21	0.03	0.02	0.00	0.02	91.94	8.06	0.03
		-135	3	0.6061	90.63	3.22	4.01	2.13	0.00	0.02	3.60	3.60	0.00	100.00	7.20
		-180	3	0.4324	83.13	2.97	3.67	10.24	0.00	0.02	2.19	2.19	0.01	99.99	4.37

5.1.3 Y-position

Similarly to X-position, the process described for zig zag maneuvers is analyzed for the 0^{th}, 1^{st}, and 2^{nd} harmonic amplitudes and phases described in Section 4.2.2. When observing the Y-position larger uncertainties are reported for the head and following waves due to the Y-position being less affected by the wave encounter when the model is not encountering the wave at an angle. The smallest percentages of uncertainties were observed with quartering and beam waves due to the larger amount of Y-position changes with the wave encounters. Similarly to the X-position the Y-position systematic uncertainty is primarily due to the reported carriage position.

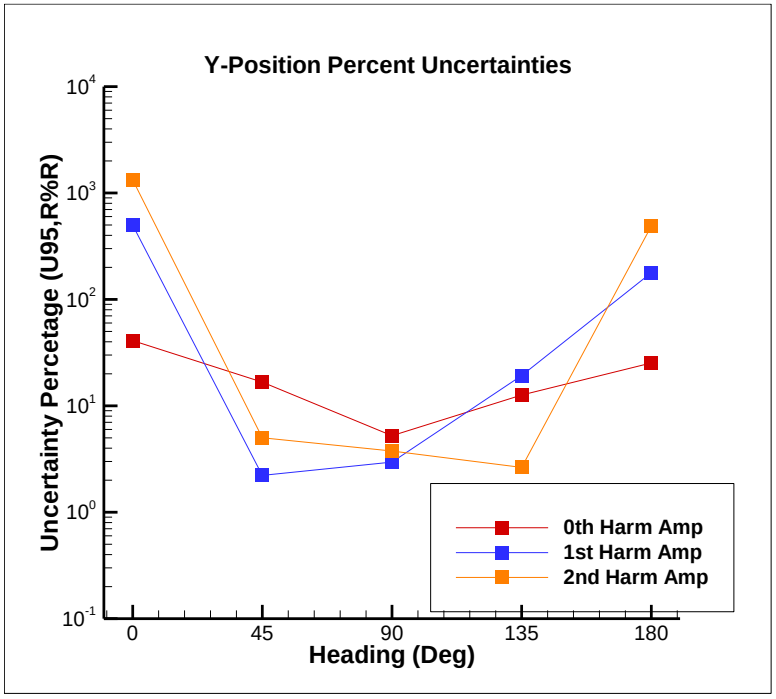

Figure 5.5: Uncertainties for Y-Position with different headings

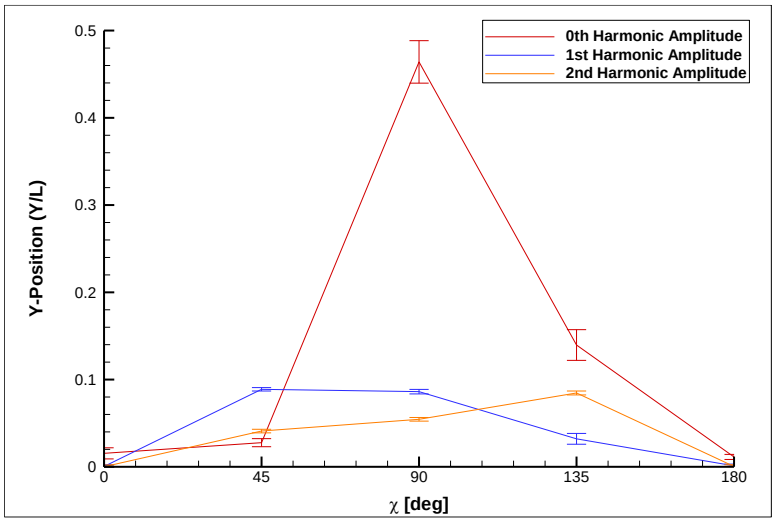

Figure 5.6: Y-Position harmonic amplitudes with error bars

Table 5.6: Harmonic amplitude uncertainties for Y-position

Test Case		Heading ψ_c	# of runs (M)	$\overline{Y/L}$	$\theta^2_{CPY}\cdot b^2_{CPY}$ $\%b^2_{Y/L}$	$\theta^2_{DPX}\cdot b^2_{DPX}$ $\%b^2_{Y/L}$	$\theta^2_{DPY}\cdot b^2_{DPY}$ $\%b^2_{Y/L}$	$\theta^2_{CPT}\cdot b^2_{CPT}$ $\%b^2_{Y/L}$	$\theta^2_{L}\cdot b^2_{L}$ $\%b^2_{Y/L}$	$b_{Y/L}$ $\%\overline{Y/L}$	$s_{\overline{Y/L}}$ $\%\overline{Y/L}$	$u_{Y/L}$ $\%\overline{Y/L}$	$b^2_{Y/L}$ $\%u^2_{Y/L}$	$s^2_{\overline{Y/L}}$ $\%u^2_{Y/L}$	$U_{95,Y/L}$ $\%\overline{Y/L}$
0th Amp	Case 3.12	0	3	0.0154	88.19	4.94	0.80	4.83	1.24	6.33	19.50	20.50	9.52	90.48	41.01
	Case 3.13	-45	3	0.0277	81.95	3.12	4.04	10.05	0.83	3.66	7.51	8.35	19.21	80.79	16.70
		-90	3	0.4641	89.45	4.30	2.41	2.80	1.04	0.21	2.61	2.62	0.64	99.36	5.24
		-135	3	0.1396	89.04	4.69	1.47	3.86	0.94	0.70	6.28	6.31	1.22	98.78	12.63
		-180	3	0.0113	88.01	5.05	0.53	5.36	1.05	8.62	9.25	12.65	46.50	53.50	25.29
1st Amp	Case 3.12	0	3	0.0004	87.30	5.25	0.00	7.46	0.00	248.97	1.51	248.97	100.00	0.00	497.94
	Case 3.13	-45	3	0.0888	90.42	4.31	2.51	2.76	0.00	1.09	0.24	1.11	95.31	4.69	2.22
		-90	3	0.0862	88.46	5.20	0.27	6.07	0.01	1.13	0.96	1.48	58.33	41.67	2.96
		-135	3	0.0321	83.14	0.49	10.08	6.27	0.01	3.14	9.09	9.62	10.65	89.35	19.24
		-180	3	0.0011	87.36	5.25	0.00	7.38	0.01	87.99	14.18	89.13	97.47	2.53	178.26
2nd Amp	Case 3.12	0	3	0.0001	87.25	5.24	0.00	7.51	0.00	663.21	13.82	663.35	99.96	0.04	1326.7
	Case 3.13	-45	3	0.0410	87.49	5.25	0.01	7.24	0.00	2.39	0.74	2.50	91.31	8.69	5.01
		-90	3	0.0545	87.40	5.25	0.01	7.34	0.00	1.80	0.54	1.88	91.73	8.27	3.76
		-135	3	0.0846	88.42	5.20	0.25	6.13	0.00	1.15	0.64	1.32	76.40	23.60	2.64
		-180	3	0.0004	87.41	5.25	0.01	7.33	0.00	243.32	25.16	244.62	98.94	1.06	489.23

Table 5.7: Harmonic phase uncertainty for Y-position

Test Case		Heading ψ_c	# of runs (M)	$\overline{Y/L}$	$\theta_{CPY}^2 \cdot b_{CPY}^2$ $\%b_{Y/L}^2$	$\theta_{DPX}^2 \cdot b_{DPX}^2$ $\%b_{Y/L}^2$	$\theta_{DPY}^2 \cdot b_{DPY}^2$ $\%b_{Y/L}^2$	$\theta_{CPT}^2 \cdot b_{CPT}^2$ $\%b_{Y/L}^2$	$\theta_L^2 \cdot b_L^2$ $\%b_{Y/L}^2$	$b_{Y/L}$ $\%2\pi$	$s_{\overline{Y/L}}$ $\%2\pi$	$u_{Y/L}$ $\%2\pi$	$b_{Y/L}^2$ $\%u_{Y/L}^2$	$s_{\overline{Y/L}}^2$ $\%u_{Y/L}^2$	$U_{95,Y/L}$ $\%2\pi$
1st Phase	Case 3.12	0	3	1.8883	89.86	4.74	1.48	3.90	0.02	0.02	3.47	3.47	0.00	100.00	6.93
	Case 3.13	-45	3	1.1472	82.25	1.48	7.75	8.50	0.02	0.02	1.94	1.94	0.01	99.99	3.89
		-90	3	-0.8956	89.80	1.55	8.61	0.00	0.03	0.02	0.15	0.16	0.98	99.02	0.31
		-135	3	-1.1501	82.49	1.02	8.82	7.65	0.02	0.02	4.42	4.42	0.00	100.00	8.83
		-180	3	-1.2346	82.79	0.73	9.51	6.96	0.02	0.02	1.75	1.75	0.01	99.99	3.51
2nd Phase	Case 3.12	0	3	-0.5749	85.73	0.01	11.51	2.75	0.00	0.02	21.71	21.71	0.00	100.00	43.42
	Case 3.13	-45	3	-2.3897	90.11	1.81	8.06	0.02	0.00	0.02	3.83	3.83	0.00	100.00	7.67
		-90	3	1.3636	89.09	5.06	0.66	5.16	0.03	0.02	0.09	0.09	3.07	96.93	0.18
		-135	3	0.6616	89.68	1.42	8.88	0.02	0.00	0.02	6.45	6.45	0.00	100.00	12.91
		-180	3	-0.8385	82.33	1.31	8.14	8.22	0.00	0.02	4.45	4.45	0.00	100.00	8.89

5.1.4 Heave

Heave is defined as the change in the vertical location of the ship's z-center of gravity during testing. This motion is measured by the 6DOF-VMCS based on the change in perspective of the target board in relation to the camera mounted at the center of the sub-carriage. The measured is non-dimensionalized by dividing by the desired wave amplitude.

$$\frac{z(t)}{A} \tag{5.5}$$

The sensitivity coefficients are found as the partial derivatives with respect to heave and wave amplitude.

$$\theta_{z,z/A} = \frac{\partial(z/A)}{\partial(z)} = \frac{1}{A} \tag{5.6}$$

$$\theta_{A,z/A} = \frac{\partial(z/A)}{\partial(A)} = -\frac{z}{A^2} \tag{5.7}$$

The systematic standard uncertainty of the heave is found based on the individual standard uncertainties of the heave and desired wave amplitude. Since the wave amplitude is based on the desired value, it is an exact value and there is zero uncertainty involved in this measurement $(b_A = 0)$.

$$b_{z/A}^2 = b_z^2\theta_{z,z/A}^2 + b_A^2\theta_{A,z/A}^2 \tag{5.8}$$

When analyzed, the heave displayed relatively large uncertainties when observing the 0th harmonic amplitude. This is due to the average heave being near zero when encountering the waves, as a result the 1st harmonic amplitude better describes the true heave uncertainty. The uncertainty percentages reported are below 3% for all headings except for the following wave case. This appears to be due to the lower reported 1st harmonic amplitude for this case where there was a lower amount of encounters with the waves. Additionally when analyzing the 1st harmonic phase the percent uncertainties are estimated as less than 5% of the maximum phase. The reported uncertainties from the heave were primarily from systematic sources due to the limited accuracy of the heave motion by the 6DOF-VMCS. With small heave changes being reported from the low amplitude waves the heave uncertainty was very dependent on the accuracy of the measurement.

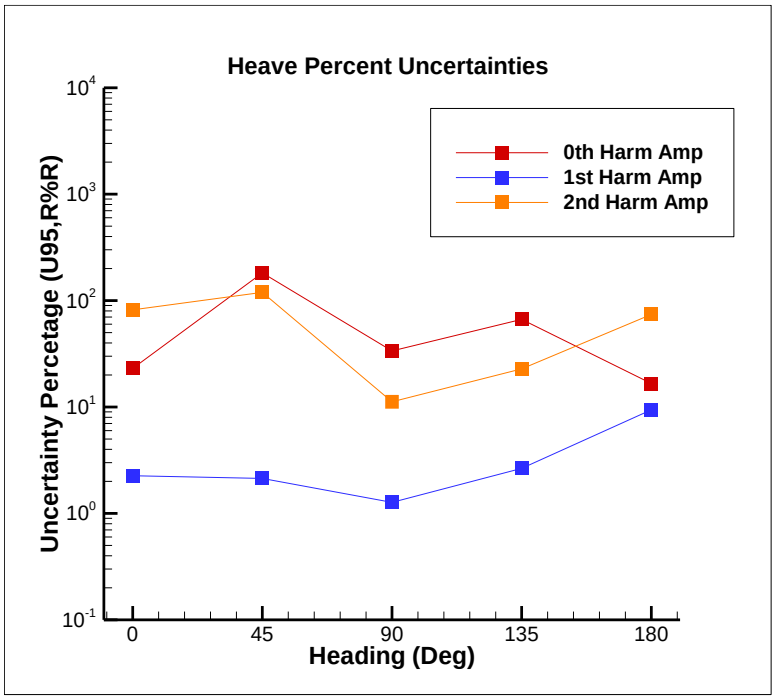

Figure 5.7: Uncertainties for heave with different headings

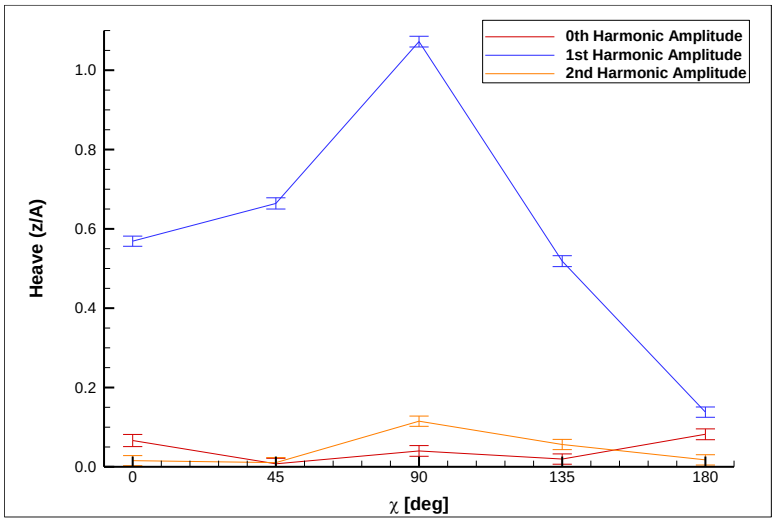

Figure 5.8: Heave harmonic amplitudes with error bars

Table 5.8: Harmonic amplitude uncertainties for heave

Test Case		Heading ψ_c	# of runs (M)	$\overline{z/A}$	$\theta_z^2 \cdot b_z^2$ $\%b_{z/A}^2$	$\theta_A^2 \cdot b_A^2$ $\%b_{z/A}^2$	$b_{z/A}$ $\%\overline{z/A}$	$s_{\overline{z/A}}$ $\%\overline{z/A}$	$u_{z/A}$ $\%\overline{z/A}$	$b_{z/A}^2$ $\%u_{z/A}^2$	$s_{\overline{z/A}}^2$ $\%u_{z/A}^2$	$U_{95,z/A}$ $\%\overline{z/A}$
0th Amp	Case 3.12	0	3	0.0663	100.00	0.00	9.59	6.41	11.53	69.11	30.89	23.07
	Case 3.13	-45	3	0.0076	100.00	0.00	83.68	35.75	91.00	84.56	15.44	182.00
		-90	3	0.0400	100.00	0.00	15.87	5.56	16.82	89.09	10.91	33.63
		-135	3	0.0195	100.00	0.00	32.52	7.23	33.31	95.29	4.71	66.63
		-180	3	0.0820	100.00	0.00	7.75	3.02	8.31	86.81	13.19	16.63
1st Amp	Case 3.12	0	3	0.5690	100.00	0.00	1.12	0.17	1.13	97.80	2.20	2.26
	Case 3.13	-45	3	0.6723	100.00	0.00	0.95	0.44	1.04	81.87	18.13	2.09
		-90	3	1.0722	100.00	0.00	0.59	0.22	0.63	87.82	12.18	1.27
		-135	3	0.5150	100.00	0.00	1.23	0.52	1.34	84.74	15.26	2.68
		-180	3	0.1379	100.00	0.00	4.61	0.94	4.71	95.97	4.03	9.41
2nd Amp	Case 3.12	0	3	0.0155	100.00	0.00	40.90	1.19	40.92	99.92	0.08	81.83
	Case 3.13	-45	3	0.0097	100.00	0.00	65.57	5.49	65.80	99.30	0.70	131.61
		-90	3	0.1150	100.00	0.00	5.52	0.87	5.59	97.58	2.42	11.19
		-135	3	0.0555	100.00	0.00	11.44	1.98	11.61	97.09	2.91	23.22
		-180	3	0.0175	100.00	0.00	36.30	7.44	37.05	95.97	4.03	74.10

Table 5.9: Harmonic phase uncertainties for heave

Test Case		Heading ψ_c	# of runs (M)	$\overline{z/A}$	$\theta_z^2 \cdot b_z^2$ $\%b_{z/A}^2$	$\theta_A^2 \cdot b_A^2$ $\%b_{z/A}^2$	$b_{z/A}$ $\%2\pi$	$s_{\overline{z/A}}$ $\%2\pi$	$u_{z/A}$ $\%2\pi$	$b_{z/A}^2$ $\%u_{z/A}^2$	$s_{\overline{z/A}}^2$ $\%u_{z/A}^2$	$U_{95,z/A}$ $\%2\pi$
1st Phase	Case 3.12	0	3	-1.0095	100.00	0.00	0.10	2.04	2.04	0.24	99.76	4.09
	Case 3.13	-45	3	2.6393	100.00	0.00	0.10	2.16	2.16	0.22	99.78	4.32
		-90	3	1.7080	100.00	0.00	0.10	0.29	0.31	10.81	89.19	0.62
		-135	3	1.6641	100.00	0.00	0.10	1.97	1.97	0.26	99.74	3.95
		-180	3	-1.4069	100.00	0.00	0.10	1.25	1.25	0.65	99.35	2.51
2nd Phase	Case 3.12	0	3	1.0421	100.00	0.00	0.10	4.40	4.40	0.05	99.95	8.80
	Case 3.13	-45	3	-1.3137	100.00	0.00	0.10	3.37	3.37	0.09	99.91	6.74
		-90	3	-1.5293	100.00	0.00	0.10	0.37	0.38	6.91	93.09	0.77
		-135	3	0.6138	100.00	0.00	0.10	5.56	5.56	0.03	99.97	11.13
		-180	3	2.6833	100.00	0.00	0.10	3.30	3.30	0.09	99.91	6.60

5.1.5 Roll Angle

The roll measurement represents the motion about the X-axis that travels longitudinally along the length of the ship model. This value is measured by the 6DOF-VMCS. The measured roll angle is non-dimensionalized by dividing by the wave number and amplitude. The wave number is represented by the variable k.

$$k = \frac{2\pi}{\lambda} \tag{5.9}$$

The wavelength (λ) is not directly measured in the experiments, but is calculated based on the frequency of the plunger motions and the effects of gravity. This relationship is applicable when deep water conditions are met ($h/\lambda > 0.5$, where h represents the depth of water in the basin).

$$\lambda = \frac{g}{2\pi f_p^2} \tag{5.10}$$

Substitution is used to combine the two above equations to obtain a representation for wave number that does not involve the wavelength.

$$\frac{\phi(t)}{Ak} = \frac{g\phi}{A(2\pi f_p)^2} \tag{5.11}$$

By finding the partial derivatives of the substituted representation of the non-dimensionalized roll angle, the sensitivity coefficients are found.

$$\theta_{\phi,\phi/Ak} = \frac{\partial(\phi/Ak)}{\partial(\phi)} = \frac{g}{A(2\pi f_p)^2} \tag{5.12}$$

$$\theta_{g,\phi/Ak} = \frac{\partial(\phi/Ak)}{\partial(g)} = \frac{\phi}{A(2\pi f_p)^2} \tag{5.13}$$

$$\theta_{A,\phi/Ak} = \frac{\partial(\phi/Ak)}{\partial(A)} = -\frac{g\phi}{A^2(2\pi f_p)^2} \tag{5.14}$$

$$\theta_{f_p,\phi/Ak} = \frac{\partial(\phi/Ak)}{\partial(f_p)} = -\frac{4\pi g\phi}{A(2\pi f_p)^3} \tag{5.15}$$

Within the systematic standard uncertainty both the gravitational constant and the desired wave amplitude are treated constants and do not have an uncertainty value associated with them.

$$b^2_{\phi/Ak} = b^2_\phi\theta^2_{\phi,\phi/Ak} + b^2_g\theta^2_{g,\phi/Ak} + b^2_A\theta^2_{A,\phi/Ak} + b^2_{f_p}\theta^2_{f_p,\phi/Ak} \tag{5.16}$$

Observing the 1st harmonic amplitude roll angles, the head and following waves reported very minor amounts of roll due to the encounter angle with the wave. This low amplitude results in drastically higher percentages reported. The quartering and beam waves reported more reasonable levels of uncertainties of under 4%.

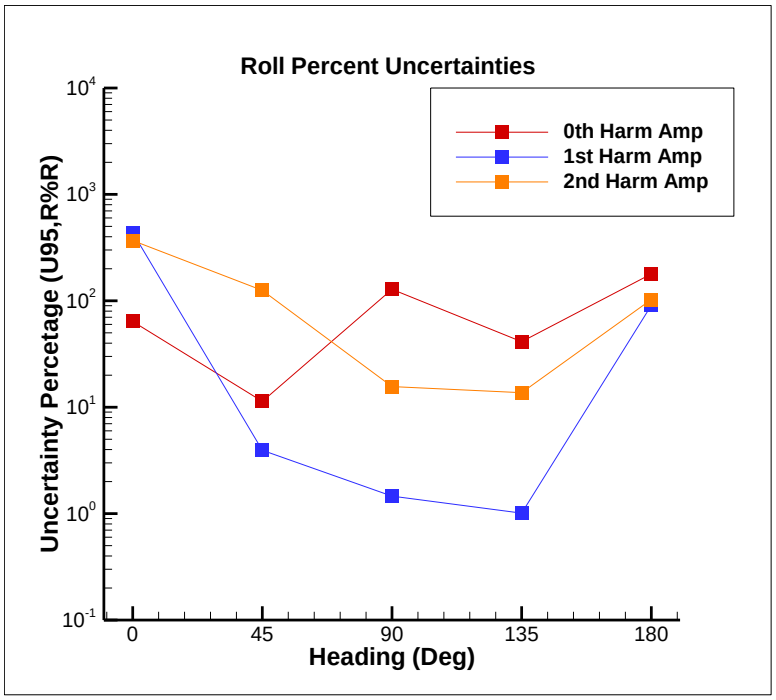

Figure 5.9: Uncertainties for roll angle with different headings

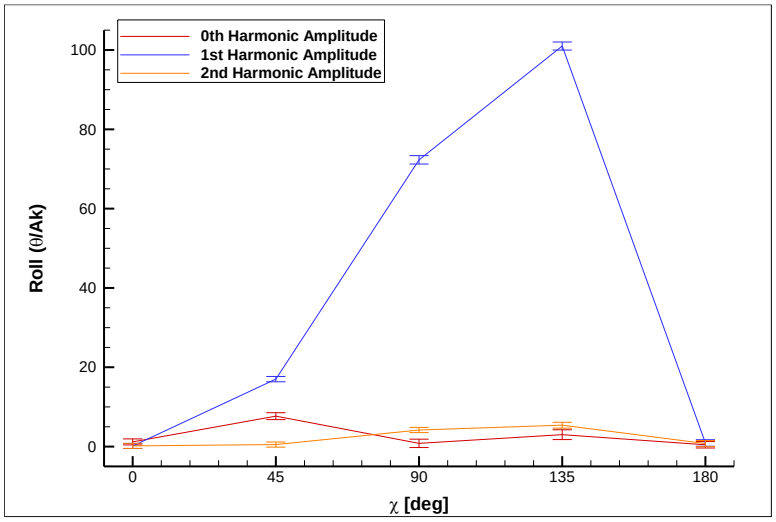

Figure 5.10: Roll angle harmonic amplitudes with error bars

Table 5.10: Harmonic amplitude uncertainties for roll

Test Case		Heading ψ_c	# of runs (M)	$\overline{\phi / Ak}$	$\theta_\phi^2 \cdot b_\phi^2$ $\%b_{\phi/Ak}^2$	$\theta_g^2 \cdot b_g^2$ $\%b_{\phi/Ak}^2$	$\theta_A^2 \cdot b_A^2$ $\%b_{\phi/Ak}^2$	$\theta_{f_p}^2 \cdot b_{f_p}^2$ $\%b_{\phi/Ak}^2$	$b_{\phi/Ak}$ $\%\overline{\phi / Ak}$	$s_{\overline{\phi/Ak}}$ $\%\overline{\phi / Ak}$	$u_{\phi/Ak}$ $\%\overline{\phi / Ak}$	$b_{\phi/Ak}^2$ $\%u_{\phi/Ak}^2$	$s_{\overline{\phi/Ak}}^2$ $\%u_{\phi/Ak}^2$	$U_{95,\phi/Ak}$ $\%\overline{\phi / Ak}$
0th Amp	Case 3.12	0	3	1.18	99.63	0.00	0.00	0.37	26.96	17.14	31.95	71.22	28.78	63.90
	Case 3.13	-45	3	7.68	86.47	0.00	0.00	13.53	4.46	3.51	5.67	61.73	38.27	11.35
		-90	3	0.82	99.82	0.00	0.00	0.18	38.90	50.98	64.13	36.80	63.20	128.26
		-135	3	3.01	97.66	0.00	0.00	2.34	10.72	17.65	20.65	26.94	73.06	41.30
		-180	3	0.46	99.94	0.00	0.00	0.06	69.55	56.29	89.48	60.42	39.58	178.96
1st Amp	Case 3.12	0	3	0.15	100.00	0.00	0.00	0.00	215.98	33.84	218.62	97.60	2.40	437.24
	Case 3.13	-45	3	17.20	98.39	0.00	0.00	1.61	1.87	0.55	1.94	92.07	7.93	3.89
		-90	3	72.30	77.58	0.00	0.00	22.42	0.50	0.53	0.73	46.67	53.33	1.46
		-135	3	100.37	64.23	0.00	0.00	35.77	0.40	0.33	0.52	58.68	41.32	1.03
		-180	3	0.91	100.00	0.00	0.00	0.00	34.82	28.92	45.26	59.17	40.83	90.53
2nd Amp	Case 3.12	0	3	0.17	100.00	0.00	0.00	0.00	184.01	7.74	184.17	99.82	0.18	368.34
	Case 3.13	-45	3	0.51	100.00	0.00	0.00	0.00	62.29	4.89	62.48	99.39	0.61	124.96
		-90	3	4.19	99.90	0.00	0.00	0.10	7.61	1.77	7.81	94.85	5.15	15.63
		-135	3	5.19	99.85	0.00	0.00	0.15	6.14	4.26	7.47	67.44	32.56	14.95
		-180	3	0.76	100.00	0.00	0.00	0.00	41.92	29.55	51.29	66.81	33.19	102.57

Table 5.11: Harmonic phase uncertainties for roll

Test Case		Heading ψ_c	# of runs (M)	$\overline{\phi/Ak}$	$\theta_\phi^2 \cdot b_\phi^2$ $\%b_{\phi/Ak}^2$	$\theta_g^2 \cdot b_g^2$ $\%b_{\phi/Ak}^2$	$\theta_A^2 \cdot b_A^2$ $\%b_{\phi/Ak}^2$	$\theta_{f_p}^2 \cdot b_{f_p}^2$ $\%b_{\phi/Ak}^2$	$b_{\phi/Ak}$ $\%2\pi$	$s_{\overline{\phi/Ak}}$ $\%2\pi$	$u_{\phi/Ak}$ $\%2\pi$	$b_{\phi/Ak}^2$ $\%u_{\phi/Ak}^2$	$s_{\overline{\phi/Ak}}^2$ $\%u_{\phi/Ak}^2$	$U_{95,\phi/Ak}$ $\%2\pi$
1st Phase	Case 3.12	0	3	0.09	99.99	0.00	0.00	0.01	5.07	17.44	18.17	7.78	92.22	36.33
	Case 3.13	-45	3	0.49	99.66	0.00	0.00	0.34	5.07	2.23	5.54	83.76	16.24	11.09
		-90	3	0.96	98.73	0.00	0.00	1.27	5.10	0.30	5.11	99.66	0.34	10.21
		-135	3	2.36	92.76	0.00	0.00	7.24	5.26	2.03	5.64	86.98	13.02	11.28
		-180	3	1.15	98.17	0.00	0.00	1.83	5.11	2.02	5.50	86.55	13.45	10.99
2nd Phase	Case 3.12	0	3	-1.20	98.03	0.00	0.00	1.97	5.12	3.45	6.17	68.79	31.21	12.34
	Case 3.13	-45	3	-0.48	99.68	0.00	0.00	0.32	5.07	28.55	29.00	3.06	96.94	57.99
		-90	3	-1.84	95.49	0.00	0.00	4.51	5.18	0.33	5.19	99.59	0.41	10.39
		-135	3	-2.05	94.46	0.00	0.00	5.54	5.21	4.32	6.77	59.27	40.73	13.54
		-180	3	3.08	88.28	0.00	0.00	11.72	5.39	0.55	5.42	98.98	1.02	10.84

5.1.6 Pitch Angle

The pitch angle is found and non-dimensionalized in the same manner as the roll angle accounting for the wave amplitude, wave number, and wavelength.

$$\frac{\theta(t)}{Ak} = \frac{g\theta}{A(2\pi f_p)^2} \tag{5.17}$$

The data reduction equation for pitch causes the resulting partial derivatives to be used as sensitivity coefficients.

$$\theta_{\theta,\theta/Ak} = \frac{\partial(\theta/Ak)}{\partial(\theta)} = \frac{g}{A(2\pi f_p)^2} \tag{5.18}$$

$$\theta_{g,\theta/Ak} = \frac{\partial(\theta/Ak)}{\partial(g)} = \frac{\theta}{A(2\pi f_p)^2} \tag{5.19}$$

$$\theta_{A,\theta/Ak} = \frac{\partial(\theta/Ak)}{\partial(A)} = -\frac{g\theta}{A^2(2\pi f_p)^2} \tag{5.20}$$

$$\theta_{f_p,\theta/Ak} = \frac{\partial(\theta/Ak)}{\partial(f_p)} = -\frac{4\pi g\theta}{A(2\pi f_p)^3} \tag{5.21}$$

From the partial derivatives the systematic standard uncertainty for pitch angle can be calculated as follows:

$$b^2_{\theta/Ak} = b^2_\theta\theta^2_{\theta,\theta/Ak} + b^2_g\theta^2_{g,\theta/Ak} + b^2_A\theta^2_{A,\theta/Ak} + b^2_{f_p}\theta^2_{f_p,\theta/Ak} \tag{5.22}$$

A lower 1st harmonic amplitude was found for the pitch angle when traveling with a heading of 90°, resulting in a higher than expected uncertainty but still a reasonable 10%. Other headings had uncertainties below 2%. The motions that the ship model displayed during testing followed harmonic motions resulting in small amplitudes for the 0th and 2nd harmonics. The combination of these small amplitudes and similar sized uncertainty values resulted in large uncertainty percentages with the largest for both 0th and 2nd being observed when the model proceeds in following waves. Uncertainties for pitch were small for all values when observing the 1st harmonic amplitudes but largest for the beam waves where the pitch was least affected by the waves. The repeatability of the pitch angle was difficult to maintain between tests. This resulted in a small contribution to the uncertainty from the systematic sources.

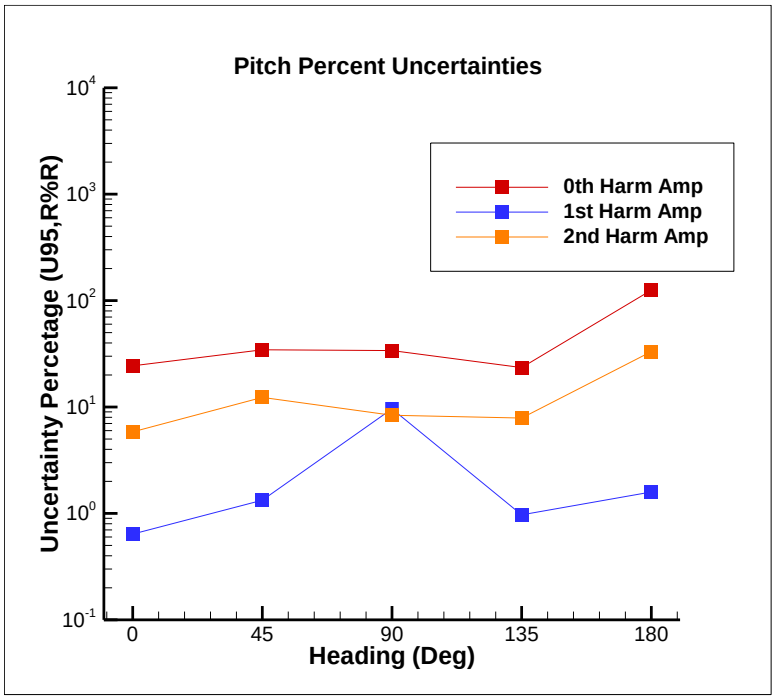

Figure 5.11: Uncertainties for pitch angle with different headings

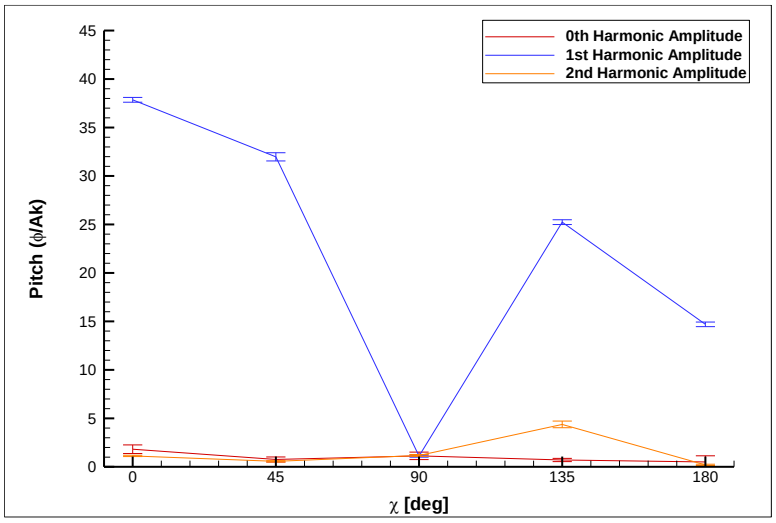

Figure 5.12: Pitch angle harmonic amplitudes with error bars

Table 5.12: Harmonic amplitude uncertainties for pitch

Test Case		Heading ψ_c	# of runs (M)	$\overline{\theta / Ak}$	$\theta_\theta^2 \cdot b_\theta^2$ $\%b_{\theta/Ak}^2$	$\theta_g^2 \cdot b_g^2$ $\%b_{\theta/Ak}^2$	$\theta_A^2 \cdot b_A^2$ $\%b_{\theta/Ak}^2$	$\theta_{f_p}^2 \cdot b_{f_p}^2$ $\%b_{\theta/Ak}^2$	$b_{\theta/Ak}$ $\%\overline{\theta / Ak}$	$s_{\overline{\theta/Ak}}$ $\%\overline{\theta / Ak}$	$u_{\theta/Ak}$ $\%\overline{\theta / Ak}$	$b_{\theta/Ak}^2$ $\%u_{\theta/Ak}^2$	$s_{\overline{\theta/Ak}}^2$ $\%u_{\theta/Ak}^2$	$U_{95,\theta/Ak}$ $\%\overline{\theta / Ak}$
0th Amp	Case 3.12	0	3	1.82	4.52	0.00	0.00	95.48	1.68	12.07	12.19	1.89	98.11	24.38
	Case 3.13	-45	3	0.76	21.43	0.00	0.00	78.57	1.85	17.16	17.26	1.15	98.85	34.51
		-90	3	1.13	10.91	0.00	0.00	89.09	1.74	16.85	16.94	1.05	98.95	33.88
		-135	3	0.71	23.97	0.00	0.00	76.03	1.88	11.58	11.73	2.57	97.43	23.47
		-180	3	0.50	38.16	0.00	0.00	61.84	2.09	62.66	62.70	0.11	99.89	125.40
1st Amp	Case 3.12	0	3	37.86	0.52	0.00	0.00	99.48	0.24	0.22	0.32	54.15	45.85	0.64
	Case 3.13	-45	3	32.36	0.71	0.00	0.00	99.29	0.24	0.60	0.64	13.62	86.38	1.29
		-90	3	1.10	86.04	0.00	0.00	13.96	0.63	4.76	4.80	1.74	98.26	9.60
		-135	3	25.11	1.18	0.00	0.00	98.82	0.24	0.38	0.45	27.71	72.29	0.90
		-180	3	14.70	3.37	0.00	0.00	96.63	0.24	0.76	0.80	9.13	90.87	1.59
2nd Amp	Case 3.12	0	3	1.12	85.64	0.00	0.00	14.36	0.62	2.86	2.92	4.56	95.44	5.85
	Case 3.13	-45	3	0.52	96.51	0.00	0.00	3.49	1.27	6.83	6.94	3.33	96.67	13.89
		-90	3	1.17	84.58	0.00	0.00	15.42	0.60	4.14	4.19	2.07	97.93	8.37
		-135	3	4.24	29.49	0.00	0.00	70.51	0.28	4.18	4.19	0.45	99.55	8.38
		-180	3	0.20	99.46	0.00	0.00	0.54	3.23	16.01	16.33	3.92	96.08	32.66

Table 5.13: Harmonic phase uncertainties for pitch

Test Case		Heading ψ_c	# of runs (M)	$\overline{\theta / Ak}$	$\theta_\theta^2 \cdot b_\theta^2$ $\%b_{\theta/Ak}^2$	$\theta_g^2 \cdot b_g^2$ $\%b_{\theta/Ak}^2$	$\theta_A^2 \cdot b_A^2$ $\%b_{\theta/Ak}^2$	$\theta_{f_p}^2 \cdot b_{f_p}^2$ $\%b_{\theta/Ak}^2$	$b_{\theta/Ak}$ $\%2\pi$	$s_{\overline{\theta/Ak}}$ $\%2\pi$	$u_{\theta/Ak}$ $\%2\pi$	$b_{\theta/Ak}^2$ $\%u_{\theta/Ak}^2$	$s_{\overline{\theta/Ak}}^2$ $\%u_{\theta/Ak}^2$	$U_{95,\theta/Ak}$ $\%2\pi$
1st Phase	Case 3.12	0	3	2.59	0.44	0.00	0.00	99.56	1.56	2.04	2.56	36.86	63.14	5.13
	Case 3.13	-45	3	0.44	13.37	0.00	0.00	86.63	0.28	2.19	2.21	1.63	98.37	4.42
		-90	3	-2.74	0.39	0.00	0.00	99.61	1.65	0.61	1.76	88.05	11.95	3.51
		-135	3	-0.85	3.92	0.00	0.00	96.08	0.52	31.38	31.38	0.03	99.97	62.76
		-180	3	0.57	8.45	0.00	0.00	91.55	0.36	1.14	1.19	8.87	91.13	2.39
2nd Phase	Case 3.12	0	3	-1.07	2.54	0.00	0.00	97.46	0.65	3.83	3.88	2.80	97.20	7.76
	Case 3.13	-45	3	-0.94	3.26	0.00	0.00	96.74	0.57	29.10	29.10	0.04	99.96	58.21
		-90	3	0.69	5.90	0.00	0.00	94.09	0.43	1.01	1.09	15.17	84.83	2.18
		-135	3	-0.95	3.16	0.00	0.00	96.84	0.58	5.12	5.16	1.27	98.73	10.31
		-180	3	0.61	7.50	0.00	0.00	92.50	0.38	27.07	27.07	0.02	99.98	54.14

5.1.7 Yaw Angle

The yaw angle is non-dimensionalized in the same way as pitch and roll angle, with the difference being in how the yaw angle is found. The yaw angle is the sum of the sub-carriage rotation (CPT) and the deviation from the sub-carriage rotation that the ship model has (DPT) as measured by the 6DOF-VMCS.

$$\frac{\psi(t)}{Ak} = \frac{\psi g}{A\left(2\pi f_p\right)^2} = \frac{\left(CPT + DPT\right)g}{A\left(2\pi f_p\right)^2} \tag{5.23}$$

From the data reduction equation the partial derivatives are found to calculate the sensitivity coefficients for yaw angle.

$$\theta_{CPT,\psi/Ak} = \frac{\partial\left(\psi / Ak\right)}{\partial\left(CPT\right)} = \frac{g}{A\left(2\pi f_p\right)^2} \tag{5.24}$$

$$\theta_{DPT,\psi/Ak} = \frac{\partial\left(\psi / Ak\right)}{\partial\left(DPT\right)} = \frac{g}{A\left(2\pi f_p\right)^2} \tag{5.25}$$

$$\theta_{g,\psi/Ak} = \frac{\partial\left(\psi / Ak\right)}{\partial\left(g\right)} = \frac{\left(CPT + DPT\right)}{A\left(2\pi f_p\right)^2} \tag{5.26}$$

$$\theta_{A,\psi/Ak} = \frac{\partial\left(\psi / Ak\right)}{\partial\left(A\right)} = -\frac{\left(CPT + DPT\right)g}{A^2\left(2\pi f_p\right)^2} \tag{5.27}$$

$$\theta_{f_p,\psi/Ak} = \frac{\partial\left(\psi / Ak\right)}{\partial\left(f_p\right)} = -\frac{4\pi g\left(CPT + DPT\right)}{A\left(2\pi f_p\right)^3} \tag{5.28}$$

The resulting systematic standard uncertainty for yaw angle can be found by:

$$b_{\psi/Ak}^2 = b_{CPT}^2\theta_{CPT,\psi/Ak}^2 + b_{DPT}^2\theta_{DPT,\psi/Ak}^2 + b_g^2\theta_{g,\psi/Ak}^2 + b_A^2\theta_{A,\psi/Ak}^2 + b_{f_p}^2\theta_{f_p,\psi/Ak}^2 \quad (5.29)$$

Throughout all headings except for 45° the model displayed very little change in yaw, resulting in higher than expected uncertainties for 0^{th} harmonic amplitudes. When analyzing the 1^{st} harmonic amplitude the head and following wave cases displayed large percent uncertainties due to the low amounts of rotational motion when the bow or stern directly interact with the wave at such a small angle. This results in very little yawing motion and a resulting larger uncertainty. The largest contributor for yaw uncertainty changed drastically depending on the heading of the model and the reported standard deviation measured. In cases where the reported yaw angles were small the repeatability was the largest contributor while the opposite occurred if large angles were reported.

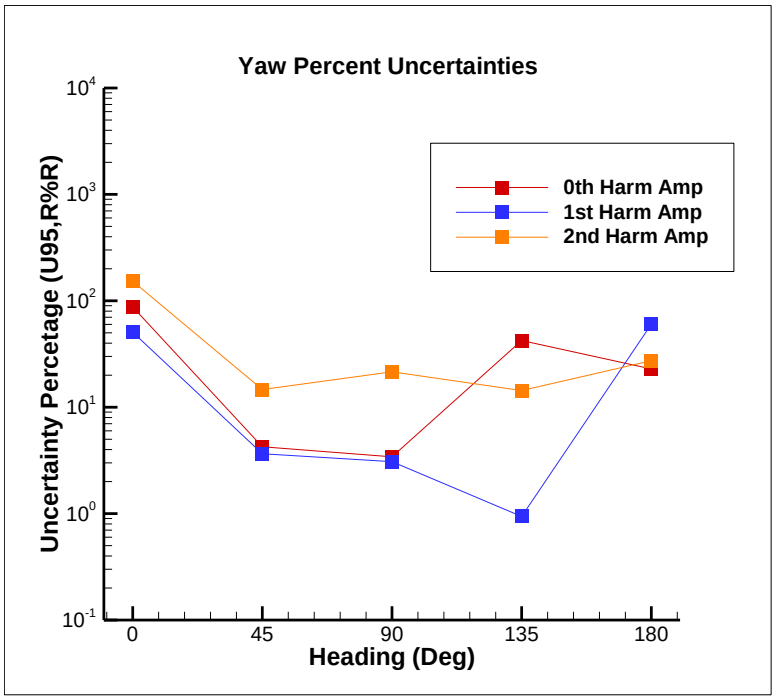

Figure 5.13: Uncertainties for yaw angle with different headings

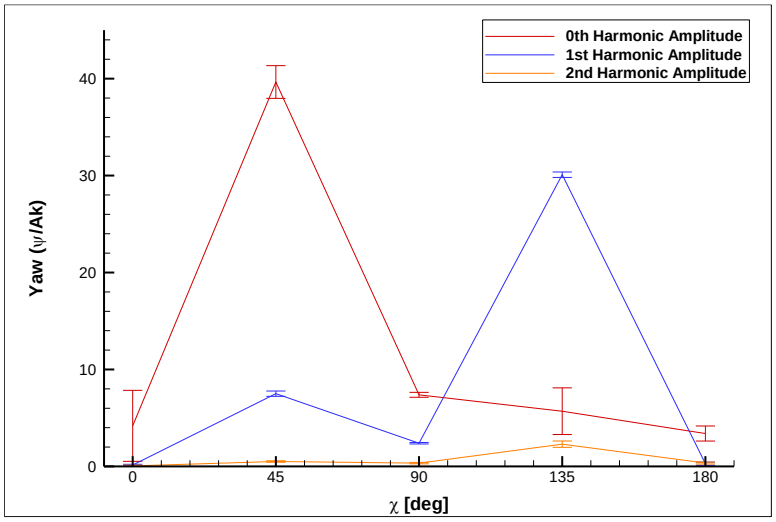

Figure 5.14: Yaw angle harmonic amplitudes with error bars

Table 5.14: Harmonic amplitude uncertainties for yaw

Test Case		Heading ψ_c	# of runs (M)	$\overline{\psi / Ak}$	$\theta_{\psi}^2 \cdot b_{\psi}^2$ $\%b_{\psi/Ak}^2$	$\theta_g^2 \cdot b_g^2$ $\%b_{\psi/Ak}^2$	$\theta_A^2 \cdot b_A^2$ $\%b_{\psi/Ak}^2$	$\theta_{f_p}^2 \cdot b_{f_p}^2$ $\%b_{\psi/Ak}^2$	$b_{\psi/Ak}$ $\%\overline{\psi / Ak}$	$s_{\overline{\psi/Ak}}$ $\%\psi / Ak$	$u_{\psi/Ak}$ $\%\overline{\psi / Ak}$	$b_{\psi/Ak}^2$ $\%u_{\psi/Ak}^2$	$s_{\overline{\psi/Ak}}^2$ $\%u_{\psi/Ak}^2$	$U_{95,\psi/Ak}$ $\%\overline{\psi / Ak}$
0th Amp	Case 3.12	0	3	4.18	0.58	0.00	0.00	99.42	1.64	43.90	43.94	0.14	99.86	87.87
	Case 3.13	-45	3	39.77	0.01	0.00	0.00	99.99	1.64	1.36	2.13	59.21	40.79	4.26
		-90	3	7.44	0.19	0.00	0.00	99.81	1.64	3.01	3.43	22.95	77.05	6.85
		-135	3	5.98	0.29	0.00	0.00	99.71	1.64	20.33	20.40	0.65	99.35	40.80
		-180	3	3.43	0.87	0.00	0.00	99.13	1.65	11.21	11.33	2.11	97.89	22.67
1st Amp	Case 3.12	0	3	0.13	99.64	0.00	0.00	0.36	3.93	2.87	4.87	65.23	34.77	9.74
	Case 3.13	-45	3	7.94	7.25	0.00	0.00	92.75	0.25	0.00	0.25	100.00	0.00	0.49
		-90	3	2.51	43.96	0.00	0.00	56.04	0.32	1.00	1.05	9.02	90.98	2.11
		-135	3	31.62	0.49	0.00	0.00	99.51	0.24	0.31	0.39	36.70	63.30	0.78
		-180	3	0.29	98.32	0.00	0.00	1.68	1.83	23.80	23.87	0.59	99.41	47.74
2nd Amp	Case 3.12	0	3	0.04	99.97	0.00	0.00	0.03	13.08	24.95	28.17	21.57	78.43	56.34
	Case 3.13	-45	3	0.53	94.67	0.00	0.00	5.33	1.02	1.28	1.64	39.14	60.86	3.28
		-90	3	0.36	97.41	0.00	0.00	2.59	1.47	9.14	9.26	2.52	97.48	18.52
		-135	3	2.34	47.29	0.00	0.00	52.71	0.33	8.75	8.76	0.14	99.86	17.51
		-180	3	0.36	97.46	0.00	0.00	2.54	1.48	9.40	9.52	2.43	97.57	19.03

Table 5.15: Harmonic phase uncertainties for yaw

Test Case		Heading ψ_c	# of runs (M)	$\overline{\psi / Ak}$	$\theta_{\psi}^2 \cdot b_{\psi}^2$ $\%b_{\psi/Ak}^2$	$\theta_g^2 \cdot b_g^2$ $\%b_{\psi/Ak}^2$	$\theta_A^2 \cdot b_A^2$ $\%b_{\psi/Ak}^2$	$\theta_{f_p}^2 \cdot b_{f_p}^2$ $\%b_{\psi/Ak}^2$	$b_{\psi/Ak}$ $\%2\pi$	$s_{\overline{\psi/Ak}}$ $\%2\pi$	$u_{\psi/Ak}$ $\%2\pi$	$b_{\psi/Ak}^2$ $\%u_{\psi/Ak}^2$	$s_{\overline{\psi/Ak}}^2$ $\%u_{\psi/Ak}^2$	$U_{95,\psi/Ak}$ $\%2\pi$
1st Phase	Case 3.12	0	3	-2.82	0.24	0.00	0.00	99.76	1.69	0.67	1.82	86.49	13.51	3.64
	Case 3.13	-45	3	2.32	0.36	0.00	0.00	99.64	1.39	2.13	2.55	29.93	70.07	5.09
		-90	3	1.00	1.89	0.00	0.00	98.11	0.61	0.80	1.01	36.46	63.54	2.01
		-135	3	-1.68	0.69	0.00	0.00	99.31	1.01	0.00	1.01	100.00	0.00	2.02
		-180	3	2.02	0.48	0.00	0.00	99.52	1.21	12.10	12.16	0.99	99.01	24.32
2nd Phase	Case 3.12	0	3	-0.87	2.51	0.00	0.00	97.49	0.53	17.57	17.58	0.09	99.91	35.15
	Case 3.13	-45	3	-1.69	0.68	0.00	0.00	99.32	1.01	4.23	4.35	5.43	94.57	8.70
		-90	3	0.23	27.03	0.00	0.00	72.97	0.16	3.97	3.98	0.16	99.84	7.96
		-135	3	-0.05	86.88	0.00	0.00	13.12	0.09	6.28	6.28	0.02	99.98	12.56
		-180	3	-1.01	1.86	0.00	0.00	98.14	0.61	5.54	5.57	1.21	98.79	11.14

5.1.8 Surge Velocity

The uncertainties for the surge velocity are found based on the process and equations used and described in Section 4.2.3. Head and following waves result in the largest speed changes in the longitudinal direction as expected. When quartering and beam waves encounter the ship the magnitude of the motions is lower resulting in a larger uncertainty when the 1st harmonic amplitude is analyzed. Additionally the head and following waves have the highest percent uncertainty due to repeatability errors signifying that these motions are less consistent between trials than the quartering and beam waves. The overall surge velocity is near the ideal ship speed of 1.11 m/s. Encountering the wave causes some lateral motion for the ship identified as the sway velocity when the ship heading is not 0° or 180°. Analyzing the 0th harmonic amplitude for all heading angles display a low percent uncertainty since the ship speed is predominately in the y-direction. The reported velocities remain fairly consistent in waves due to the design of the hull. This resulted in the uncertainty of the measurement being primarily systematic with the largest contributor varying between headings.

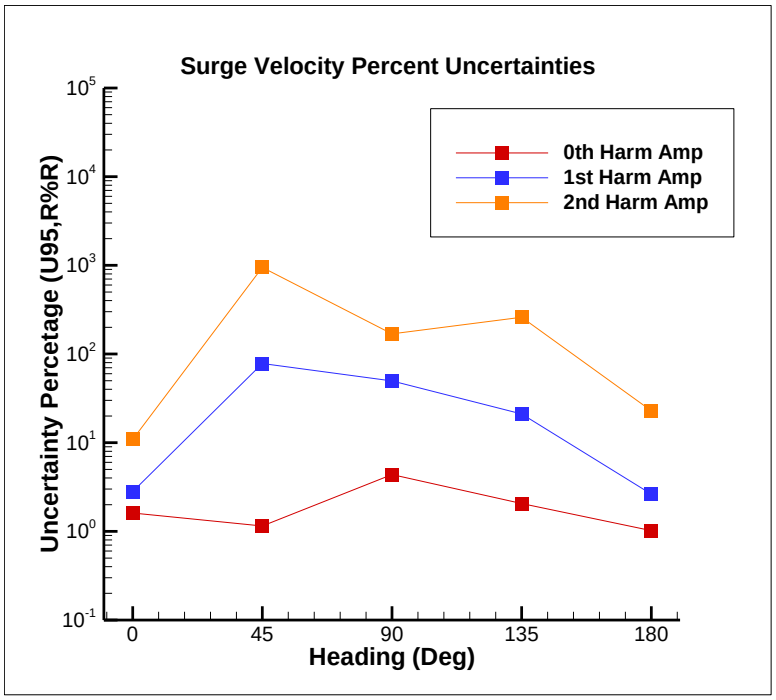

Figure 5.15: Uncertainties for surge velocity with different headings

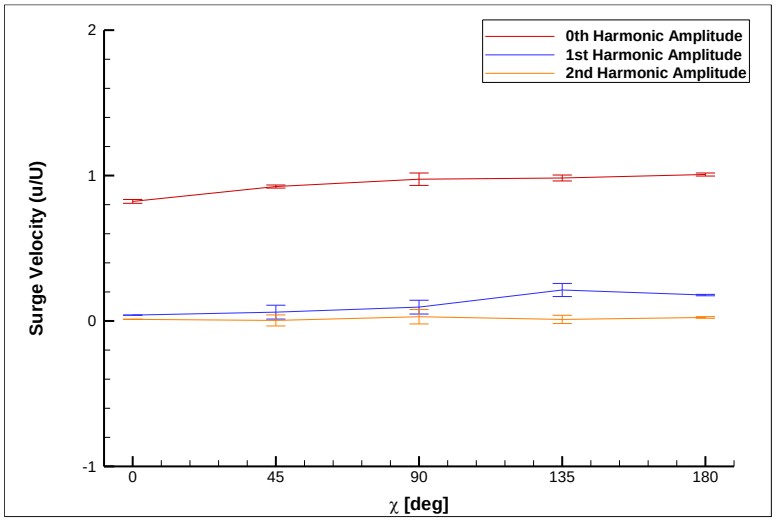

Figure 5.16: Surge velocity harmonic amplitudes with error bars

Table 5.16: Harmonic amplitude uncertainties for surge velocity

Test Case		Heading ψ_c	# of runs (M)	$\overline{u/U}$	$\theta^2_{dx/dt} \cdot b^2_{dx/dt}$ $\%b^2_{u/U}$	$\theta^2_{dy/dt} \cdot b^2_{dy/dt}$ $\%b^2_{u/U}$	$\theta^2_{\psi} \cdot b^2_{\psi}$ $\%b^2_{u/U}$	$b_{u/U}$ $\%\overline{u/U}$	$s_{\overline{u/U}}$ $\%\overline{u/U}$	$u_{u/U}$ $\%\overline{u/U}$	$b^2_{u/U}$ $\%u^2_{u/U}$	$s^2_{\overline{u/U}}$ $\%u^2_{u/U}$	$U_{95,u/U}$ $\%\overline{u/U}$
0th Amp	Case 3.12	0	3	0.82	0.00	96.42	3.58	0.49	0.06	0.49	98.27	1.73	0.99
	Case 3.13	-45	3	0.92	54.60	41.11	4.29	1.42	0.18	1.43	98.46	1.54	2.86
		-90	3	0.98	95.32	0.00	4.68	1.11	0.28	1.14	94.13	5.87	2.28
		-135	3	0.98	47.09	48.12	4.79	0.64	0.27	0.69	85.12	14.88	1.39
		-180	3	1.01	0.00	94.62	5.38	0.81	0.14	0.83	97.19	2.81	1.65
1st Amp	Case 3.12	0	3	0.01	0.00	96.45	3.55	1.23	3.51	3.72	11.01	88.99	7.44
	Case 3.13	-45	3	0.01	54.53	41.12	4.34	97.61	2.06	97.63	99.96	0.04	195.26
		-90	3	0.10	95.13	0.00	4.87	13.02	0.29	13.03	99.95	0.05	26.05
		-135	3	0.05	46.21	49.02	4.77	16.61	11.55	20.23	67.40	32.60	40.46
		-180	3	0.17	0.00	94.66	5.34	6.46	0.72	6.50	98.77	1.23	13.00
2nd Amp	Case 3.12	0	3	0.01	0.00	96.45	3.55	0.68	2.84	2.92	5.42	94.58	5.85
	Case 3.13	-45	3	0.00	54.71	41.04	4.26	366.51	24.68	367.34	99.55	0.45	734.68
		-90	3	0.04	94.83	0.00	5.16	24.63	0.33	24.63	99.98	0.02	49.26
		-135	3	0.01	46.44	48.65	4.92	24.76	24.71	34.98	50.09	49.91	69.96
		-180	3	0.02	0.00	94.87	5.13	53.19	10.68	54.26	96.12	3.88	108.51

Table 5.17: Harmonic phase uncertainties for surge velocity

Test Case		Heading ψ_c	# of runs (M)	$\overline{u/U}$	$\theta^2_{dx/dt} \cdot b^2_{dx/dt}$ $\%b^2_{u/U}$	$\theta^2_{dy/dt} \cdot b^2_{dy/dt}$ $\%b^2_{u/U}$	$\theta^2_{\psi} \cdot b^2_{\psi}$ $\%b^2_{u/U}$	$b_{u/U}$ $\%2\pi$	$s_{\overline{u/U}}$ $\%2\pi$	$u_{u/U}$ $\%2\pi$	$b^2_{u/U}$ $\%u^2_{u/U}$	$s^2_{\overline{u/U}}$ $\%u^2_{u/U}$	$U_{95,u/U}$ $\%2\pi$
1st Phase	Case 3.12	0	3	-1.81	0.00	96.36	3.64	0.08	2.04	2.04	0.14	99.86	4.08
	Case 3.13	-45	3	2.23	54.13	41.81	4.06	0.04	1.37	1.37	0.11	99.89	2.74
		-90	3	-2.27	95.06	0.00	4.94	0.21	3.52	3.53	0.35	99.65	7.05
		-135	3	2.56	46.52	48.93	4.55	0.21	4.13	4.13	0.25	99.75	8.26
		-180	3	2.20	0.00	95.06	4.94	0.17	1.48	1.49	1.32	98.68	2.97
2nd Phase	Case 3.12	0	3	0.15	0.00	96.65	3.35	0.19	3.17	3.18	0.37	99.63	6.35
	Case 3.13	-45	3	-0.74	54.05	41.55	4.40	0.22	2.84	2.84	0.59	99.41	5.69
		-90	3	0.83	95.03	0.00	4.97	0.20	18.80	18.80	0.01	99.99	37.60
		-135	3	0.79	46.24	48.94	4.82	0.11	4.21	4.21	0.06	99.94	8.43
		-180	3	1.09	0.00	94.71	5.29	0.19	2.90	2.91	0.43	99.57	5.82

5.1.9 Sway Velocity

To determine the uncertainties for the sway velocities at different harmonics the process described for zig zag maneuvers in Section 4.2.4 is used. In the opposite manner that head and following waves displayed the largest change in surge velocity these headings had almost no motion in their sway velocities. The resulting uncertainties were drastically larger than a reasonable value being on the order of 1000%. The beam waves displayed consistently larger harmonic amplitudes resulting in a lower uncertainty percentage. All three harmonic amplitudes display the same trend of having higher uncertainties during head and following wave cases with the lowest uncertainty found during beam waves. The reported standard deviation from sway velocities were consistently small percentages of the measured velocity. This resulted in all measurement being composed of mainly systematic uncertainties. Without a significant amount of sway velocity the systematic standard uncertainties will remain as the key source and an improvement on this is not feasible without designing a completely new measurement system that can report velocity with an extreme amount of accuracy.

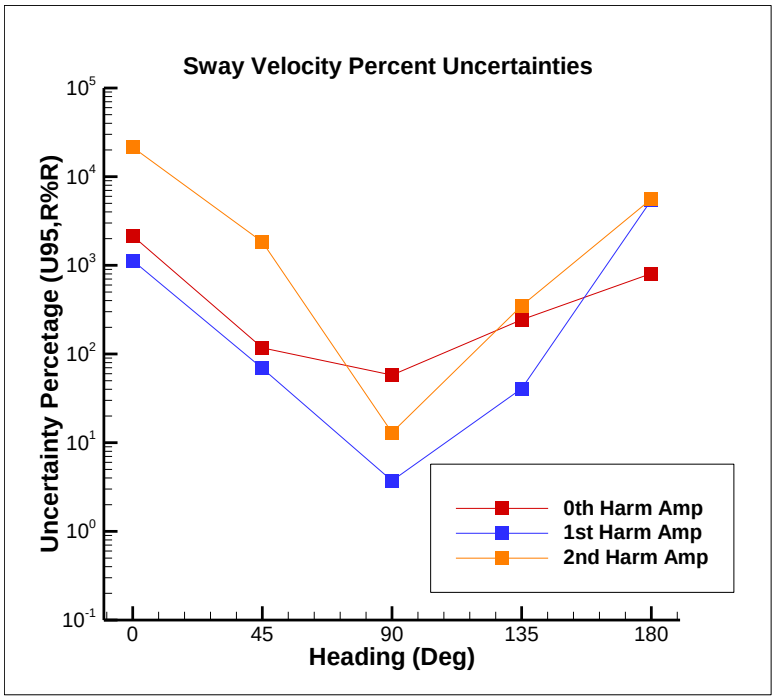

Figure 5.17: Uncertainties for sway velocity with different headings

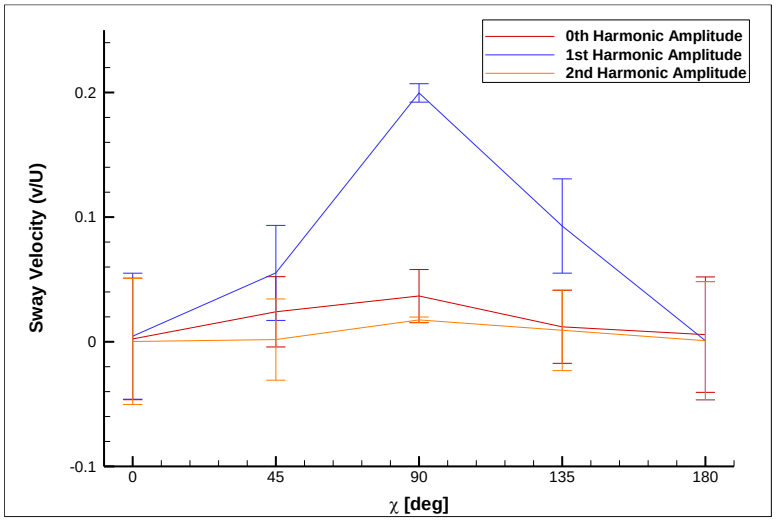

Figure 5.18: Sway velocity harmonic amplitudes with error bars

Table 5.18: Harmonic amplitude uncertainties for sway velocity

Test Case		Heading ψ_c	# of runs (M)	$\overline{v/U}$	$\theta^2_{dx/dt} \cdot b^2_{dx/dt}$ $\%b^2_{v/U}$	$\theta^2_{dy/dt} \cdot b^2_{dy/dt}$ $\%b^2_{v/U}$	$\theta^2_{\psi} \cdot b^2_{\psi}$ $\%b^2_{v/U}$	$b_{v/U}$ $\%\overline{v/U}$	$s_{\overline{v/U}}$ $\%\overline{v/U}$	$u_{v/U}$ $\%\overline{v/U}$	$b^2_{v/U}$ $\%u^2_{v/U}$	$s^2_{\overline{v/U}}$ $\%u^2_{v/U}$	$U_{95,v/U}$ $\%\overline{v/U}$
0th Amp	Case 3.12	0	3	0.00	0.00	96.41	3.59	515.51	26.24	516.17	99.74	0.26	1032.35
	Case 3.13	-45	3	0.03	45.46	34.23	20.31	21.62	4.61	22.10	95.64	4.36	44.21
		-90	3	0.01	95.18	0.00	4.82	155.84	21.42	157.31	98.15	1.85	314.61
		-135	3	0.01	48.71	49.78	1.51	110.33	6.05	110.49	99.70	0.30	220.98
		-180	3	0.01	0.00	94.67	5.33	174.98	3.50	175.02	99.96	0.04	350.04
1st Amp	Case 3.12	0	3	0.00	0.00	96.45	3.55	11160.06	3.19	11160.06	100.00	0.00	22320.13
	Case 3.13	-45	3	0.00	41.86	31.57	26.57	266.98	2.44	266.99	99.99	0.01	533.98
		-90	3	0.06	92.22	0.00	7.77	0.94	0.22	0.97	94.71	5.29	1.94
		-135	3	0.07	47.21	50.07	2.72	14.69	0.41	14.70	99.92	0.08	29.40
		-180	3	0.00	0.00	94.78	5.22	1224.68	15.99	1224.78	99.98	0.02	2449.56
2nd Amp	Case 3.12	0	3	0.00	0.00	96.45	3.55	29138.87	15.16	29138.87	100.00	0.00	58277.74
	Case 3.13	-45	3	0.00	52.69	39.52	7.79	3816.85	39.58	3817.06	99.99	0.01	7634.12
		-90	3	0.00	94.97	0.00	5.02	339.76	3.81	339.78	99.99	0.01	679.57
		-135	3	0.00	48.76	51.08	0.15	480.67	7.32	480.73	99.98	0.02	961.45
		-180	3	0.00	0.00	97.88	2.12	37.54	41.58	56.02	44.90	55.10	112.04

Table 5.19: Harmonic phase uncertainties for sway velocity

Test Case		Heading ψ_c	# of runs (M)	$\overline{v/U}$	$\theta^2_{dx/dt} \cdot b^2_{dx/dt}$ $\%b^2_{v/U}$	$\theta^2_{dy/dt} \cdot b^2_{dy/dt}$ $\%b^2_{v/U}$	$\theta^2_{\psi} \cdot b^2_{\psi}$ $\%b^2_{v/U}$	$b_{v/U}$ $\%2\pi$	$s_{\overline{v/U}}$ $\%2\pi$	$u_{v/U}$ $\%2\pi$	$b^2_{v/U}$ $\%u^2_{v/U}$	$s^2_{\overline{v/U}}$ $\%u^2_{v/U}$	$U_{95,v/U}$ $\%2\pi$
1st Phase	Case 3.12	0	3	-2.51	0.00	96.35	3.65	0.23	2.40	2.41	0.92	99.08	4.82
	Case 3.13	-45	3	-1.89	56.15	43.37	0.47	0.22	1.58	1.59	1.94	98.06	3.19
		-90	3	1.58	96.05	0.00	3.94	0.02	0.30	0.30	0.50	99.50	0.60
		-135	3	1.62	32.66	34.36	32.98	0.08	2.00	2.00	0.15	99.85	4.01
		-180	3	2.94	0.00	94.98	5.02	0.12	1.51	1.51	0.63	99.37	3.03
2nd Phase	Case 3.12	0	3	-0.49	0.00	96.67	3.33	0.16	10.97	10.97	0.02	99.98	21.94
	Case 3.13	-45	3	1.18	20.58	15.82	63.60	0.06	27.24	27.24	0.00	100.00	54.48
		-90	3	-0.35	95.63	0.00	4.37	0.04	2.40	2.40	0.02	99.98	4.79
		-135	3	-1.99	47.83	50.63	1.55	0.18	4.98	4.98	0.13	99.87	9.96
		-180	3	1.05	0.00	94.87	5.13	0.07	4.28	4.28	0.03	99.97	8.56

5.1.10 Ship Speed

The ship speed represents the speed that the model is traveling at without a relation to the direction. When analyzing the uncertainty of the ship speed the 0^{th} harmonic amplitudes best describes the motions. The reported uncertainties were very consistent with a range of 6-7% and the higher uncertainties were reported when the average ship speed was lowest. Larger uncertainties are reported for both the 1^{st} and 2^{nd} harmonic amplitudes due to the ship speed not changing severely with harmonic motions. The ship speed was very consistent throughout all tests resulting in a small amount of uncertainty from repeatability. The uncertainty on ship speed was almost entirely systematic standard uncertainties with the largest contributor coming from the initial ship speed due to the model being released inconsistently between tests.

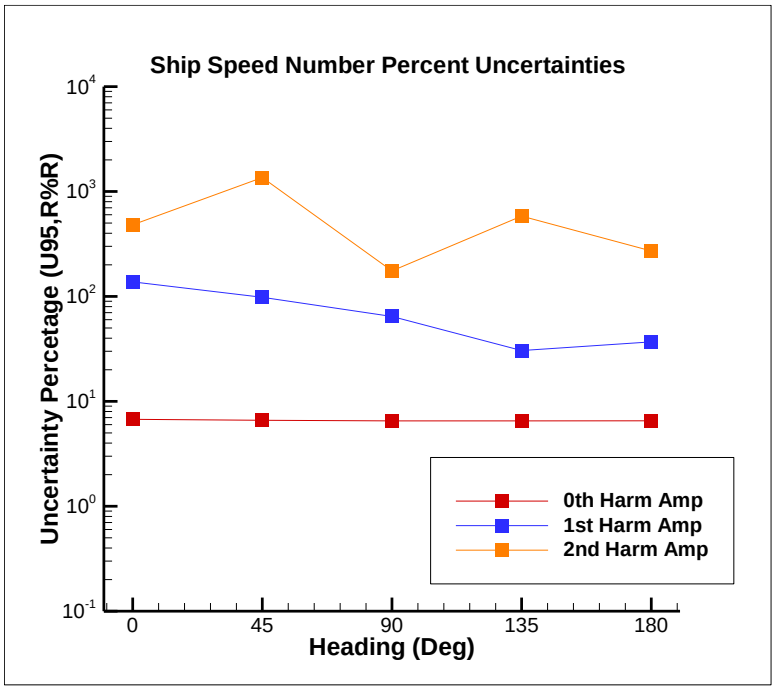

Figure 5.19: Uncertainties for ship speed with different headings

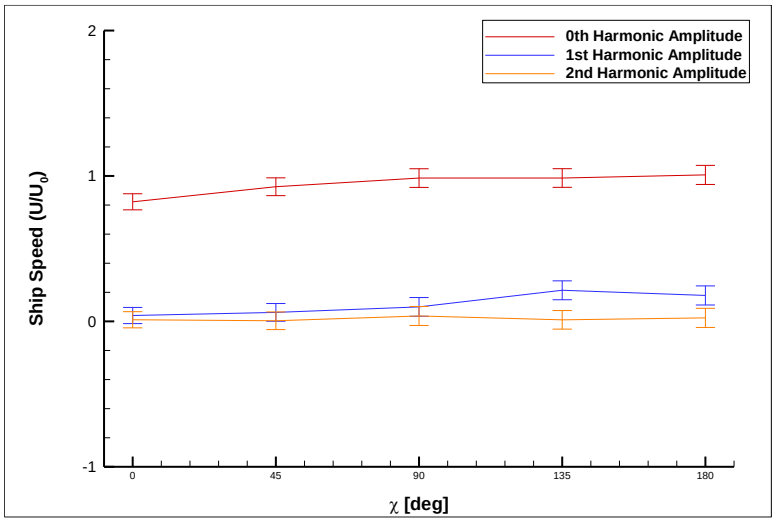

Figure 5.20: Ship speed harmonic amplitudes with error bars

Table 5.20: Harmonic amplitudes for ship speed

Test Case		Heading ψ_c	# of runs (M)	U/U_0	$\theta^2_{dx/dt} \cdot b^2_{dx/dt}$ $\%b^2_{U/U_0}$	$\theta^2_{dy/dt} \cdot b^2_{dy/dt}$ $\%b^2_{U/U_0}$	$\theta^2_{U_0} \cdot b^2_{U_0}$ $\%b^2_{U/U_0}$	b_{U/U_0} $\%U/U_0$	$s_{\overline{U/U_0}}$ $\%U/U_0$	u_{U/U_0} $\%U/U_0$	b^2_{U/U_0} $\%u^2_{U/U_0}$	s^2_{U/U_0} $\%u^2_{U/U_0}$	$U_{95,U/U_0}$ $\%U/U_0$
0th Amp	Case 3.12	0	3	0.82	22.01	0.00	77.99	3.37	0.06	3.37	99.97	0.03	6.74
		-45	3	0.93	8.02	10.68	81.30	3.30	0.18	3.30	99.69	0.31	6.60
	Case 3.13	-90	3	0.99	0.00	16.49	83.51	3.25	0.17	3.25	99.73	0.27	6.51
		-135	3	0.99	8.20	7.73	84.06	3.24	0.28	3.25	99.25	0.75	6.51
		-180	3	1.01	16.33	0.00	83.67	3.25	0.14	3.26	99.81	0.19	6.52
1st Amp	Case 3.12	0	3	0.04	22.22	0.00	77.78	68.80	1.26	68.82	99.97	0.03	137.63
		-45	3	0.06	7.47	9.89	82.64	48.88	4.36	49.07	99.21	0.79	98.15
	Case 3.13	-90	3	0.10	0.00	16.62	83.37	32.09	2.34	32.18	99.47	0.53	64.36
		-135	3	0.21	8.42	8.19	83.40	14.99	2.72	15.24	96.81	3.19	30.48
		-180	3	0.18	16.45	0.00	83.55	18.40	1.30	18.44	99.50	0.50	36.89
2nd Amp	Case 3.12	0	3	0.01	22.23	0.00	77.77	240.82	5.34	240.88	99.95	0.05	481.75
		-45	3	0.00	7.72	10.14	82.14	678.99	28.66	679.60	99.82	0.18	1359.20
	Case 3.13	-90	3	0.04	0.00	16.78	83.22	85.94	16.75	87.56	96.34	3.66	175.12
		-135	3	0.01	8.28	7.77	83.95	291.15	9.94	291.32	99.88	0.12	582.65
		-180	3	0.02	16.44	0.00	83.56	135.15	11.29	135.62	99.31	0.69	271.24

Table 5.21: Harmonic phases for ship speed

Test Case		Heading ψ_c	# of runs (M)	U/U_0	$\theta^2_{dx/dt} \cdot b^2_{dx/dt}$ $\%b^2_{U/U_0}$	$\theta^2_{dy/dt} \cdot b^2_{dy/dt}$ $\%b^2_{U/U_0}$	$\theta^2_{U_0} \cdot b^2_{U_0}$ $\%b^2_{U/U_0}$	b_{U/U_0} $\%2\pi$	$s_{\overline{U/U_0}}$ $\%2\pi$	u_{U/U_0} $\%2\pi$	b^2_{U/U_0} $\%2\pi$	s^2_{U/U_0} $\%2\pi$	$U_{95,U/U_0}$ $\%2\pi$
1st Phase	Case 3.12	0	3	-0.31	21.68	0.00	78.32	0.44	0.37	0.57	58.75	41.25	1.15
	Case 3.13	-45	3	-0.06	7.90	10.66	81.44	0.49	0.46	0.67	52.48	47.52	1.34
		-90	3	0.20	0.00	16.44	83.56	0.51	4.96	4.99	1.04	98.96	9.98
		-135	3	-0.18	8.50	8.24	83.26	0.51	5.53	5.56	0.85	99.15	11.11
		-180	3	0.39	16.66	0.00	83.34	0.52	0.27	0.59	79.46	20.54	1.17
2nd Phase	Case 3.12	0	3	0.05	21.82	0.00	78.18	0.44	0.52	0.68	41.96	58.04	1.36
	Case 3.13	-45	3	-0.28	7.35	9.93	82.72	0.48	0.37	0.61	62.32	37.68	1.22
		-90	3	-0.45	0.00	16.54	83.46	0.51	0.43	0.67	58.51	41.49	1.33
		-135	3	0.07	7.97	7.71	84.33	0.51	0.23	0.56	83.06	16.94	1.11
		-180	3	0.20	16.80	0.00	83.20	0.52	0.54	0.75	48.45	51.55	1.50

5.1.11 Course Keeping in Waves Conclusions

Overall the uncertainties of the measured values during wave cases were relatively small. If the motion most closely followed the wave encounter frequency the 1st harmonic amplitude accurately described the motion. Some outliers to this idea are the surge and sway velocity. In these cases the model would react differently depending on the heading causing a large variance in the reported uncertainties due to the reported harmonic amplitude. For motions that do no oscillate with the wave encounter frequency the 0th harmonic amplitude is a better representation of the overall motion and results in more accurate uncertainty percentages. Across the time history the beam waves display the largest deviation from the desired course.

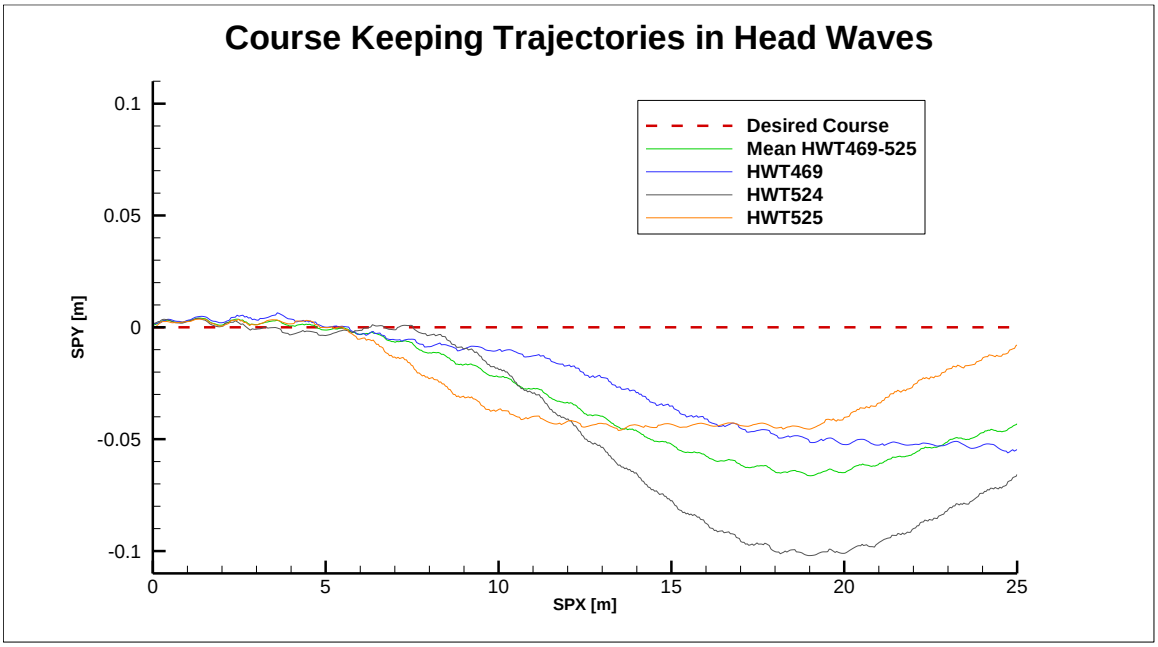

Figure 5.21: Course keeping trajectories in head waves with desired course

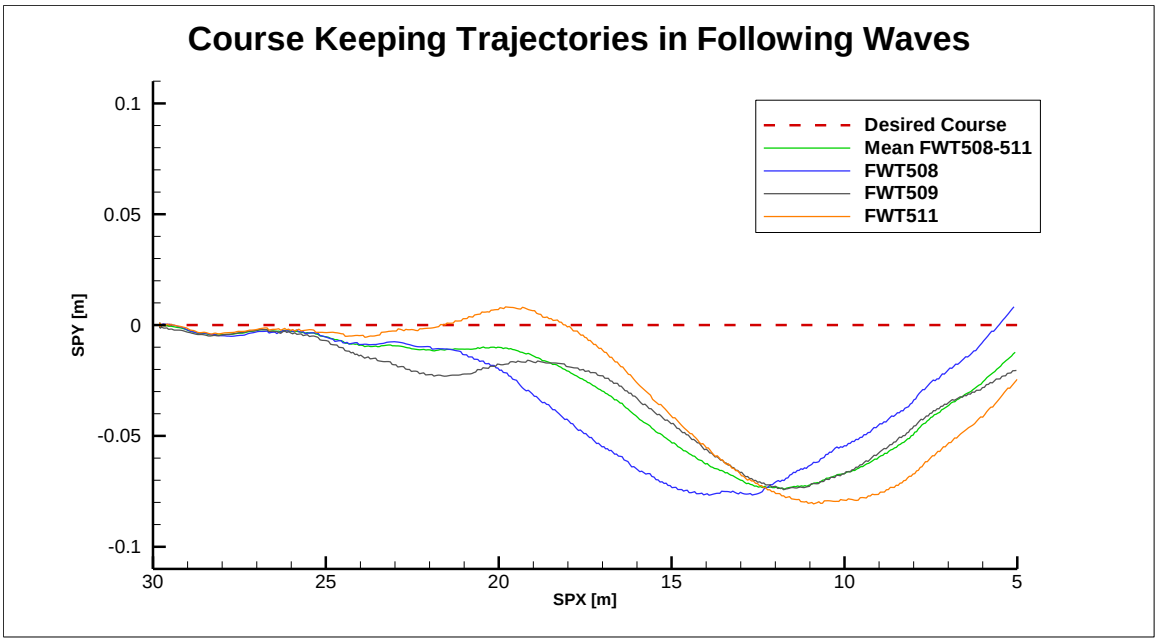

Figure 5.22: Course keeping trajectories in following waves with desired course

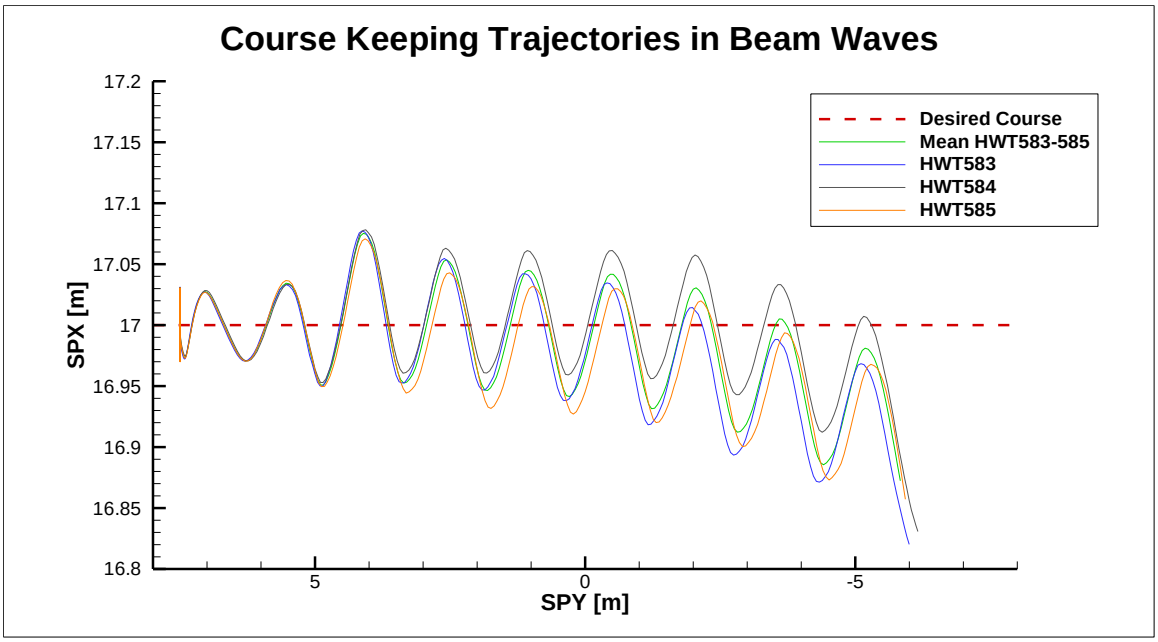

Figure 5.23: Course keeping trajectories in beam waves with desired course

5.2 Zig Zag Maneuver in Waves

Zig zag maneuvers were performed with an initial heading of zero degrees (towards the wavemakers) at a Froude Number of 0.20. The wavelength with respect to ship length and wave height with respect to wavelength were 1.0 and 0.02 respectively. The ship position and orientation, speed, and overshoot angles were analyzed. The location of the overshoot angles and heading were observed and the uncertainty at these points were calculated. Lower uncertainties for position were observed for the 1st overshoot angle due to the lower standard deviation at these points from the controlled start of the trial.

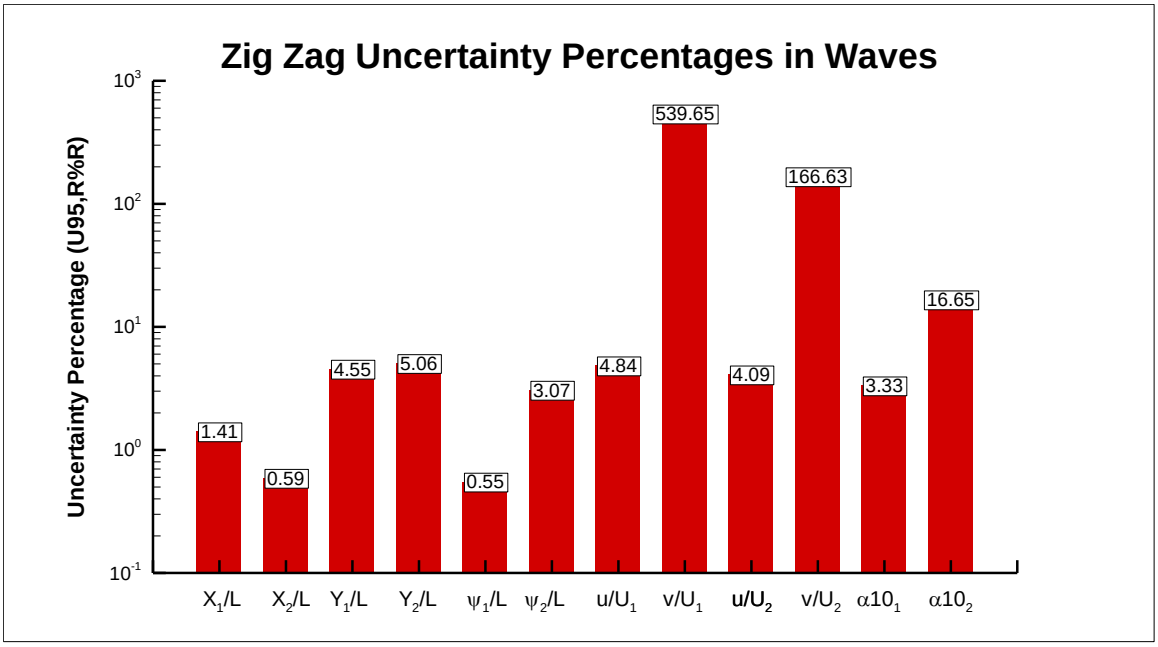

Figure 5.24: Uncertainties during zig zag tests in waves

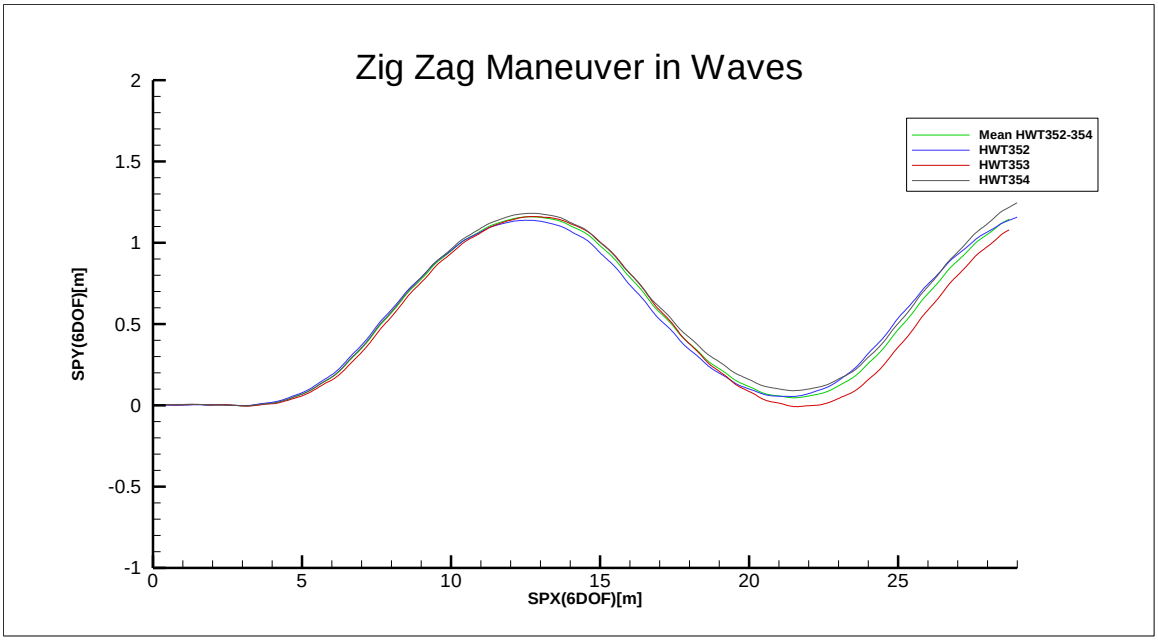

Figure 5.25: Zig Zag trajectory in waves

Table 5.22: Head waves zig zag uncertainties (Fr=0.20, λ/L=1.0, H/λ=0.02)

r	Mean	b_r %r	s_r %r	u_r %r	b_r^2 $\%u_r^2$	s_r^2 $\%u_r^2$	$U_{95,r}$ %r
X_1/L	2.0554	0.05	0.70	0.70	0.46	99.54	1.41
X_2/L	4.9304	0.02	0.29	0.29	0.46	99.54	0.59
Y_1/L	0.0798	1.25	1.91	2.28	29.93	70.07	4.55
Y_2/L	0.2829	0.35	2.51	2.53	1.92	98.08	5.06
ψ_1	12.27	0.16	0.22	0.28	35.06	64.94	0.55
ψ_2	-12.47	-0.16	-1.53	-1.54	1.09	98.91	-3.07
u/U_1	0.89	1.88	1.52	2.42	60.56	39.44	4.84
v/U_1	0.00	242.93	117.42	-269.82	81.06	18.94	539.65
u/U_2	0.86	1.95	0.62	2.05	90.80	9.20	4.09
v/U_1	-0.01	74.93	36.42	-83.31	80.89	19.11	166.63
$\alpha 10_1$	2.08	0.29	1.62	1.64	3.04	96.96	3.28
$\alpha 10_2$	-2.55	-0.11	8.32	-8.33	0.02	99.98	16.65

5.3 Turning Circle Maneuver in Waves

The turning circle were completed with a short approach and an initial heading toward the wave makers. Similar to the calm water tests turning circles were performed with both positive and negative 35 degree rudder angles. The two sets of trials were compared to observe the uncertainty in the measured advance, transfer, and tactical diameter positions throughout the basin. The X-position, Y-position, and yaw angle at each of these points were compared and the uncertainty of the measurement was found in addition to the uncertainty of the advance, transfer, and tactical diameters. These uncertainties were similar between rudder angles with comparable measurements and the largest difference between the two trials demonstrate the repeatability errors.

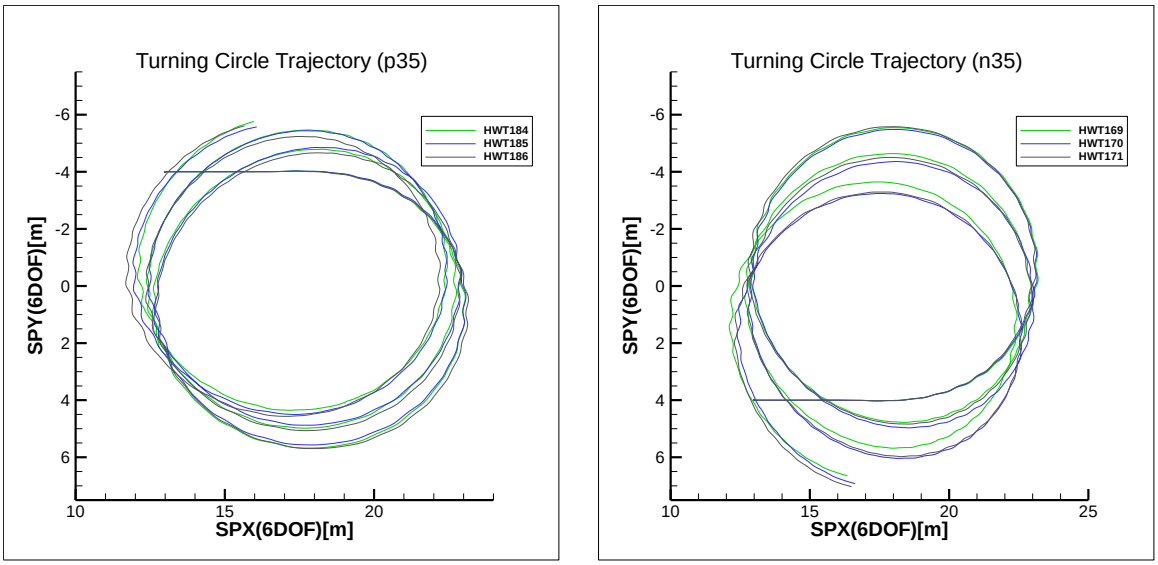

Figure 5.26: Turning circle trajectories in waves

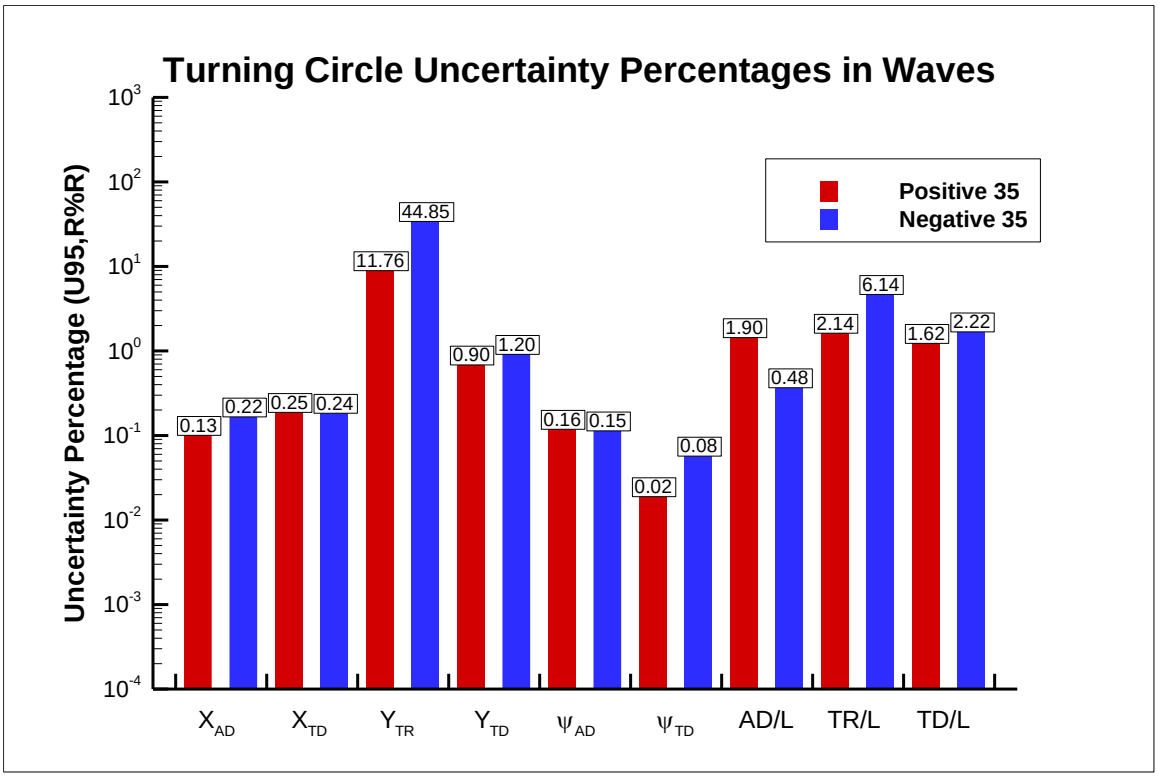

Figure 5.27: Uncertainty for turning circles in waves

Table 5.23: Turning circle in waves uncertainties (Fr=0.20, λ/L=1.0, H/λ=0.02, δ=35)

r	Mean	b_r %r	s_r %r	u_r %r	b_r^2 $\%u_r^2$	s_r^2 $\%u_r^2$	$U_{95,r}$ %r
X_{AD}/L	7.2893	0.01	0.11	0.11	1.46	98.54	0.22
X_{TD}/L	6.0261	0.02	0.12	0.12	1.74	98.26	0.24
Y_{TR}/L	-0.0528	-1.84	-22.42	-22.50	0.67	99.33	-44.99
Y_{TD}/L	1.7622	0.06	0.60	0.60	0.84	99.16	1.21
ψ_{AD}	90.01	0.02	0.07	0.07	8.85	91.15	0.15
ψ_{TD}	179.84	0.01	0.04	0.04	8.74	91.26	0.08
AD/L	2.21	0.14	0.20	0.24	32.03	67.97	0.48
TR/L	1.22	0.24	3.06	3.07	0.61	99.39	6.14
TD/L	3.03	0.10	1.10	1.11	0.76	99.24	2.22

Table 5.24: Turning circle in waves uncertainties (Fr=0.20, λ/L=1.0, H/λ=0.02, δ=-35)

r	Mean	b_r $\%r$	$s_{\bar{r}}$ $\%r$	u_r $\%r$	b_r^2 $\%u_r^2$	s_r^2 $\%u_r^2$	$U_{95,r}$ $\%r$
X_{AD}/L	7.3072	0.01	0.07	0.07	3.87	96.13	0.13
X_{TD}/L	6.0590	0.02	0.12	0.12	1.65	98.35	0.25
Y_{TR}/L	0.0698	1.40	5.71	5.88	5.63	94.37	11.76
Y_{TD}/L	-1.7244	-0.06	-0.45	-0.45	1.57	98.43	-0.90
ψ_{AD}	-89.92	-0.02	-0.07	-0.08	8.12	91.88	-0.16
ψ_{TD}	-179.72	-0.01	-0.01	-0.01	79.78	20.22	-0.02
AD/L	2.22	0.14	0.94	0.95	2.07	97.93	1.90
TR/L	1.20	0.24	1.04	1.07	5.22	94.78	2.14
TD/L	2.99	0.10	0.80	0.81	1.46	98.54	1.62

CHAPTER 6: CONCLUSIONS AND FUTURE WORK

The IIHR wave basin is designed with the intention to accurately test free-running ship models to validate CFD results. The basin is equipped with an overhead carriage with an equipped camera system to observe the motions in six degrees of freedom. With the ability to follow the model as it is maneuvering the carriage attached camera can measure the rotations and translation of the ship model through the full scale of the testing maneuvers. The six plunger-type wave makers produce consistent waves during the trial of known heights and wavelengths. The ONRT model was run through various maneuvering tests to find the benchmark data to compare to CFD.

The uncertainty of trial runs for course keeping in both calm water and wave conditions and zig zag and turning circle maneuvers were analyzed to determine the reliability of the measurement system and the repeatability of each test to validate CFD results. The course keeping test were performed with headings ranging from 0° to -180° with 45° increments to represent head, beam, quartering, and following waves on the model. Turning circle tests were performed with a 35° rudder angle to both the port and starboard side. The zig zag maneuvers were performed with rudder angles of 10°/10°. All maneuvers and tests were performed with an initial Froude Number of 0.20 representing 1.11 m/s in the model scale, and the wave cases were performed with wavelength to ship length ratios (λ/L) of 1.0 and wave height to wavelength ratios of (H/λ) of 0.02. After tests the results were non-dimensionalized by manipulating the results by multiplying or dividing by a combination of the ship length, wave number, wave amplitude, and ship speed. This was done to allow for comparison to both CFD results and the results of other

facilities. From the data reduction equations the sensitivity coefficients were found to determine how the uncertainty propagates through the expression and determine the systematic standard uncertainty. In addition to the systematic uncertainty the random uncertainty is found by comparing the standard deviation of the measurements. In addition to the results throughout the test, the results of maneuvering were found. These include the advance, transfer, tactical diameter, and 1st and 2nd overshoot angles. The advance, transfer, and tactical diameter are divided by the ship length to non-dimensionalize and compare to the ship maneuverability standards.

After analysis the uncertainty percentages were generally found to be small with exceptions during cases where small motions occur in their respective direction. Examples of this include the surge velocity in beam waves and the sway velocity in head and following waves. The 1st harmonic amplitude accurately describes the motion of wave elevation, pitch, heave, roll, yaw, surge, and sway velocity and results in relatively small uncertainties during most cases. The 0th harmonic amplitude best describes the ship speed, X-position, and Y-position. The maneuvering characteristics reported comparable uncertainties to the two other facilities that focused on the uncertainties involved with free-running tests.

Future work includes performing long approach turning circle maneuvers to allow for equilibrium to be reached before the turning maneuver begins. This maneuver consists of an initial release with a two ship length course keeping approach before the rudder angle is changed to begin the turn. By allowing an equilibrium point to be reached before the turning maneuver begins the consistency of the rudder execution will be verified. In addition to the long approach, larger diameter turning circles will be conducted to observe

the effects of drift angles and ship speed during these tests. Left and right hand turns with course keeping before and after the turn will also be conducted.

To improve the reliability of the data recorded, the systematic standard uncertainties should be improved to limit the overall uncertainty. The consistently largest uncertainties were found as the ship speed during turning tests and the pitch and heave measurements in waves. These can be improved by reducing the vibrations on the carriage during a speed change and improving the accuracy of the carriage tracking system to report position to a similar level as the 6DOF-VMCS. Overall the largest uncertainty percentages reported were due to incredibly small mean values reported by the 0^{th} harmonic amplitude or small oscillations measured in the 1^{st} harmonic.

REFERENCES

American Bureau of Shipping, 2006, Guide for Vessel Maneuverability, American Bureau of Shipping, Houston, TX.

Araki, M., Sadat-Hosseini, H., Sanada, Y., Tanimoto, K., Umeda, N., Stern, F., 2012, Estimating maneuvering coefficients using system identification methods with experimental, system-based, and CFD free-running trial data, Ocean Engineering Vol. 51, pp. 63-84.

ASME, 2013, Performance Test Codes, Test Uncertainty, ASME PTC 19.1-2013, The American Society of Mechanical Engineers New York, NY.

Benetazzo, A. 2010, Accurate measurement of six Degree of Freedom small-scale ship motion through analysis of one camera images, Ocean Engineering Vol. 38, pp 1755-1762.

Bhushan, S., Xing, T., Carrica, P., and Stern, F., 2009, Model- and Full-scale URANS Simulations of Athena Resistance, Powering, Seakeeping, and 5415 Maneuvering, Journal of Ship Research Vol. 53, pp. 179-198.

Carrica, P., Paik, K., Hosseini, H., Stern, F., 2008, URANS analysis of a broaching event in irregular quartering seas, J. Mar. Sci. Technol., 13, pp.395-407.

Castigliona, T., Stern, F., Bova, S., Kandasamy, M., 2011, Numerical investigation of the seakeeping behavior of a catamaran advancing in regular head waves, Ocean Engineering Vol.38, 1806-1822.

Cook, S.S., 2011, Effects of headwinds on towing tank resistance and PMM tests for ONRT Tumblehome, MS (Master of Science) thesis, University of Iowa.

Davidson, K., 1944, On the Turning and Steering of Ships, Transactions of the Society of Naval Architects and Marine Engineers, Volume 52.

Eloot, K., Delefortrie, G., Vantorre, M., Quadvlieg, F., 2015, Validation of ship manoeuvring in shallow water through free-running tests, ASME 2015 34th International Conference on Ocean, Offshore an Arctic Engineering, Ocean Engineering Vol. 7.

Elshiekh, H. A., 2014, Maneuvering characteristics in calm water and regular waves for ONR Tumblehome. MS (Master of Science) thesis, University of Iowa.

Harley, B., 1994, The Society of Arts' Model Ship Trials 1758-1763: a study in the pre-history of ship model hydrodynamics, RSA Journal Vol. 142, pp. 50-52.

International Maritime Organization, 2002, Standards for Ship Maneuverability, MSC.137 (76).

ITTC, 2014a, ITTC – Recommended Procedures, Guide to the Expression of Uncertainty in Experimental Hydrodynamics, 7.5-02-01-01, pp. 1-17.

ITTC, 2014b, ITTC – Recommended Procedures and Guidelines, Free Running Model Tests, 7.5-02-06-01. Pp. 1-11.

ITTC, 2014c, ITTC – Recommended Procedures and Guidelines, Uncertainty Analysis, Example for Open Water Test, 7.5-02-03-02.2, pp. 1-15.

ITTC, 2014d, ITTC – Recommended Procedures and Guidelines, Uncertainty Analysis for Free Running Model Tests, 7.5-02-06-05, pp. 1-15.

ITTC, 2014e, ITTC – Recommended Procedures and Guidelines, Uncertainty Analysis Instrument Calibration, 7.5-01-03-01, pp. 1-16.

Leo, G., Paolillo, A., 2011, Uncertainty Evaluation of Camera Model Parameters, Instrument and Measurement Technology Conference.

Miyazaki, H., Sawada, H., Ueno, M., Tsukada, Y.,, Uncertainty analysis of maneuvering characteristic parameters obtained by free- running tests of podded propulsion ship with twin-skeg, JASNAOE No. 12 (In Japanese).

Quadvlieg, F., Brouwer, J., 2011, KVLCC2 benchmark data including uncertainty analysis to support manoeuvring predictions, IV International Conference on Computational Methods in Marine Engineering (ECCOMAS MARINE), Lisbon, Portugal.

Tonelli, R., Quadvlieg, F., 2015, New benchmark data for manoeuvring in shallow water based on free running manoeuvring tests including uncertainty of the results, OMAE ASME 34th International Conference on Ocean, Offshore and Arctic Engineering, St. John's, Newfoundland, Canada.

Sanada, Y., Tanimoto, K., Takagi, K., Gui, L., and Stern, F., 2013, Trajectories for ONR Tumblehome Maneuvering in Calm Water and Waves, Ocean Engineering Vol. 72, pp. 45-65.

Sanada, Y., Elshiekh, H., Toda, Y., Stern, F., 2014, Effects of Waves on Course Keeping Maneuvering for Surface Combatant ONR Tumblehome, 30th Symposium on Naval Hydrodynamics.

Stern, F., Olivieri, A., Shao, J., Longo, J., Ratcliffe, T., 2004, Statistical approach for estimating intervals of certification or biases of facilities or measurement systems including uncertainties, IIHR Technical Report No. 442.

Stern, F., Wilson, R., and Shao, J., 2006, Quantitative V&V of CFD simulations and certification of CFD codes, Int. J. Numer. Meth. Fluids Vol. 50, pp. 1335-1355.

Ueno, M., Yoshimura, Y., Tsukada, Y., and Miyazaki, H., 2009, Circular motion tests and uncertainty analysis for ship maneuverability, J. Mar. Sci. Technol., 14, pp. 469-484.

Yoon, H., Simonsen, C., Benedetti, L., Longo, J., Toda, Y., and Stern, F., 2015a, Benchmark CFD validation data for surface combatant 5415 in PMM maneuvers – Part I: Force/motion/motion measurements, Ocean Engineering Vol. 109, pp. 705-734.

Yoon, H., Longo, J., Toda, Y., and Stern, F., 2015b, Benchmark CFD validation data for surface combatant 5415 in PMM maneuvers – Part II: Phase-average Stereoscopic PIV Flow Field Measurements, Ocean Engineering Vol. 109, pp. 735-750.

Zhang, A., 2000, A flexible new technique for Camera Calibration, IEEE Transaction on Pattern Analysis and Machine Intelligence #22, pp. 1330-1334

APPENDIX A: INDIVIDUAL SYSTEMATIC UNCERTAINTIES

Table A.1: Quantities included in data reduction equations

ζ	m	Wave Elevation
L	m	Ship Length
X	m	X-position
Y	m	Y-position
z	m	Heave
ϕ	deg	Roll
θ	deg	Pitch
ψ	deg	Yaw
f_p	Hz	Plunger frequency
A	m	Desired wave amplitude
g	m/s^2	Gravitational constant
dx/dt	m/s	Instantaneous X-velocity
dy/dt	m/s	Instantaneous Y-velocity

A.1.1 Wave Elevation

The wave elevation throughout the test is measured by an ultrasonic wave sensor (Keyence UD-100 sensor amplified by Keyence UD-501 amplifier) positioned near the bow of the ship model. This sensor uses reflected ultrasound waves to measure how far from the senor the water level is with the initial reading being recorded during a period of calm water. This initial reading is set to the zero value. The voltage outputted from the sensor is passed through an amplifier and this elevated voltage is calibrated to relate the voltage reading to a wave height. Calibration is completed using a slide to precisely control the distance from the probe to the water. Two sources of uncertainty account for the wave elevation. These include the uncertainty due to the accuracy of the slide and the uncertainty involved in converting from a voltage signal to a wave elevation.

$$b_\zeta^2 = b_{calibration}^2 + b_{acquisition}^2 \tag{A.1}$$

Table A.2: Systematic uncertainty for wave elevation

$b_{calibration}$	mm	0.0439
$b_{acquisition}$	mm	0.5485
b_{ζ}	mm	0.5503

A.1.2 Ship Length

Ship length is designed based off of manufacturer specifications. The specification for the ONRT model is a ship length of 3.1470m with a tolerance of ±0.1 mm. The ship length can be within the full range of 3.147±0.0001 m with a normal distribution for the estimated uncertainty. Estimating within this full range the standard uncertainty is the model specification accuracy divided by 3. The value of 3 represents the maximum t-distribution value for a small sample size (ITTC, 2014c).

$$b_L^2 = \left(0.0001^2 / 3\right) \tag{A.2}$$

Table A.3: Systematic uncertainty for ship length

b_L	m	0.0001

A.1.3 X-position

The measurement data that accounts for the X-position of the ship include both the carriage's X-position as well as the deviation from the carriage center to the ship center. The deviation is found by using the 6DOF-VMCS to measure how many pixels from the center of the sub-carriage the center of the target board has moved. The camera used to observe the deviation is a Point Grey model FL2-08S2C with a NITTOH Theia MY110M

lens. The observed images are recorded through IOI FWB-EC3402 capture card. This pixel number is converted to an amount in meters based on the calibration found for the camera and lens setup. The carriage position is found with an encoder on the wheel of the main carriage. This position can have some slight deviation from the reported location due to slippage of the wheels if sudden braking occurs. The maximum deviation for DPX is based on the maximum deviation from center that the cameras can record. This maximum is based on the field of vision of the camera system (Benetazzo, 2011).

Table A.4: Systematic uncertainty for X-position

b_{CPX}	m	0.0029
b_{DPX}	m	0.0003
b_X	m	0.0029

In order to ensure that the carriage tracking system can view the mounted LED's during the duration of the test a mirror is mounted to the deck of the ship. The mirror acts to mimic lowering the position of the LED to the vertical center of gravity and ensure that when rolling occurs the LED remains within the camera's field of vision. This introduces a negligible uncertainty in relation to the position of the ship as viewed by the cameras. The uncertainty is a result of the angle that the mirror is set at and the distance from the mirror to the LED. The combination of these uncertainty sources is a small value compared to the uncertainty introduced by the rest of the tracking system.

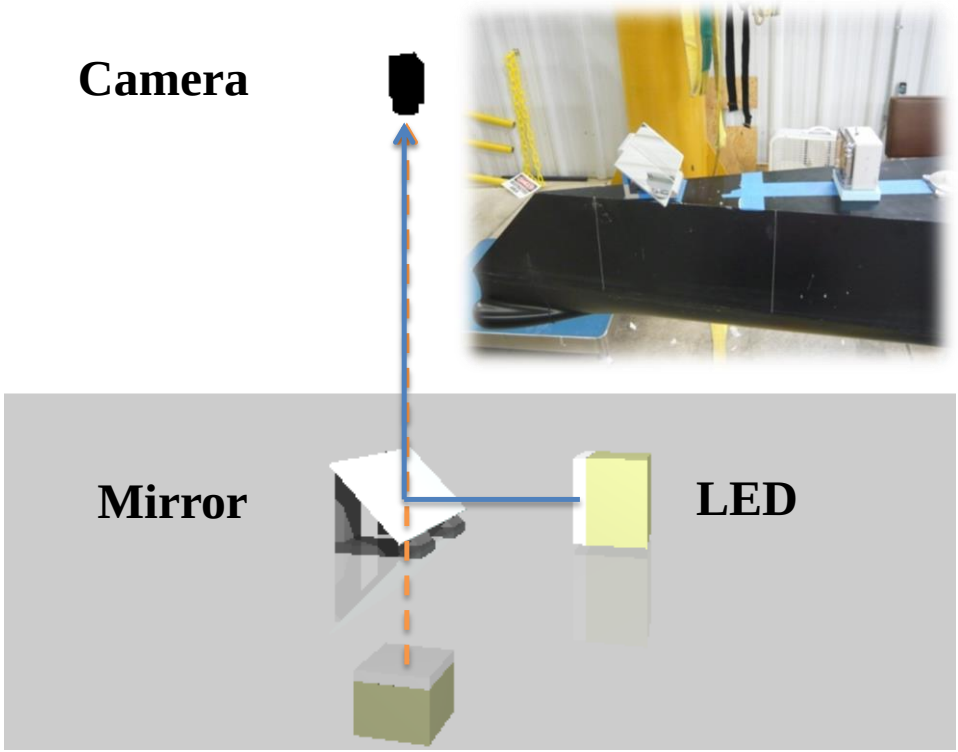

Figure A.1: LED and mirror schematic

Source: (Sanada, 2013)

The uncertainty of the X-position changes with the heading but this change is such a small degree due to the sensitivity coefficients multiplying by the changes that with the appropriate amount of significant digits the values are the same.

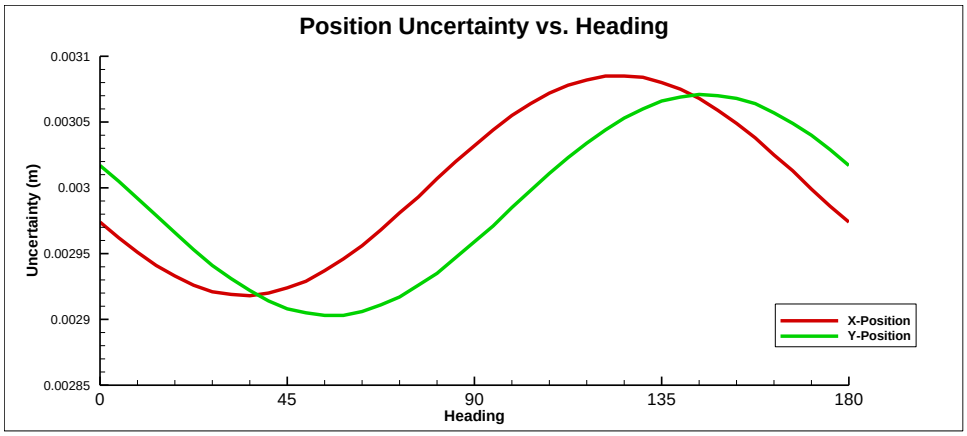

Figure A.2: Uncertainty of X and Y-Position compared to headings

A.1.4 Y-position

Similarly to X-positon the Y-position is found based on the sub-carriage location and the deviation from the center of the sub-carriage. The same 6DOF-VMCS is used but has a narrower field of view due to the resolution of the camera. Similarly to the X-position the LED and mirror setup causes a negligible uncertainty for the Y-position. Similarly to X-position there are minor changes depending on the heading but these differences are negligible.

Table A.5: Systematic uncertainty for Y-position

b_{CPY}	m	0.0029
b_{DPY}	m	0.0002
b_Y	m	0.0029

A.1.5 Heave

Heave is determined by utilizing the 6DOF-VMCS and comparing the initial condition to the current position. This measurement is based on the change in pixel location of the corners of the target board within the camera's field of view and comparing this to

the original position. A positive heave value represents the ship model being lower than the initial condition at the initialization of the test run. The uncertainty of the heave is estimated as ±0.2 mm. This estimation is derived based on the estimation within the Benetazzo paper as well as the specifications of the camera. In the following equations m represents the distance, in mm, from the centerpoint of the chessboard to the corner, and d represents the distance from the focal point to the chessboard. The uncertainty within the measurement m represents the maximum deviation from center point of the focus to the edge of the camera frame, while d is measured based on the calm water height of the ship model.

$$\overline{BP} = \sqrt{\left(X - \left(X - m/2\right)\right)^2 + \left(Y - \left(Y - m/2\right)\right)^2} = \frac{m}{\sqrt{2}} \tag{A.3}$$

$$Err_z = \frac{d\,\overline{BP}}{\overline{OB}} = \frac{md/\sqrt{2}}{\sqrt{\left(X - m/2\right)^2 + \left(Y - m/2\right)^2}} = \frac{md}{\sqrt{2}\sqrt{X^2 + Y^2}} \tag{A.4}$$

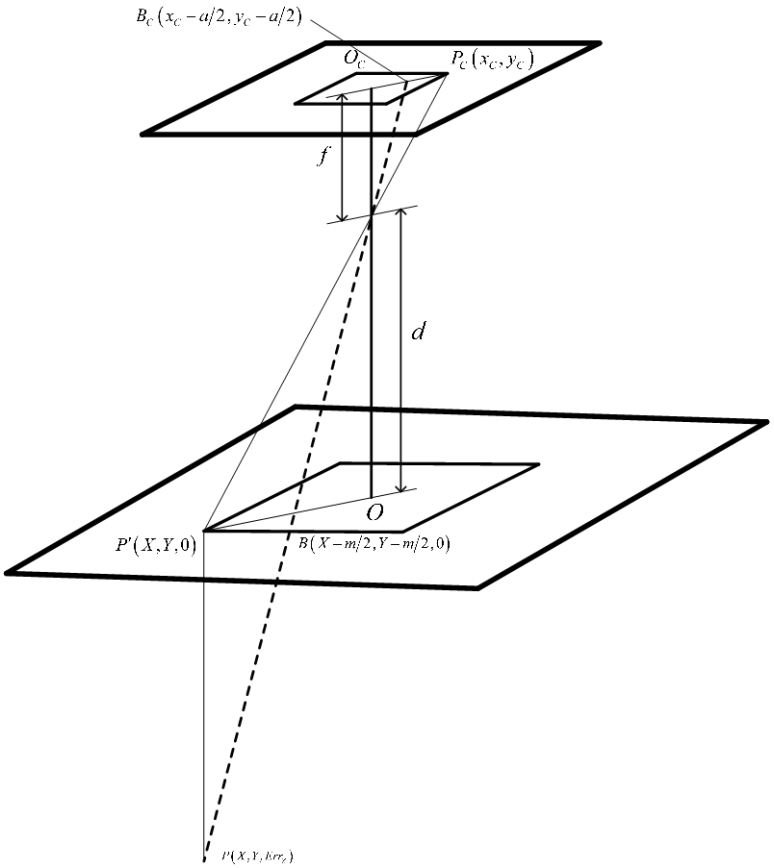

Figure A.3: Heave measurement diagram

Table A.6: Systematic uncertainty for heave

b_z	m	0.0002

A.1.6 Roll

To determine the uncertainty for roll the uncertainty of the 6DOF-VMCS is used. The roll is determined based on the observed rotation and translation matrices that are calculated based on the motion of the pattern that is mounted to the ship. This detection works by connecting the corners of the target board and determining how the angles between the target board lines change in the perspective of the camera. The uncertainty accounts for the uncertainty of the calibration of the camera, the uncertainty from the target

board dimensions, and the uncertainty from the pixel location. This total uncertainty is estimated at ±0.02 deg when utilizing sub-pixel detection for the corners. Sub-pixel detection calculates the gradient across the intersecting corners of the board to more precisely estimate the exact location of the corner. Similar to heave the roll is found based on the motion of the centerpoint of side of the chessboard. The change in height at this point is measured and converted to the roll angle achieved.

$$\phi = \tan^{-1}\left(\frac{md}{Y\left(Y + m/2\right)}\right) \tag{A.5}$$

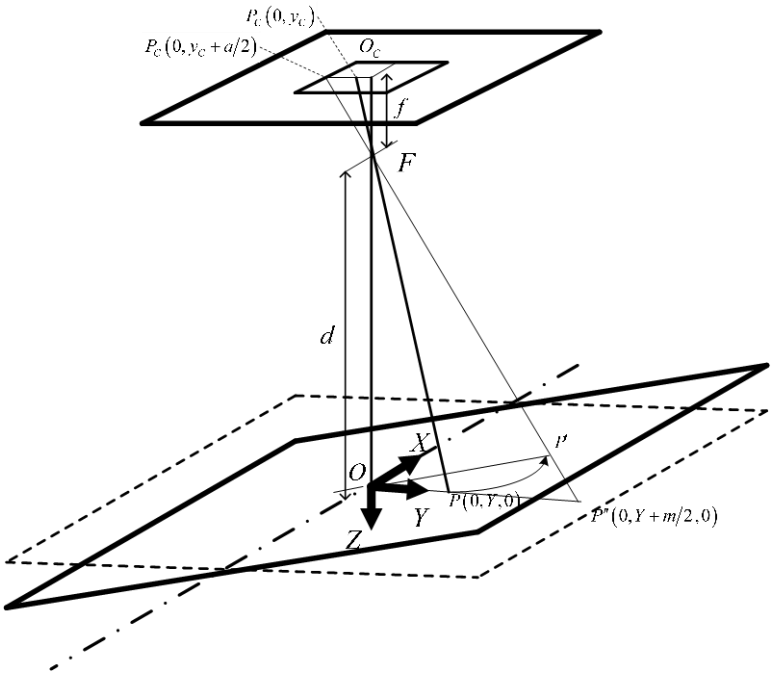

Figure A.4: 3-D roll and pitch measurement diagram

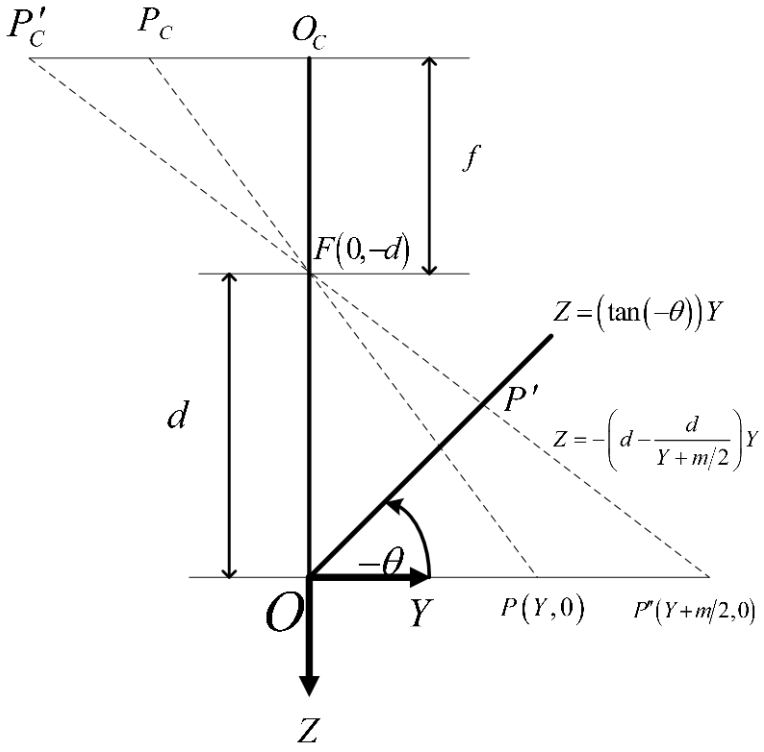

Figure A.5: 2-D roll and pitch measurement diagram

Table A.7: Systematic uncertainty for Roll

b_ϕ	deg	0.02

A.1.7 Pitch

The calculation to find uncertainty for pitch is nearly identical to the calculation for roll. This is due to the pitch and roll acting the same when viewed from above with a 90 degree rotation about the z-axis but the camera properties do not change.

$$\theta = \tan^{-1}\left(\frac{md}{Y\left(Y+m/2\right)}\right) \tag{A.6}$$

Table A.8: Systematic uncertainty for pitch

b_θ	deg	0.02

A.1.8 Yaw

Yaw is found with a combination of the 6DOF-VMCS as well as the sub-carriage rotation. The uncertainty from the 6DOF-VMCS is estimated at ±0.02 deg similarly to roll and pitch is reported as B_{DPT} representing the deviation from the sub-carriage center to the center of gravity of the ship. The uncertainty for sub-carriage rotation is based on the accuracy of the sub-carriage reported value and the backlash that occurs within the gears of the sub-carriage as it rotates. The uncertainty for sub-carriage rotation is reported as B_{CPT}. The resolution of the carriage position was accurate to ±0.01 deg and assumed as a rectangular distribution.

$$b_{CPT}^2 = \left(0.01^2 / 3\right) \tag{A.7}$$

$$\psi = \tan^{-1}\left(\frac{\frac{m}{\sqrt{2}}}{\left(X^2 + Y^2\right)}\right) \tag{A.8}$$

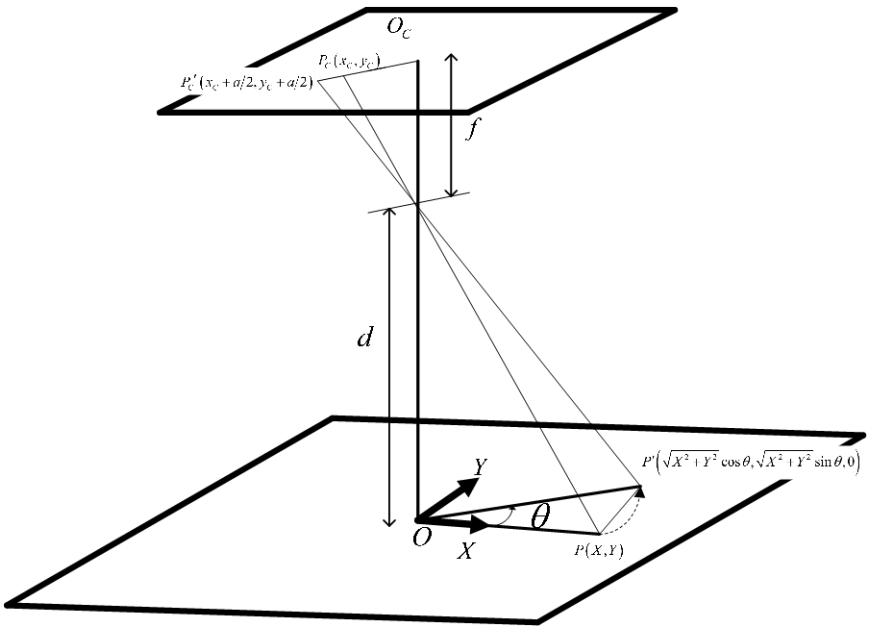

Figure A.6: 3-D yaw measurement diagram

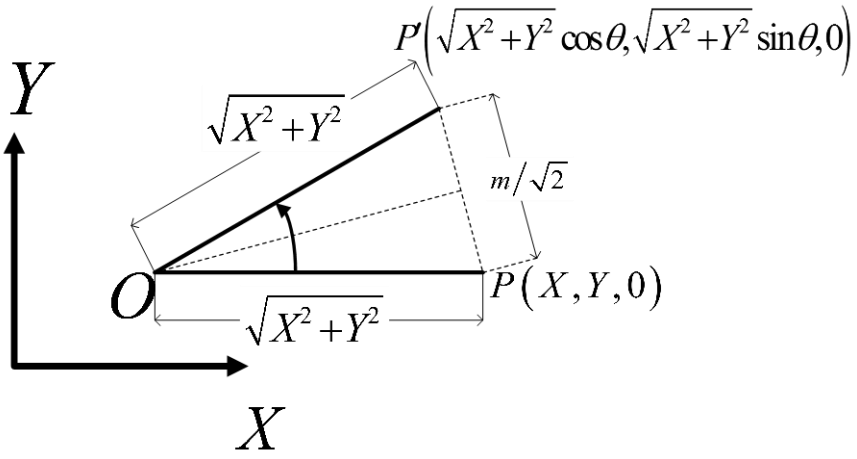

Figure A.7: 2-D yaw measurement diagram

Table A.9: Systematic uncertainty for yaw

b_{CPT}	deg	0.003
b_{DPT}	deg	0.0004
b_{ψ}	deg	0.003

A.1.9 Plunger frequency

The plunger frequency represents the motion of the plunger used to produce the waves. This value is used to replace the uncertainty due to wavelength since the wavelength cannot be directly measured.

$$\lambda = \frac{g}{2\pi f_p^2} \tag{A.9}$$

The uncertainty of the plunger frequency is based on how accurately the frequency can be set with an accuracy of ±0.01 Hz and is assumed to be a rectangular distribution (ITTC, 2014c).

$$b_{f_p}^2 = \left(0.01^2 / 3\right) \tag{A.10}$$

Table A.10: Systematic uncertainty for plunger frequency

b_{f_p}	Hz	0.006

A.1.10 Desired wave amplitude

The desired wave amplitude does not have any uncertainty due to the fact that A represents the desired amplitude as opposed to representing the actual wave amplitude. In actuality there is an amount of uncertainty with the wave amplitude that occurs, but this height difference is minimal and not accounted for. Through previous testing the produced waves were found to be well within 5% of the desired height.

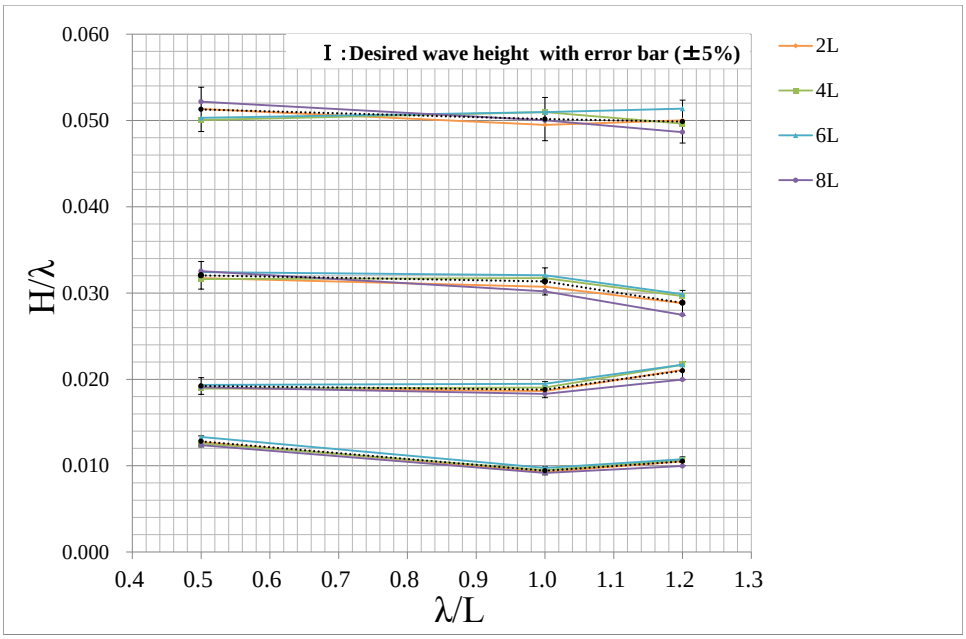

Figure A.8: Measured wave heights

Source: (Sanada, 2013)

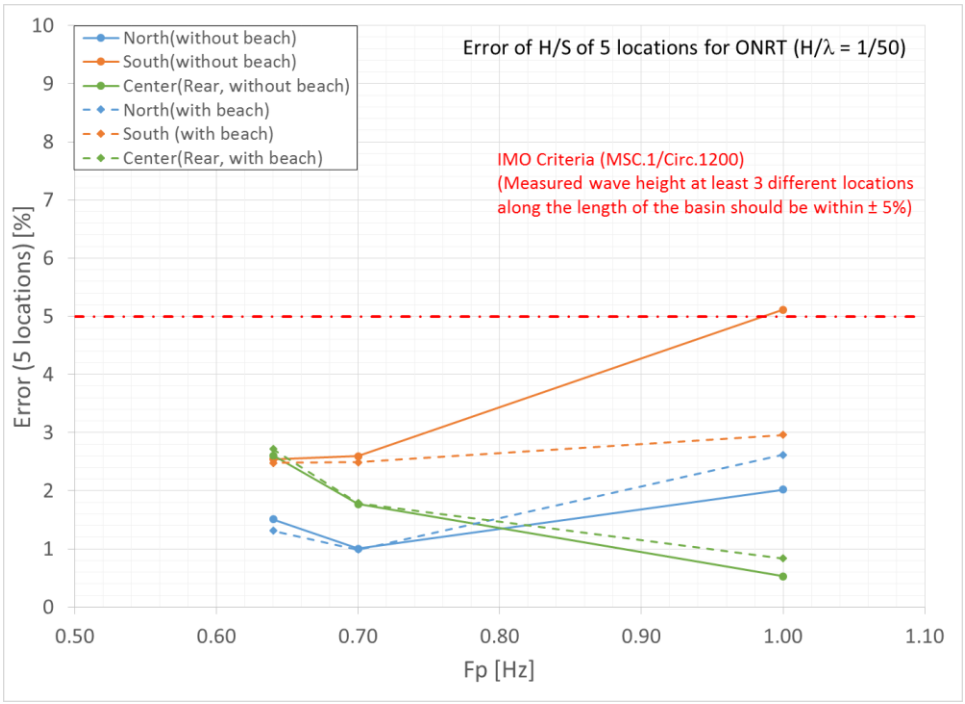

Figure A.9: Wave height errors

Source: (Sanada, 2013)

In order to evaluate the consistency and accuracy of the generated waves calibration was performed. This calibration consisted of producing varying wave height and wave length ratios within the basin and recording the heights throughout the test. Three ultrasonic wave sensors were mounted to the carriage at the center point and 6.7 meters to the north and south. The carriage was located at distances from the wave makers in increments of 6.29 meters representing approximately 2, 4, 6, and 8 ship lengths from the makers with the furthest being approximately 8 meters from the beach.

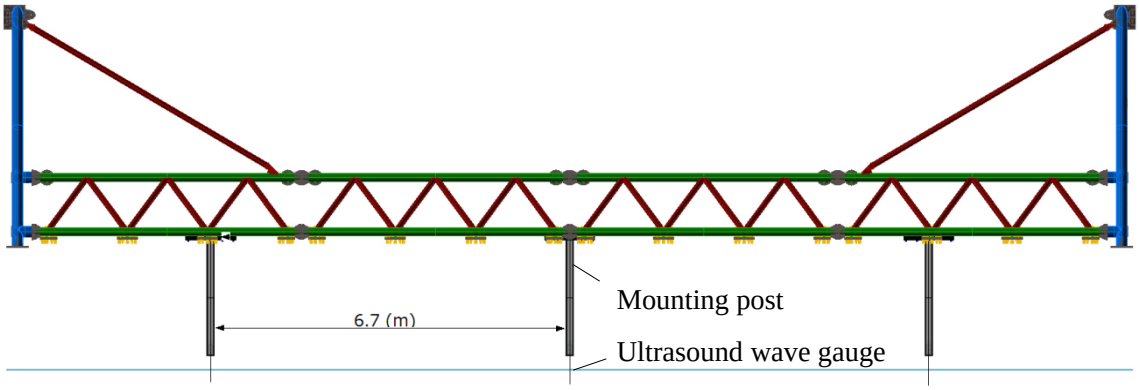

Figure A.10: Locations of wave gauges on carriage

Source: (Sanada, 2013)

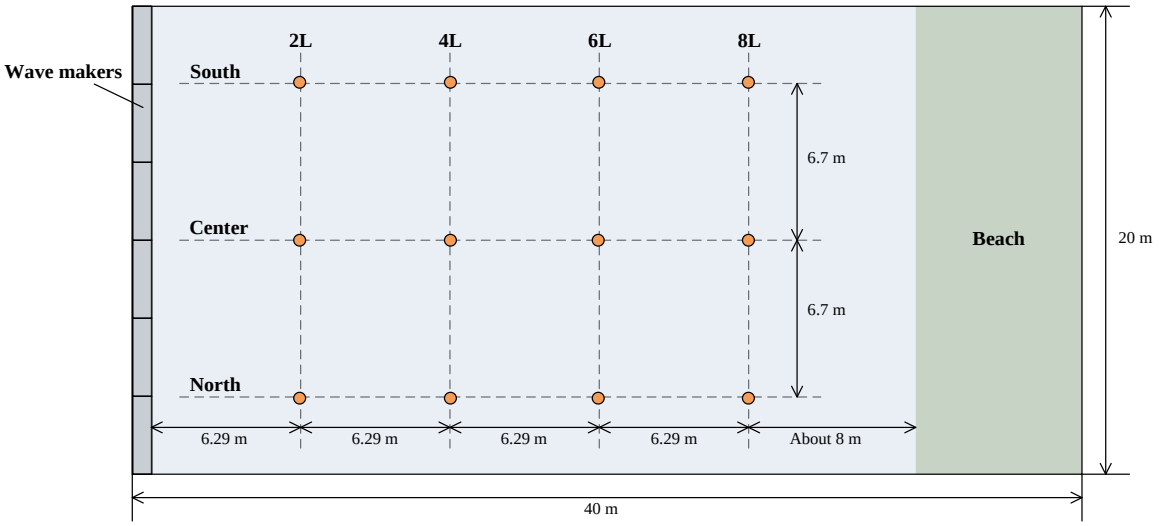

Figure A.11: Measurement locations of wave gauges

Source: (Sanada, 2013)

The wave heights are measured based on the repeated single-cycle wave train. This represents 10 cycles of waves moving past each wave gauge and then being overlaid to display the repeatability of the waves. From the average wave found the standard deviation of the period for each individual wave case is reported. From this standard deviation and average the measured wave heights are found to be within 3% of the average across the entirety of the basin when the movable beach is in place. Without the movable beach in place the south end of the basin has a larger error of approximately 5% due to the change in shape that allows for the model to be transported from the trimming tank. With the beach in place during trials consistent results are found.

Table A.11: Systematic uncertainty for desired wave amplitude

b_A	m	0.00

A.1.11 Gravitational constant

The uncertainty associated with the gravitational constant is negligible due to the accuracy of the constant being calculated based on the latitude and altitude of the testing facility which can be measured with almost no uncertainty. The standard gravitational constant of 9.80665 m/s^2 is used.

Table A.12: Systematic uncertainty for gravitational constant

b_g	m/s^2	0.00

A.1.12 Instantaneous X-velocity

To calculate the instantaneous X-velocity the difference in X-position across two time steps $(\Delta t = 0.05s)$ is compared to the time change across the two time steps.

$$\frac{dx}{dt} = \frac{x_{i+1} - x_{i-1}}{2\Delta t} \tag{A.11}$$

The uncertainty for both x_{i+1} and x_{i-1} are the uncertainty for X-position and the uncertainty for Δt is represented as the accuracy of the time step. The X-position uncertainty is calculated above.

$$b_{\Delta t}^2 = \left(0.05^2 / 3\right) \tag{A.12}$$

Table A.13: Systematic uncertainty for instantaneous X-velocity

b_X	m	0.0029
$b_{\Delta t}$	s	0.03
$b_{dx/dt}$	m/s	0.01

A.1.13 Instantaneous Y-velocity

The calculation for instantaneous Y-velocity follows the same procedure as the instantaneous X-velocity but uses the change in Y-position as opposed to X-position. The Y-position uncertainty is calculated above.

$$\frac{dx}{dt} = \frac{y_{i+1} - y_{i-1}}{2\Delta t} \tag{A.13}$$

Table A.14: Systematic uncertainty for instantaneous Y-velocity

b_Y	m	0.0029
$b_{\Delta t}$	s	0.03
$b_{dy/dt}$	m/s	0.01

A.1.14 Rudder Angle

The rudder angle is controlled by a PID controller with the properties of $K_P = 1$ and $K_I = K_D = 0$. This represents that the controller is only operated based on the current time and deviation from the desired heading angle without accounting for past or expected future heading difference.

$$\delta(t) = K_P\left(\psi(t) - \psi_c\right) \tag{A.14}$$

In the above equation $\psi(t)$ represents the current yaw angle where ψ_C represents the target yaw angle and a maximum rudder angle of 35 degrees is a requirement based on the model specifications. From this equation the sensitivity coefficients are found to determine the uncertainty of the rudder angle throughout the test.

$$\theta_{\psi(t),\delta(t)} = K_P \tag{A.15}$$

$$\theta_{\psi_C,\delta(t)} = K_P \tag{A.16}$$

$$\theta_{K_P,\delta(t)} = \psi(t) - \psi_c \tag{A.17}$$

With the target heading having no uncertainty due to it representing the desired heading and the proportional setting also being a fixed constant without uncertainty the systematic uncertainty of the rudder angle reduces to:

$$b_\delta = b_\psi \theta_{\psi(t),\delta(t)} = b_\psi K_P = b_\psi \tag{A.18}$$

A.1.15 Metacentric height

The metacentric height (GM) is found by moving a small counter weight from port to starboard on the ship when the model is placed in the water. The weight is ideally moved as far as possible to reduce the relative inaccuracies from the limited accuracy of the distance moved. The change in the roll angle of the model is recorded by a digital protractor (SPI-TRONIC Pro 3600).

$$GM = \frac{wd}{W \tan(\theta)} \tag{A.19}$$

The sensitivity coefficients are derived from this expression.

$$\theta_{w,GM} = \frac{w}{W\tan(\theta)} \tag{A.20}$$

$$\theta_{d,GM} = \frac{d}{W\tan(\theta)} \tag{A.21}$$

$$\theta_{W,GM} = -\frac{wd}{W^2\tan(\theta)} \tag{A.22}$$

$$\theta_{\theta,GM} = \frac{wd}{W\left(1+\theta^2\right)} \tag{A.23}$$

Table A.15: Systematic uncertainty for Metacentric height

b_w	kg	0.003
b_d	m	0.0006
b_W	kg	0.06
b_θ	deg	0.1
b_{GM}	m/s	0.0001

A.1.16 Moment of Inertia

The moment of inertia is measured by mounting the model on a carriage and displacing the model a known distance. From here the model is released and swings, the period of this swinging is measured with the known carriage and ship mass to find. Additional masses are located at either the center or end of model and the difference in time is directly related to the moment of inertia in both X and Y direction.

$$\frac{K_{xx}}{B} = \frac{\sqrt{I_m / M_m}}{B} \tag{A.24}$$

$$\frac{K_{yy}}{L_{pp}} = \frac{\sqrt{I_m / M_m}}{L_{pp}} \tag{A.25}$$

From these expressions sensitivity coefficients are found where B, L_{pp}, I_m, and M_m represent the beam width, ship length, moment of inertia, and mass of the ship model respectively.

$$\theta_{B,\frac{K_{xx}}{B}} = -\frac{\sqrt{I_m}}{B^2\sqrt{M_m}} \tag{A.26}$$

$$\theta_{I_m,\frac{K_{xx}}{B}} = \frac{1}{2B\sqrt{I_m M_m}} \tag{A.27}$$

$$\theta_{M_m,\frac{K_{xx}}{B}} = -\frac{\sqrt{I_m}}{2BM_m^{3/2}} \tag{A.28}$$

$$\theta_{B,\frac{K_{yy}}{L_{pp}}} = -\frac{\sqrt{I_m}}{L_{pp}^2\sqrt{M_m}} \tag{A.29}$$

$$\theta_{I_m,\frac{K_{yy}}{L_{pp}}} = \frac{1}{2L_{pp}\sqrt{I_m M_m}} \tag{A.30}$$

$$\theta_{M_m,\frac{K_{yy}}{L_{pp}}} = -\frac{\sqrt{I_m}}{2L_{pp}M_m^{3/2}} \tag{A.31}$$

Table A.16: Systematic uncertainty for moment of inertia

$b_{\frac{k_{xx}}{B}}$	-	0.021
$b_{\frac{k_{yy}}{L_{pp}}}$	-	0.04

A.1.17 Natural Roll Period

The natural roll period is measured by attaching an incline sensor to the model before placing the model in the water. From this position the model is displaced in roll to a known angle of 8 degrees before being released. The roll period is then measured as the ship rocks back and forth recording the time between upswings through zero degrees. These periods are measured through a DAQ with a precision of 0.01 seconds. From the inline sensor (MEMSIC CXTA01) the zero angle voltage was reported to be 2.5 ± 0.15 volts and the voltage is converted to an angle by equation A.25. Once the angles are found the average across ten periods is calculated and reported as the natural roll period.

$$\phi = \sin^{-1}\left[\frac{V_{out}(V) - ZeroAngleVoltage(V)}{Sensitivity(V/rad)}\right] \tag{A.32}$$

$$b_{T_\phi}^2 = \left(0.01^2/3\right) \tag{A.33}$$

Table A.17: Systematic uncertainty for natural roll period

b_{T_ϕ}	s	0.0058

A.1.18 Wave Encounter Frequency

The wave encounter frequency is used to calculate the harmonic amplitude and phases of the model motions during wave cases. The wave encounter frequency is found based on the plunger frequency, wavelength, ship speed and heading.

$$f_e = f_p - \frac{U\cos(\chi + 180)}{\lambda} \tag{A.34}$$

The wavelength is substituted by the plunger frequency to allow for the uncertainty to be found based on the measured and controlled variables. The resulting wave encounter frequency calculation is found as:

$$f_e = f_p - \frac{2\pi f_p^2 U \cos(\chi + 180)}{g} \tag{A.35}$$

Based on the above data reduction equation the sensitivity coefficients are found based on the partial derivatives and the systematic uncertainties of the variables. The systematic uncertainty of gravity is assumed to be zero while the systematic uncertainty of the heading is based on the yaw angle found.

$$\theta_{f_p, f_e} = \frac{\partial(f_e)}{\partial(f_p)} = 1 - \frac{4\pi f_p U \cos(\chi + 180)}{g} \tag{A.36}$$

$$\theta_{g, f_e} = \frac{\partial(f_e)}{\partial(g)} = \frac{2\pi f_p^2 U \cos(\chi + 180)}{g^2} \tag{A.37}$$

$$\theta_{\chi, f_e} \frac{\partial(f_e)}{\partial(\chi)} == \frac{2\pi f_p^2 U \sin(\chi + 180)}{g} \tag{A.38}$$

$$\theta_{U, f_e} = \frac{\partial(f_e)}{\partial(U)} = -\frac{2\pi f_p^2 \cos(\chi + 180)}{g} \tag{A.39}$$

The systematic uncertainty of the wave encounter frequency is found based on the individual biases and sensitivity coefficients. The systematic uncertainty of the wave encounter frequency strongly changes with the heading of the model. The wave encounter frequency and error bars are plotted in figure A.12 with the uncertainty percentages plotted

in A.13. Across the full range of headings the plunger frequency and ship speed alternate being the larger contributor of systematic uncertainties. The lowest uncertainty percentages occur near headings of ±90 deg with the maximum uncertainty percentage at the heading of 180 degrees with the ship speed being the largest contributor at this point with all uncertainty percentages being between 0.8 and 3%.

Table A.18: Systematic uncertainty for wave encounter frequency during head waves

f_e	Hz	1.057
b_{f_p}	Hz	0.006
b_g	m/s^2	0.00
b_χ	deg	0.033
b_U	m/s	0.0029
b_{f_e}	Hz	0.0156

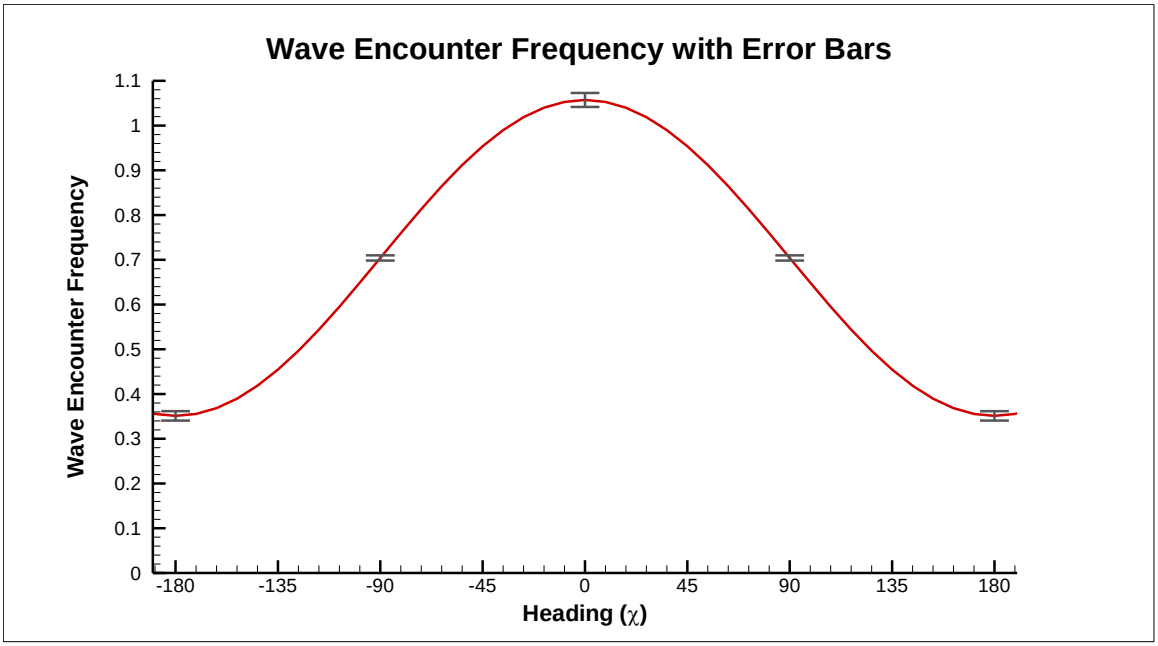

Figure A.12: Wave encounter frequency with various headings and error bars

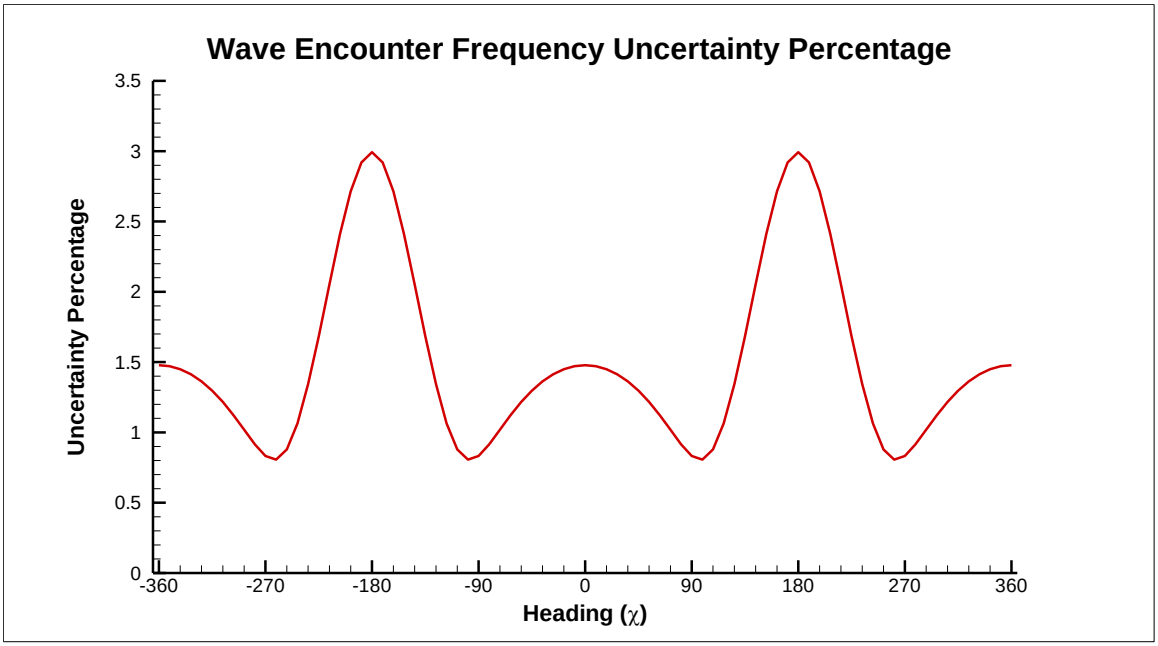

Figure A.13: Uncertainty percentages of wave encounter frequency

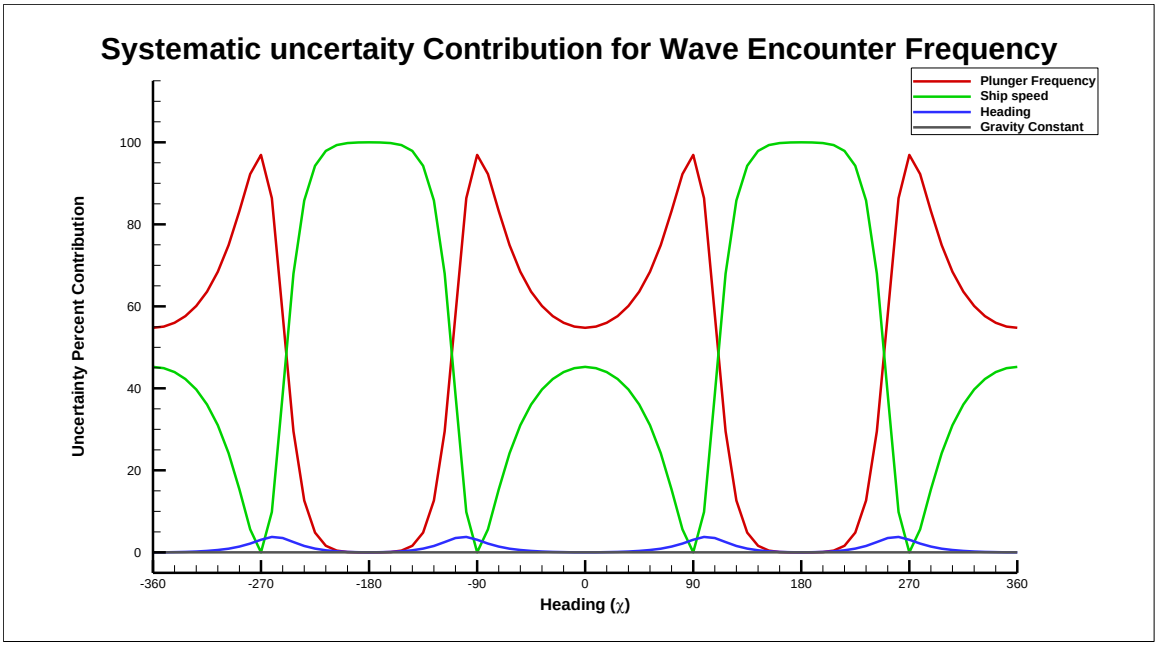

Figure A.14: Uncertainty percentage contribution for wave encounter frequency

APPENDIX B: 6DOF-VMCS UNCERTAINTY PROPAGATION

The calibration of the 6DOF-VMCS is performed based on the proposed lens and camera combination that will be used for experimentation. This setup is used to capture a series of images of the target board to determine the intrinsic parameters of the camera representing the focal distance, lens distortion, and sensor size of the camera. The combination of these values represent the matrix A. To ensure an accurate calibration a wide range of views of the target board should be taken representing the full view of potential orientation of the model during testing. With a sufficient set of images and sub-pixel accuracy being used the calibration uncertainty should be approximately one pixel in the x, y, and heave translations as well as a very small uncertainty of the reported angles, this small amount of uncertainty should be negligible compared to the other measurement systems utilized to report the ship motion. The measured translation and rotations are observed based on the orientation of the target board represented as the pixel locations of the corner points. This orientation is compared to the initial position of the target board to report the change in position from the start of the trial. The measured rotations are reported as a part of the matrix R while the translations are recorded in matrix T. The combination of the intrinsic camera parameters and the extrinsic rotations and translations are reported as matrix P describing the projection matrix. With a single view of the target board it is possible to accurately report the location of all corners of the target board resulting in an accurate orientation of the model during the trial. The matrix A will remain constant throughout the entirety of the trial after calibration while the matrices R and T will vary with time throughout the trial (Zhang, 2000).

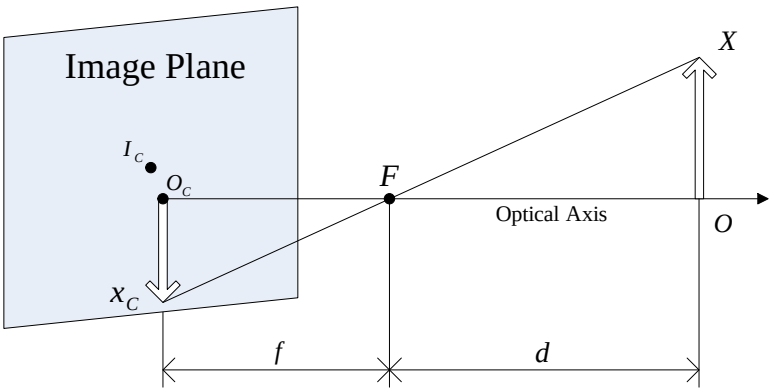

Figure B.1: Pinhole camera model

$$P = A[R \mid T] \tag{B.1}$$

$$A = \begin{bmatrix} f_x & 0 & c_x \\ 0 & f_y & c_y \\ 0 & 0 & 1 \end{bmatrix} \tag{B.2}$$

$$R = \begin{bmatrix} 1 & 0 & 0 \\ 0 & \cos\theta_x & \sin\theta_x \\ 0 & -\sin\theta_x & \cos\theta_x \end{bmatrix} \cdot \begin{bmatrix} \cos\theta_y & 0 & -\sin\theta_y \\ 0 & 1 & 0 \\ \sin\theta_y & 0 & \cos\theta_y \end{bmatrix} \cdot \begin{bmatrix} \cos\theta_z & \sin\theta_z & 0 \\ -\sin\theta_z & \cos\theta_z & 0 \\ 0 & 0 & 1 \end{bmatrix} \tag{B.3}$$

$$T = \begin{bmatrix} T_x \\ T_y \\ T_z \end{bmatrix} \tag{B.4}$$

Calibration is performed by using a direct linear transformation (DLT) method. This method utilizes the image set of target board views to find the elements of matrix P using a decomposition of algorithms. This decomposition tracks the propagation of systematic uncertainties through the algorithms to find the combination of pixel coordinates and world coordinates. By analyzing the found camera parameters, and current rotations and translations the uncertainty of the measurement system can be estimated. One uncertainty assessment of a similar system found a target point uncertainty to be under 1

pixel and under 0.1 mm for translations, though the center point of a circle was used instead of corners for the target points. Within Leo et al., 2011, ISO GUM uncertainty evaluations are used as opposed to ASME 2013 allowing for the potential of a difference in calculated uncertainties, with a slightly difference process the calculated uncertainty can vary but should be minimal with the scale of uncertainties predicted.